La résistance osseuse du radius distal humain suite une chute sous chargement, une étude expérimentale et numérique

Edison Zapata

N° d'ordre : 275 -2015 Année 2015

THESE DE L'UNIVERSITE DE LYON

Délivrée par

L'UNIVERSITE CLAUDE BERNARD LYON 1

ECOLE DOCTORALE MEGA

DIPLOME DE DOCTORAT
(Arrêté du 7 août 2006)

Spécialité : Biomécanique

Soutenue publiquement le 2 décembre 2015

Par :

Edison ZAPATA

Bone strength of the human distal radius under fall loading conditions

an experimental and numerical study

Directeur de thèse: **David MITTON**
Co-Encadrante : **Hélène FOLLET**

JURY :

Lalaonirina RAKOTOMANANA	Professeur des Universités, Université de Rennes	Rapporteur
Bert VAN RIETBERGEN	Professeur associé, Université de Technologie d'Eindhoven	Rapporteur
Pascal LAUGIER	Directeur de Recherche, CNRS, Paris	Examinateur
Jean-Baptiste PIALAT	Professeur des Universités, Université Claude Bernard Lyon 1	Examinateur
Hélène FOLLET	Chargée de recherche, INSERM, Lyon	Examinateur
David MITTON	Directeur de Recherche, IFSTTAR, Lyon	Examinateur

UNIVERSITE CLAUDE BERNARD - LYON 1

Président de l'Université	**M. François-Noël GILLY**
Vice-président du Conseil d'Administration	M. le Professeur Hamda BEN HADID
Vice-président du Conseil des Etudes et de la Vie Universitaire	M. le Professeur Philippe LALLE
Vice-président du Conseil Scientifique	M. le Professeur Germain GILLET
Directeur Général des Services	M. Alain HELLEU

COMPOSANTES SANTE

Faculté de Médecine Lyon Est – Claude Bernard	Directeur : M. le Professeur J. ETIENNE
Faculté de Médecine et de Maïeutique Lyon Sud – Charles Mérieux	Directeur : Mme la Professeure C. BURILLON
Faculté d'Odontologie	Directeur : M. le Professeur D. BOURGEOIS
Institut des Sciences Pharmaceutiques et Biologiques	Directeur : Mme la Professeure C. VINCIGUERRA
Institut des Sciences et Techniques de la Réadaptation	Directeur : M. le Professeur Y. MATILLON
Département de formation et Centre de Recherche en Biologie Humaine	Directeur : Mme. la Professeure A-M. SCHOTT

COMPOSANTES ET DEPARTEMENTS DE SCIENCES ET TECHNOLOGIE

Faculté des Sciences et Technologies	Directeur : M. F. DE MARCHI
Département Biologie	Directeur : M. le Professeur F. FLEURY
Département Chimie Biochimie	Directeur : Mme Caroline FELIX
Département GEP	Directeur : M. Hassan HAMMOURI
Département Informatique	Directeur : M. le Professeur S. AKKOUCHE
Département Mathématiques	Directeur : M. le Professeur Georges TOMANOV
Département Mécanique	Directeur : M. le Professeur H. BEN HADID
Département Physique	Directeur : M. Jean-Claude PLENET
UFR Sciences et Techniques des Activités Physiques et Sportives	Directeur : M. Y.VANPOULLE
Observatoire des Sciences de l'Univers de Lyon	Directeur : M. B. GUIDERDONI
Polytech Lyon	Directeur : M. P. FOURNIER
Ecole Supérieure de Chimie Physique Electronique	Directeur : M. G. PIGNAULT
Institut Universitaire de Technologie de Lyon 1	Directeur : M. le Professeur C. VITON
Ecole Supérieure du Professorat et de l'Education	Directeur : M. le Professeur A. MOUGNIOTTE
Institut de Science Financière et d'Assurances	Directeur : M. N. LEBOISNE

Bone strength of the human distal radius under fall loading conditions:
an experimental and numerical study

Fragility fractures represent a public health problem for elderly. The assessment of the bone strength and of the risk of fracture by the gold standard method (Dual X-ray Absorptiometry - DXA) is limited. Micro-finite element models (μFEM) have shown to better predict the bone strength, but it is not possible to confirm that they do better than the density measured by DXA to estimate the risk of fracture. Thus, the aim of this thesis was to evaluate whether including realistic loading conditions could improve the level of prediction of the FEM. First, we reproduced the loading conditions of a forward fall on 32 radii in an ex-vivo experiment. This experiment leaded to two groups: one fractured and one non - fractured. Then, we evaluated the prediction capability of a segment FEM (9 mm of the distal radius) created using the High Resolution peripheral Quantitative Computed Tomography. This segment FEM was tested under the axial loading (standard analysis), and under five additional non-axial configurations. It was found that the prediction capability of the segment FEM was not improved by the implementation of non-axial loadings. Finally, a heterogeneous FEM of the whole distal radius was created using data from a Cone Beam Computed Tomography. This model considers the fall loading configurations in orientation and speed of the ex-vivo experiment. The FEM of the whole distal radius has a better accuracy to predict the experimental failure load than the segment FEM. This study proposes original data for model validation dedicated to further improvements of fracture risk prediction.

Keywords: Bone Strength, Fracture Risk, Distal Radius, Forward fall, Finite Element Models.

Résistance du radius humain distal soumis à un chargement représentatif d'une chute:
Etude expérimentale et numérique

Les fractures de fragilité représentent un problème de santé publique pour les personnes âgées. L'évaluation de la résistance osseuse et du risque de fracture par la méthode de référence (absorption bi-photonique à rayons X, DXA) est limitée. Les micro-modèles en éléments finis (μFEM) ont montré de meilleures prédictions de la résistance osseuse, mais on ne peut confirmer qu'ils améliorent l'estimation du risque de fracture par rapport à la DXA. L'objectif de cette thèse était donc d'évaluer si la prédiction par simulation numérique pouvait être améliorée en prenant en compte des conditions réalistes de chargement. Tout d'abord, les conditions de chargement correspondant à une chute vers l'avant ont été reproduites sur 32 radius humain dans une expérimentation ex-vivo. Les résultats expérimentaux ont conduits à deux groupes : un fracturé et un non fracturé. Puis, la capacité de prédiction d'un modèle « ségment » (9 mm de radius distal) créé en utilisant un scanner à très haute résolution (High Resolution peripheral Quantitative Computed Tomography) a été évaluée. . Différentes configurations (axiale (configuration standard) et 5 non-axiales) ont été simulées. L'implémentation de chargement non-axial n'a pas amélioré la capacité de prédiction du modèle « segment ». Finalement, un modèle hétérogène du radius distal entier a été créé à partir d'un scanner clinique (Cone Beam Computed Tomography). Ce modèle a pris en compte les conditions d'une chute en termes d'orientation et de vitesse. Le modèle de radius distal entier a montré une meilleure prédiction de la charge à la rupture expérimentale que le modèle « segment ». Cette étude propose des données originales pour la validation de modèles numériques pour l'amélioration de la prédiction du risque de fracture.

Mots clés: Résistance osseuse, Risque de fracture, Radius distal, Chute, Modèles éléments finis.

Laboratoire de Biomécanique et de Mécanique des Chocs – UMR_T9406 (IFSTTAR-UCBL)
25 Avenue François Mitterrand, Case 24, 69675 BRON Cedex France

Pathophysiology, Diagnosis and Treatments of Bone Diseases – UMR1033 (INSERM-UCBL)
7-11, rue G. Paradin, 69372 Lyon Cedex 08 France

Foreword

This thesis was performed in collaboration between the Laboratoire de Biomécanique et Mécanique des Chocs (LBMC) (joint unit between the French institute of science and technology for transport, development and networks (IFSTTAR) and Université Claude Bernard Lyon 1 (UCBL) and the Laboratory LYOS (joint unit between the French Institute of Health and Medical Research (INSERM) and UCBL).

A grant for this thesis was provided by the Administrative Department of Science, Technology and Innovation (COLCIENCIAS), which is the government agency supporting fundamental and applied research in COLOMBIA.

I would like to thank Dr. Philippe Vezin, director of LBMC, and the Dr. George BOIVIN, responsible of the Team "Bone Quality and Biological markers" at the INSERM unit 1033 (LYOS), for their kind welcome and acceptance into their laboratories.

I would like to express my sincere gratitude to my advisors Dr. David Mitton and Dr. Hélène Follet for their excellent guidance, caring and patience. They provided me priceless advices that I will undoubtedly remember for my career in research.

I would like to thank Pr. Lalaonirina Rakotomanana, Pr. Bert van Rietbergen and Dr. Pascal Laugier for taking part of the jury committee.

To Jean-Paul Roux, Dr. François Dubœuf, Dr. Stéphanie Boutroy and Dr. Jean-Baptiste Pialat (jury member), I am deeply grateful for everything you taught during these years and for all your support.

I own also my gratitude to Dr. Phillippe Beillas, whom introduce me into the finite element models for injury risk prediction, for his kind observations during my thesis.

I want to thank the technical support of Leila Benboubaker, Yves Caire, Stéphane Ardizzone, Jean-Luc Russo and Marc Dagnino.

I want to thank all my fellow labmates from the LYOS and LBMC. I specially thank Camille Ponçon, Florien Montagner, Sébastien Rizzo, Emmanuelle Lefèvre, Rafaa Ellouz, Roman Desbats, Pascal Vallée and Fabien Berthet for their friendship and support.

The last but not least, I would also like to extend my gratitude to my much-loved parents, my beloved Valentina Vera and my closest friends, for their unconditional affection and sincere support over all these years.

Contents

Foreword 4

Contents 5

Introduction 8

Chapter 1. State of Art 10

1.1 Introduction 10

1.2 Anatomy 11

1.2.1 Anatomical Planes 11

1.2.2 The Bones 11

1.2.3 The Radius 12

1.3 Epidemiology of Fragility fractures 14

1.4 Bone fragility estimation in clinics 15

1.4.1 Dual-energy x-ray absorptiometry 15

1.4.2 Computed tomography scan 17

1.4.3 The High Resolution peripheral Quantitative Computed Tomography 18

1.4.4 The FRAX 20

1.4.5 Distal radius fractures description and classification 21

1.5 Bone fragility estimation in research 23

1.5.1 Mechanical Definitions 23

1.5.2 Bone Imaging 24

1.5.3 Topology and Material properties 26

1.5.4 Material law assumptions 29

1.5.5 Meshing options 30

1.5.6 Risk of fracture definition 31

1.5.7 Failure criteria 31

1.6 Discussion: Selection of the loading conditions 35

1.7 Conclusions and aims 37

Chapter 2. Experimental protocol to reproduce a forward fall leading to fractured and non-fractured radii 39
2.1 Introduction 39
2.2 Methods 39
2.3 Results 45
2.3.1 Maximum Forces from the experiment 45
2.3.2 Fracture cases and type of fractures 50
2.3.3 Strain analysis 51
2.4 Discussion 52
2.5 Conclusions 54
Chapter 3. Numerical study: effect of the loading direction 55
3.1 Introduction 55
3.2 Methods and results 55
3.2.1 Validation Study 60
3.2.2 Effect of the loading direction 65
3.2.3 Discrimination of the groups 70
3.2.4 Accuracy of the models 71
3.2.5 Correlations between model and experiment 71
3.2.6 Assessment of the risk of fracture 72
3.2.7 Assessment of a criterion 73
3.3 Discussion 76
3.4 Conclusions 77
Chapter 4. Finite element model reproducing an ex-vivo forward fall on the distal radius. 78
4.1 Introduction 78
4.2 Methods and results 79
4.3 Discussion 89
4.4 Conclusion 90

General Conclusion 92

Bibliography 95

Appendix 1: Personal Communications 104

Appendix 2: Summary in French 111

Introduction 111

Chapitre 1 : Contexte de l'étude 113

Chapitre 2 : Protocole expérimental afin de reproduire une chute vers l'avant sur radius humain 117

Chapitre 3 : Etude numérique: effet de la direction de chargement sur segment 123

Chapitre 4 : Modèle éléments finis reproduisant une chute en avant sur radius distal ex vivo 128

Conclusion générale 135

Appendix 3: FEM Parameters from CT-Scat and HR-PQCT 138

Introduction

Fragility fractures are a worldwide health problem. These types of fractures, which correspond to any fracture caused by a fall from the standing height or less, are related to underlying diseases generating bone fragility. The osteoporosis is one of these diseases. Its prevalence in women in the largest countries in the EU (France, Germany, Italy, Spain and UK) is estimated in more than 12 million cases (Kanis et al. 2013).

The gold standard method for the clinical diagnosis of the osteoporosis and the evaluation of the risk of fracture is the Dual X-ray Absorptiometry (DXA)(World Health Organization 2004). This method is based on the measurement of bone mineral density at different anatomical sites. It has been shown that this measure, which is an x-ray 2D projection, presents an insufficient sensibility, because 50 % of fractures occur in patients considered non osteoporotic (Siris et al. 2001).

Ongoing research has proposed different methods to improve this sensibility. One of these methods is the FRAX, which is a survey correlating different 'risk factors' to estimate the risk of fracture over ten years. However, this method does not integrate the falls and the disturbances of the walking in the algorithm of prediction (Chapurlat 2013). In other words, this survey cannot take into account the external loading conditions that increase the risk of fracture. Another method that has been proposed is the analysis by micro-finite element models (μFEM) created using a High Resolution peripheral Quantitative Computed Tomography (HR-pQCT) (Vilayphiou et al. 2010). All validation studies have shown that the estimation of the bone strength is better achieved by the μFEM (R^2 between 0.73 and 0.92) than using density measures from the DXA (R^2 between 0.31 and 0.71)(Rietbergen & Ito 2015). Despite this good level of prediction of the bone strength, retrospective studies have not provide at this moment a clear evidence that the output of μFEM are better predictors of the risk of fracture than the density measurements by DXA (Rietbergen & Ito 2015).

The standard method of μFEM analysis is the static-axial loading. However, in the case of a fall, velocities can reach 2 m/s, that should be considered as a dynamic loading. Also, it has been shown that only 15 % of the fall cases are associated with an axial load on the radius (Melton et al. 2010). Thus, the aim of this thesis was to study the influence of using realistic

loading conditions (direction and velocity), in finite element models for the assessment of bone strength and the fracture risk. This study was carried out in three steps:

First, we developed an ex-vivo experiment to reproduce a fall case, leading to fractured and non-fractured radii (Chapter 2). The case of the study was a forward fall with outstretched hand. The angle between the volar face of the radius and the ground was 75° and the velocity when impacting the ground was 2 m/s.

Second, we evaluated the prediction capability in different conditions of a segment FEM (9 mm distal radius) created using the HR-pQCT (Chapter 3). It was tested under the axial loading (standard configuration of analysis), and under five additional non-axial configurations.

In the third step, a heterogeneous FEM of the whole distal radius was created using data from a Cone Beam Computed Tomography (Chapter 4). This model simulated the dynamic non-axial loading conditions of the ex-vivo experiment representing a forward fall case. The accuracy to predict the experimental failure load of this model and the segment FEM were compared.

Chapter 1. State of Art

1.1 Introduction

This chapter focuses on presenting the research subject and a review of the literature related with the assessment of bone strength and bone fracture risk. This review will cover anatomical, clinical and biomechanical aspects of the subject. A special focus will be done on the radius.

First, biological and anatomical notions are remembered. The structure and function of the involved components are explained, from the micro level to the macro level. The next subchapter explains the epidemiology of the fragility fractures.

Then, the bone fragility assessment is presented. Two approaches are discussed: clinical and research. The mains techniques used on each approach are presented.

Finally, we discussed the prediction capability of the different techniques and we stated our hypothesis for its improvement.

1.2 Anatomy

1.2.1 Anatomical Planes

Before describing the bones of the skeleton, it is important to remember the main conventions to localize and position body parts. They are shown in the Figure 1-1

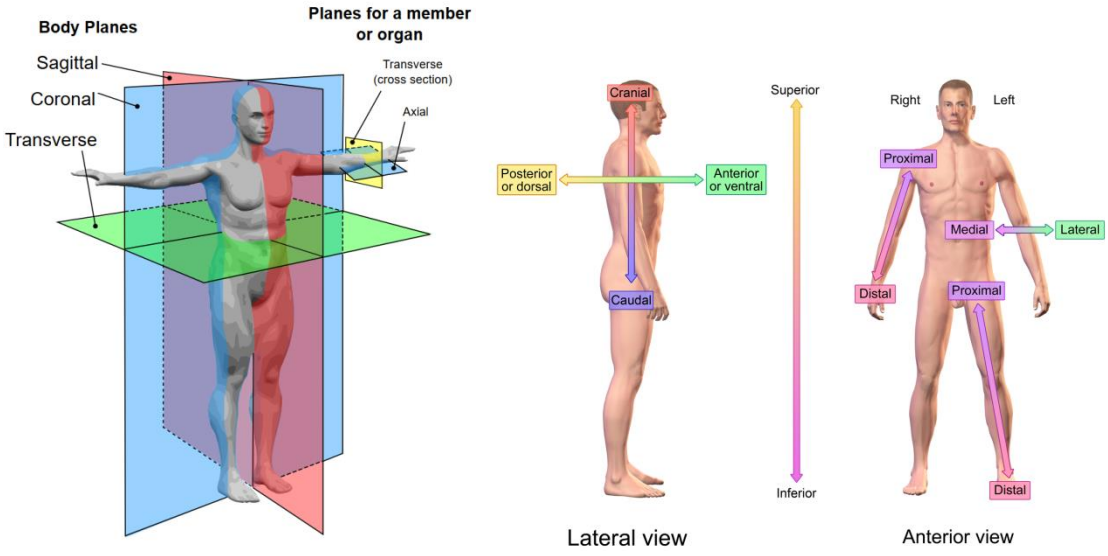

Figure 1-1 : Convention for the localization and position of the human body parts.
Ilustrations: Jordi March i Nogué & Blausen.com staff: "Blausen gallery 2014"

1.2.2 The Bones

Bones are rigid organs that constitute the skeleton. The human skeleton is formed by 206 bones, which provide the framework of the body. Bones support and protect the soft organs of the body. As a tissue, it consists in an intercellular calcified matrix, containing collagen fibers and different types of cell. The bone is a reservoir for calcium and phosphorus and a container for blood-producing cells (Drake et al. 2014).

Bones goes constantly through a modeling process (reshaping and resizing), to adapt the structure to loading. It also undergoes a remodeling process to remove old, and to repair micro-damages by replacing with new stronger bone and keep bone strength (Frost 1994). The appreciation of this phenomena were stated by Wolf, in the law carrying his name: *"Every change in the form and the function of a bone or in the function of the bone alone, leads to changes in its internal architecture and in its external form"*(Wolff 1986).

The bone has two components: the cortical bone and the trabecular bone. The cortical bone is a dense bone which corresponds generally to the exterior shell of the bone. It surrounds the trabecular bone and the marrow. The trabecular bone, which is a network of trabecular plates and rods sprinkled in the marrow (Carter & Hayes 1977).

Cortical bone is recovered by the periosteum, which is a fibrous connective tissue surrounding bone (Figure 1-2).

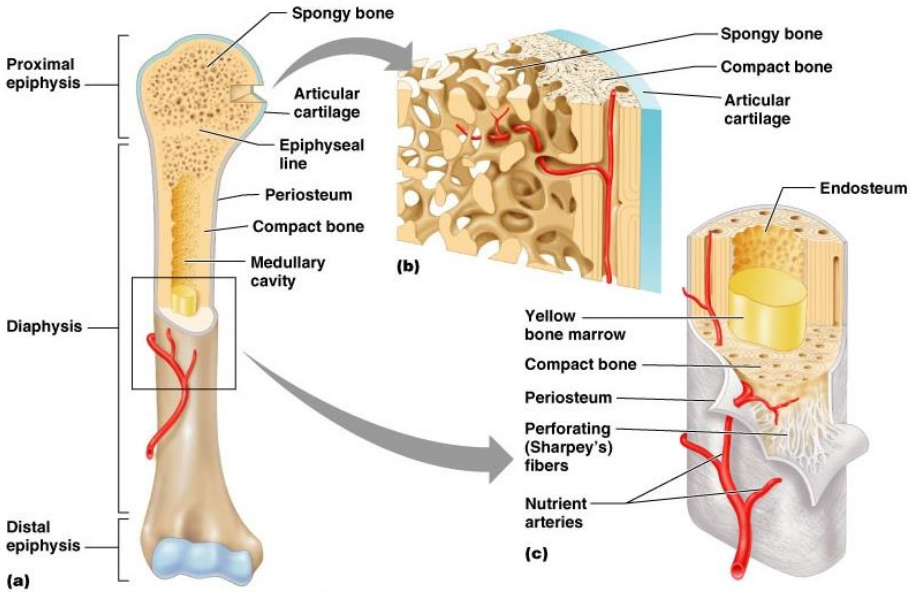

Figure 1-2 : Long bone structures. *Ilustration: Pearson Education, Inc., publishing as Pearson Benjamin Cummings*

1.2.3 The Radius

The assembly of bones forms the skeleton, which can be divided in two groups: the axial skeleton (cranium, vertebral column, ribs and sternum) and the appendicular skeleton (upper and lower limbs). This subdivision of the skeleton can be seen in the Figure 1-3

The upper limb can be sub-divided in arm, forearm and hand. The radius is located on the lateral side of the forearm between the elbow and the wrist joints. It forms the elbow joint on its proximal end with the humerus and the ulna (Figure 1-4).

Figure 1-3 : Human Skeleton. *Illustration: Gray's anatomy for students, 2nd Edition*. (Drake et al. 2014)

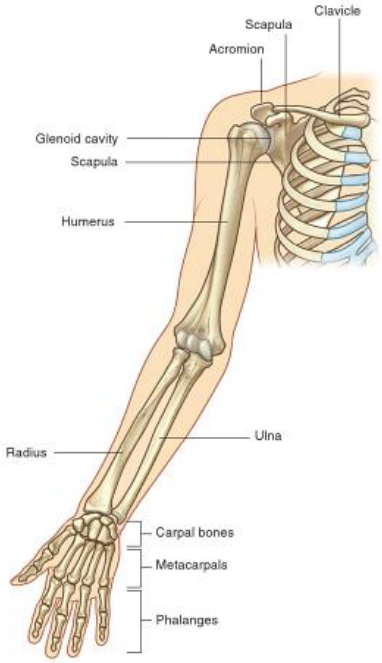

Figure 1-4 : Bones in the upper limb. *Illustration: Gray's anatomy for student, 2nd Edition.* (Drake et al. 2014)

The distal radius has a quadrilateral form. It has two articular surfaces (one for the carpal bones and one for the ulna). The carpal articular surface is marked by two facets for the scaphoid and lunate. The surface for the ulna, also known as the ulnar notch, is narrow, concave and smooth, and articulates with the head of the ulna. The other surfaces are the volar, dorsal and lateral surface (Figure 1-5).

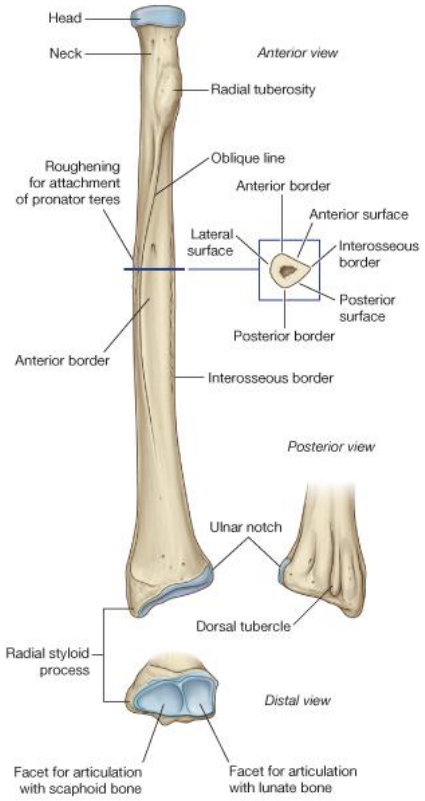

Figure 1-5 *:* Anatomy of the radius. *Illustration: Gray's anatomy for student, 2nd Edition.* (Drake et al. 2014)

1.3 Epidemiology of Fragility fractures

A fragility fracture results from a low trauma event, such as fall from standing height or less (Marshall et al. 1996). This kind of fracture is usually associated with osteoporosis. According to the World Health Organization, the osteoporosis is a disease characterized by low bone mass and microarchitectural deterioration of bone tissue, leading to enhanced bone fragility and consequent increase in fracture risk. This disease affects 75 million people in the United States, Europe and Japan and is the cause for at least 8.9 million fractures annually worldwide. The estimated lifetime risk for osteoporosis is between 30 and 40% (World Health Organization 2004).

The awareness about the high morbidity and mortality associated with osteoporotic fractures had existed for many years. However, prevention, diagnosis, and treatment only found really progress after the quantification of the osteoporosis by the quantification of the bone mineral density (BMD). The BMD is used to define a threshold of fracture, which means a cut-off value which attempts to capture most of the patients with osteoporotic fractures (Kanis 1994).

Different pharmaceutical treatments have been proposed for the treatment of the osteoporosis. One of the most common treatments is based in the use of bisphosphonate (Briot et al. 2014)(Roux & Briot 2014). However, this thesis does not focus on the pharmaceutical treatments, but mainly in the diagnosis methods involving biomechanical methods.

1.4 Bone fragility estimation in clinics

1.4.1 Dual-energy x-ray absorptiometry

The measure of the BMD is done using a Dual-energy x-ray absorptiometry scan (DXA). In this scan, two x-ray beams with different energy levels are focused at the patient's bones. The absorption depends at the same time of the quantity and nature of the traversed material. One of the two energies will be mainly absorbed by the soft tissue, and the other one by bone. After soft tissue absorption is subtracted, the BMD can be determined. As the DXA is a measure in a 2D projection, the BMD measure indicates the amount of mineral per square centimeter of bone. (Genant et al. 1996; Blake & Fogelman 2007)

Clinical practice using this scan has been available since 1987 and it has been used to prove effectiveness of different pharmaceutical product to prevent bone loss (Blake & Fogelman 2007).

According to the World Health Organization, osteoporosis is defined as a BMD that lies between 2.5 standard deviations or more, below the average value for young person (T-score of <-2.5)(Kanis 1994). This value applies for measures on spine, hip and forearm. A detailed description of classification, according to the World Organization Definition is shown in Table 1-1 (Blake & Fogelman 2007).

Terminology	T-score definition
Normal	T ≥ -1.0
Osteopenia	-2.5 < T < -1.0
Osteoporosis	T≤ -2.5
Established osteoporosis	T≤ -2.5 with presence of one or more fragility fracture

Table 1-1 : The World Health Organization definitions of osteoporosis and osteopenia, used to interpret DXA scans in postmenopausal women. (Kanis 1994).

The T-score is calculated using the Equation 1-1. It estimates the difference between the measure of BMD in a patient and the mean BMD in a healthy young population, and is expressed as a standard deviation.

$$\text{T-score} = \frac{\text{Measured BMD} - \text{Young adult mean BMD}}{\text{Young adult population SD}}$$

Equation 1-1 : T-Score estimation.

An example of a DXA test report for a forearm is presented in Figure 1-6. The value measured of BMD is compared with data of a specific population.

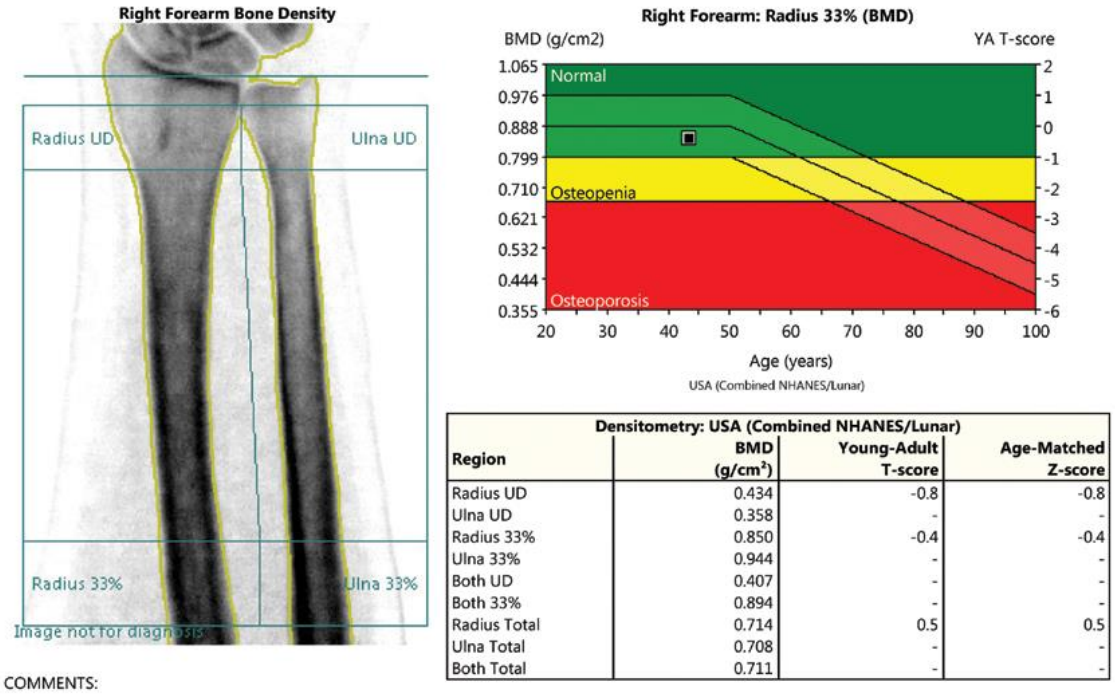

Densitometry: USA (Combined NHANES/Lunar)

Region	BMD (g/cm²)	Young-Adult T-score	Age-Matched Z-score
Radius UD	0.434	-0.8	-0.8
Ulna UD	0.358	-	-
Radius 33%	0.850	-0.4	-0.4
Ulna 33%	0.944	-	-
Both UD	0.407	-	-
Both 33%	0.894	-	-
Radius Total	0.714	0.5	0.5
Ulna Total	0.708	-	-
Both Total	0.711	-	-

Figure 1-6 : Example of a forearm DXA Report. *Renée Newman, 'avoidboneloss.com'*

Nevertheless, the DXA presents some problems for the detection of individual with high risk of fracture. Indeed, DXA have been reported as a test with a high specificity, but low sensitivity (Kanis 1994). Thus, when osteoporosis is detected, the prediction of the risk of fracture is high, but if the measure of BMD is normal, this prediction remains uncertain. It has been shown that, 50% of fractures are presented in patient diagnosed as non-osteoporotic by DXA (Siris et al. 2004)

1.4.2 Computed tomography scan

The Computed tomography (CT-scan) is not a standardized method used in clinical practice for the assessment of bone fragility. Nevertheless, it is frequently used to evaluate the complications associated with major fractures. On the other hand, scanner imaging is a very common source of data to develop different models to predict bone strength (Subchapter 1.5.6).

The CT-scan uses a computer-proceeded combination of a series of X-ray images, taken from different angles, to produce cross sectional images of a specific area. The CT scan

generates a volume of data that can be manipulated to detect different body structures. An example of a CT-scan and a cross-sectional acquisition (Figure 1-7)

Figure 1-7: CT-Scan Phillips ingenuity and one acquisition example of the distal radius (*Acquisition from the manufacturer – 'healthcare.philips.com'*).

One of the advantages of the CT-scan over a traditional X-ray radiography is that the CT-scan eliminates the superposition of images of structures outside the area of interest. Also, the CT-Scan presents an inherent high-contrast resolution, which is useful to differentiate tissue by its density.

The acquired stack of images can be analyzed in the 3 mains anatomical planes: Axial, sagittal and transverse, but also, on oblique planes when defined by the user.

1.4.3 The High Resolution peripheral Quantitative Computed Tomography

The High Resolution peripheral Quantitative Computed Tomography (HR-pQCT) (Figure 1-8) evaluates bone architecture and gives a range of bone mineral density of the bone (Rietbergen et al. 1995) (Figure 1-9). It has been used for clinical research trials, but its use as a clinical diagnostic method is not implemented.

Figure 1-8 : XtremeCT: High Resolution peripheral Quantitative Computed Tomography HR-pQCT, by SCANCO (Zürich, Switzerland)

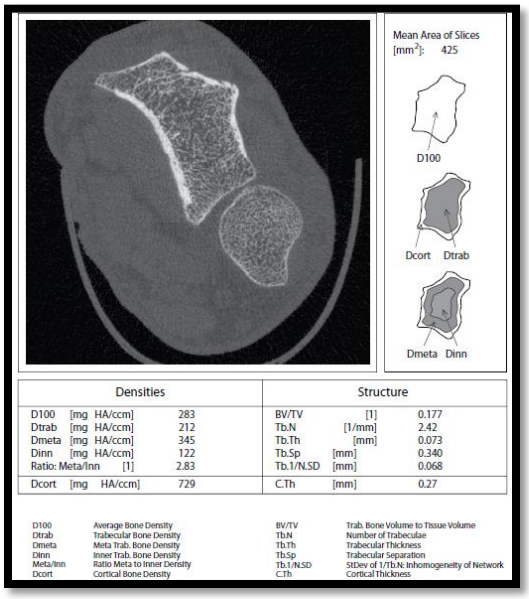

Figure 1-9 : Example of a HR-pQCT analysis result for a radius, showing density an architecture measures.

In vivo, this scanner evaluates peripheral sites (distal radius and distal tibia). It has two-dimensional detector (1536*127) pixels of 82 microns, which faces an X-ray tube (conical beam, 60 kV, 900 µA, spot size at the focal point: 80 microns). It allows the simultaneous acquisition of 110 parallel slices of 82 microns in 3 minutes, which corresponds to a reconstruction of 9 mm thick. The actual irradiation is very low and amounted to 3 µSv per examination. The 3D data set provided by the HR-pQCT allows the separation of analyses of trabecular and cortical bone at peripheral sites (Vilayphiou 2012).

Measurements are performed in the non-dominant member being inserted into a carbon fiber shell to maintain the position inside the scanner. A scout view is performed prior to manually set a reference line at the plateau of the distal radius or tibia. The measurement area is located 9.5 mm and 22.5 mm proximal to the reference line for radius and tibia, respectively.

1.4.4 The FRAX

Thus, for the past years, one of the main concerns in the field has been the determination of others factors contributing to predict the fracture risk. In order to determine those, meta-analysis studies have been implemented using 12 prospectively studied population-based cohorts from several geographic territories. Some of them are the age, the sex, the bone turnover, lifestyle and family history. After this rigorous analysis, over more than 250 000 patients, an algorithm of fracture risk have been established and condensed in a survey called FRAX. The FRAX estimates fracture risk over 10 years. The risk factors are (Kanis et al. 2008): Age, Sex, Weight, Height, Previous fracture, Parent fractured hip (this enquires for a history of hip fracture in the patient's mother or father), Current smoking, Glucocorticoids (currently exposure to oral glucocorticoids), Rheumatoid arthritis (confirmed diagnosis), Secondary osteoporosis (strong disorders associated with osteoporosis: diabetes type I osteogenesis imperfecta in adults, untreated long-standing hyperthyroidism, hypogonadism or premature menopause, chronic malnutrition, or malabsorption and chronic liver disease), Alcoholism and Bone mineral Density (Figure 1-10).

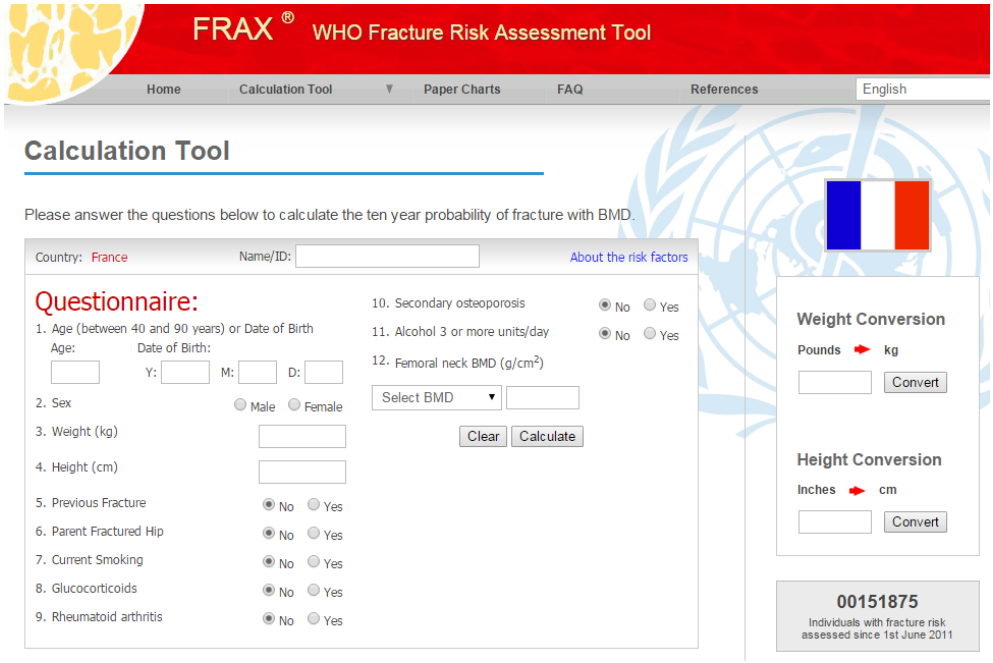

Figure 1-10 : FRAX, as presented in the web calculation tool.
https://www.shef.ac.uk/FRAX/tool.aspx?lang=en

FRAX did not consider the fall as a risk factor. There is no external mechanical influences considered into the algorithm. Thus, FRAX can do assumption about the fracture risk based on intrinsic properties, but will not assess the risk of fracture in a fall case, for example.

1.4.5 Distal radius fractures description and classification

Radius fractures have been described by Pouteau since 1783 (Belloti et al. 2013). When the description of almost all kind of fractures was done, authors have tried to classify the fractures in order to determine the complexity of the lesions and their treatment. Fernandez has presented a detailed description of the evolution of this classification and he proposed their own classification, which is more mechanically related (Fernandez 2001). Before we get to the classification, it is needed to explain the traditional description of the fractures. This have been well resumed by Segaren and Cresswell (Segaren & Cresswell 2013):

Colles' fracture: Extra-articular distal radius fracture with dorsal comminution, angulation, displacement, radial shortening and supination.

Smith's fracture: Distal radius fracture with volar displacement

Barton's fracture: Displaced, unstable articular fractures ubluxation of the distal radius with displacement of the carpus along with the articular fracture fragment. These may be either dorsal or volar

Chauffeur's fracture: Fracture of the radial styloid. May be associated with displacement of the carpus and may be the only bony component of perilunate injury.

Die-punch fracture: Intraarticular fracture with depression of the dorsal aspect of the lunate fossa.

The problem with this classification happens principally when an intra-articular disruption is misdiagnosed. For example, in the case of a slight die punch fracture, that can be simply diagnosed as a Colles' fracture. Then, researchers have proposed to use different classifications which, in some cases, denote a wide spectrum of fractures, using an alpha-numerical system (Fernandez 2001)(Laulan et al. 2007).

Nevertheless, most of those classifications tend to be anatomical descriptions. In this work, we are interested also in a description which emphasizes distal radius fracture according to their biomechanics. This was the work done by Jupiter and Fernandez, who used a biomechanical description of the fractures in order to get a classification which predicts stability of the fracture and giving recommendations for the treatments (Jupiter & Fernandez 1997)(Belloti et al. 2013). Details can be seen in Table 1-2.

Fracture types (adults) based on the mechanism of injury	Children fracture equivalent	Stability/ instability: high risk of secondary displacement after initial adequate reduction	Displacement pattern	Number of fragments	Associated lesions carpal ligament, fractures, median, ulnar nerve, tendons, ipsilat, fx upper extremity, compartment syndrome	Recommended treatment
Type I Bending fracture of the metaphysis 	Distal forearm fracture Salter II	Stable Unstable	Non-displaced dorsally (Colles–Pouteau) Volarly (Smith) Proximal Combined	Always 2 main fragments + Varying degree of metaphyseal comminution (instability)	Uncommon	Conservative (stable fxs) Percutaneous pinning (extra- or intrafocal) External fixation (exceptionally bone graft)
Type II Shearing fracture of the joint surface 	Salter IV	Unstable	Dorsal Radial Volar Proximal Combined	Two-part Three-part Comminuted	Less uncommon	Open reduction Screw-/plate fixation
Type III Compression fracture of the joint surface 	Salter III, IV, V	Stable Unstable	Non-displaced Dorsal Radial Volar Proximal Combined	Two-part Three-part Four-part Comminuted	Common	Conservative closed, limited, arthroscopic assisted, or extensile open reduction Percutaneous pins combined external and internal fixation Bone graft
Type IV Avulsion fractures, radial carpal frature dislocation 	Very rare	Unstable	Dorsal Radial Volar Proximal Combined	Two-part (radial styloid ulnar styloid) Three-part (volar, dorsal margin) Comminuted	Frequent	Closed or open reduction Pin or screw fixation Tension wiring
Type V Combined fractures (I–II–III–IV) high velocity injury 	Very rare	Unstable	Dorsal Radial Volar Proximal Combined	Comminuted and/or bone loss (frequently intra-articular, open, seldom extra-articular)	Always present	Combined method

Table 1-2: Fracture classification of the radius by Fernandez (Fernandez 2001).

1.5 Bone fragility estimation in research

This subchapter presents the definitions and methodologies related to the creation of models for assessing bone fragility. We presented on this subchapter different models presented in literature.

1.5.1 Mechanical Definitions

The **Stress** is the ratio between the applied force and the cross sectional area where the force is applied. The **Strain** is the ratio of change in dimension to the original dimension. The ratio between tensile stress and tensile strain is called the **Young's modulus** or elastic modulus.

The **strength** of a material is defined as the ability of a material to sustain loads. The stronger the material, the greater the load it can withstand. So it is the ability of the material to withstand stress without failure.

The **Poisson ratio** is the ratio between the transverse contraction strain and the longitudinal extension strain.

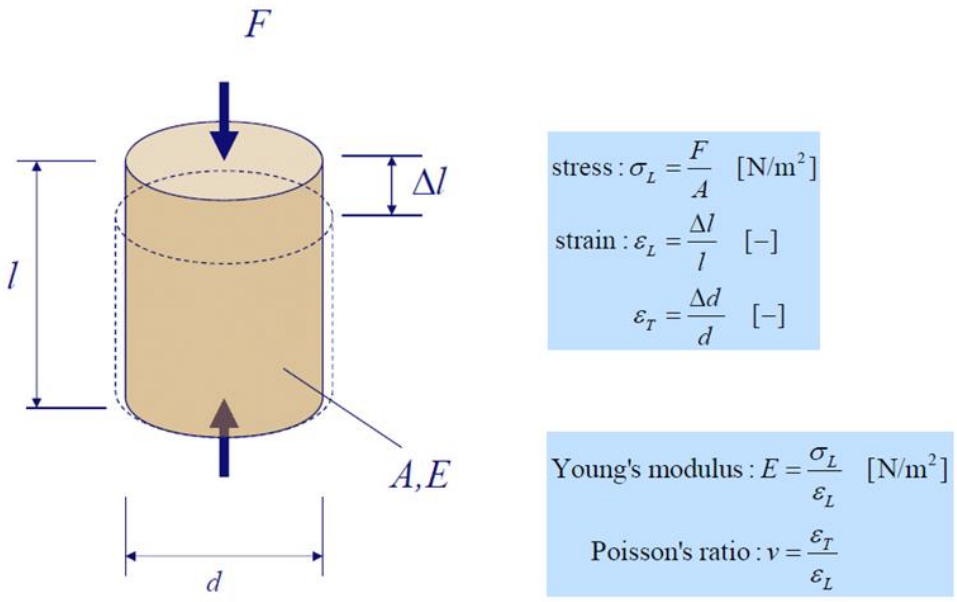

Figure 1-11 : Mechanical definitions. *Illustration: van Rietbergen, CISM summer course 2013.*

The **failure load** is the force needed to reach the fracture of a material.

1.5.2 Bone Imaging

The classic procedure to deduce the mechanical properties that will be used in a bone model is to use the data from a CT scanner. First, the **grey levels** (Hounsfield units+1000) measured by the scanner are used to deduce the Hydroxyapatite density of each voxel of the sample. Then, the density of hydroxyapatite is used to deduce the apparent density Using this value (Schileo et al. 2008), it is possible to deduce an approximate value for the Young's Modulus.

It is important to know that the measured valued of grey levels in a CT are influenced by some image artifacts, as beam hardening, so, this technique can give only a qualitative

information of the mineral content (Ruffoni & Lenthe 2011). Nevertheless, this technique has become widely used and models created using this technique have shown very good bone strength prediction (R^2>0.9) (Schileo et al. 2007a)(Christen et al. 2014).

The most common equations to do these conversions have been evaluated by (Bhatia et al. 2014), and are shown in Equation 1-2.

$E = 10.500\rho_{ash}{}^{2.25}$ (Keller 1994)
$E = 3.790\rho_{app}{}^{3}$ (Carter & Hayes 1977)
$E = 6850\rho_{app}{}^{1.49}$ femoral specimens (Morgan et al. 2003)
$E = 8920\rho_{app}{}^{1.83}$ pooled specimens (Morgan et al. 2003)
$E = 10.095\text{x}10^{-3}\rho_{HA}$ (Duchemin et al. 2008)

$\rho_{app} = \rho_{HA}/0.55$ Helgason et al 2008
$\rho_{app} = \rho_{HA}/0.626$ (Dalstra et al. 1995)
$\rho_{ash} = \rho_{app} * 0.6$ (Schileo et al. 2008a)

Equation 1-2 : Set of equations to estimate the Young's modulus of bone tissues.

E is the Young's modulus expressed in MPa. ρ_{ash} (ash density), ρ_{app} (apparent density) and ρ_{HA} (calcium hydroxyapatite equivalent density density) are expressed in g/cm^3.

The ash density is an indicator of the mineral content of bone tissue providing stiffness and strength to the tissue (Mosekilde et al. 1987).

The mineral content can be estimated from clinical scanner acquisitions, by using a **Phantom**. A Phantom is a calibration instrument which is scanned alongside with the patient or the sample. The phantom has inserts (generally presented as cylindrical rods) of a material with a known value of density. The more common rods are equivalent insert with a known value of density of Hydroxyapatite (HA), dipotassium phosphate (K_2HPO_4) and water. An example of a calibration phantom is shown the Figure 1-12.

Figure 1-12 : Calibration Phantom (Mindways Software, US). This Phantom has insert equivalents of water and K_2HPO_4

Thus, by using a calibration phantom, it is possible to obtain calibration curves relating the Hounsfield units (measured by the scanner) and the density of the bone mineral content.

The **Hounsfield scale** is a linear transformation of the original linear attenuation coefficient (μ) of a scanner. The Hounsfield scale is defined in the Equation 1-3.

$$HU = 1000 \ \frac{\mu - \mu_{water}}{\mu_{water} - \mu_{air}}$$

Equation 1-3 : Hounsfield Scale.

In this new scale it is assumed that distilled water in normal conditions of pression and temperature (0°C and 1 atm) has a coefficient of attenuation of zero. In the case of the air, the value is -1000.

1.5.3 Topology and Material properties

The acquisition made by a scanner device needs to be segmented to deduce the geometry of a bone model. The segmentation consists in the selection of the voxels considered as bone. This selection can be made by fixing a global threshold visually (Mueller et al. 2009). This method is operator-dependent. Other option is the use of a calibration curves to fix a threshold based on a density value (of HA or K_2HPO_4). More complex operations used to the segmentation include filtering algorithms (Boutroy et al. 2008), and adaptive thresholds (which applies local thresholds based on local density distributions, Bruker CtAn).

The correct segmentation of the bone is important because the bone fragility not only depend on the mineral content in the bone, but also on its microarchitecture. The bone

micro-architecture is a term which describes the interconnected network of trabeculae in the bone (Parfitt et al, 1992).

In the case of the HR-pQCT there is a standardized method to segment the bone using a sequence of filters. It uses a 3D Laplace hamming filter and a fixed global threshold (Laib & Rüegsegger 1999). These segmentations lead to binarized images, in which the bone is assumed as a homogeneous material. An average Young's modulus will be assigned to the whole bone. It has been shown that this approach is valid mostly in cases with a very low resolution, up to 30µm (Bevill & Keaveny 2009). In the standard HR-pQCT segmentation, the Hamming cut-off frequency is set to 0.4 of the Nyquist frequency, the weighting factor is 0.5 and the threshold is set to 400/1000 of the maximal gray scale value. (Christen et al. 2014). An adaptive threshold option exist also in the software CT-An, which is a software to manage the CT-Scan by Bruker (version 1.13.5.1). There are three adaptive options: median C, where the threshold is calculated as a median of all pixel/voxel grayscales, within a selected radius. In the adaptive mean C, The threshold is calculated as the mean of all pixel/voxel gray scales within a selected radius. Finally, the mean of min and max values, estimates the threshold using the mean, of the minimum and maximum value, of all pixel/voxel grayscales, within a selected radius

When using this type of segmentation, a heterogeneous model can be created. The model will be the results of several layers of mapping. Each layer will have a particular bone density and a particular Young's modulus.

This is the case of several FEA. They have used a mapping based on the relation between density and Young's modulus (Morgan et al. 2003). Some studies have also follow their own segmentation method to separate cortical and trabecular bone.. As an example, two Young's moduli where assigned to the bone, 19.3 and 590 MPa for the cortical and trabecular bone respectively (Taddei et al. 2006).

For the most part of the clinical CT-scans, it is possible to find a relationship between grayscale, Hounsfield units and Young's modulus. Nevertheless, some scans, as the Conebeam CT (CBCT) can only establish this relationships by using linear coefficients attenuations as an intermediate step (Mah et al. 2010).

However, most part of the models using the Morgan's relationship, were created using a CT clinical scan (Crawford et al. 2003)

A tool used for mapping bone mechanical properties using greylevels from images from CT-scan is the software called Bonemat, released by the Istituto Ortopedico Rizzoli in Bologna, Italy.

Another way to deduce material properties is to use the fabric values tensor, has it was made by (Pahr & Zysset 2009) and (Hazrati Marangalou et al. 2012) in femur studies on femur, using a CT-scanner.

The FEA using models from HR-pQCT use in general a homogeneous Young's modulus (10 GPa (Mueller et al. 2009; Ackerman et al. 2012) (Mueller et al. 2009) or 20 GPa (cortical) and 17GPa (cancellous) (Vilayphiou et al. 2011), depending on the failure criterion considered) .

Another Young's moduli are also used. For example, (Liu et al. 2010) has used a homogenous value of 15 GPa on a distal tibia analysis. In the study of (Mueller et al. 2011) a value of 6.829 GPa (MacNeil et al. 2012) was used for the analysis of the radius. This is a value lower than the used in most HR-pQCT studies. They found that the assignation of this value in the distal radius (specifically under the subchondral plate) allows a better estimation of the bone strength than the commonly used second stack from a radius HR-pQCT acquisition. This value can be justified in the very thin cortical bone found generally in the distal epiphysis of the radius.

In another radius and tibia study, (Jayakar et al. 2012) have studied the bone strength using 18 GPa for Young's modulus of cortical and trabecular bones. (Graeff et al. 2013), in a radius study which consider a fall loading condition has used a 15 GPa value as the Young's modulus for cortical and trabecular bones.

It can be seen that the choice of the segmentation and the material properties depends usually on the acquisition methods of the images, but also of the aim of the study.

1.5.4 Material law assumptions

Most part of studies considers the bone to have linear elastic properties, which means that there is a linear relationship between strain and stress, and an isotropic behavior, which means that the stress response, in each element, is the same in all directions. (Figure 1-13)

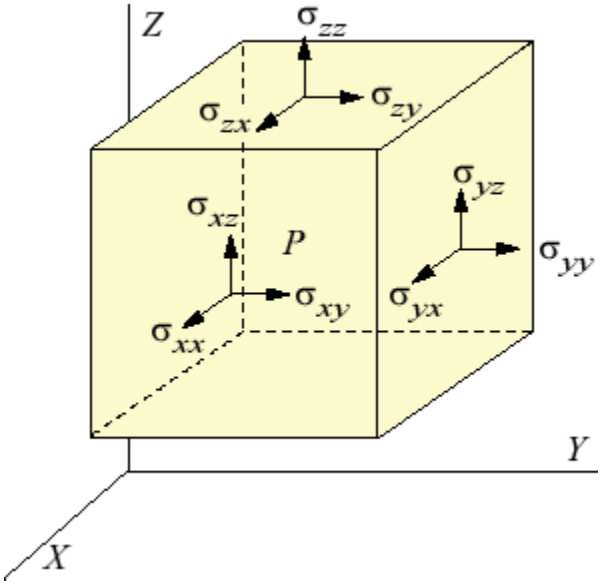

Figure 1-13 : Stress directions in a solid.

Nevertheless, there are some studies which evaluate the bone strength under a different assumption. For example, Varga et al. considered the cortical bone of distal radius as a non-linear orthotropic homogeneous material (Varga et al. 2009). In this study, the trabecular bone is considered as an isotropic non-linear homogeneous material, the properties were extracted from several nano-indentation studies. In the study of (Hosseini et al. 2012) on vertebra, the bone is considered isotropic, non-linear, and homogeneous. The level of prediction of bone strength by (Varga et al. 2009) and (Hosseini et al. 2012) with these non-linear models is given by a R^2 of 0.87 and 0.82. Higher values of prediction can be found in linear isotropic models. Nevertheless, it is not possible to determinate which one of the approaches would be more accurate to deduce bone strength. The decision when assigning the material properties will be always related with the application and aims of the study. On their study, Varga et al. stated that this kind of non-linear model does not require a high computational cost, on the contrary to the typical HR-pQCT Finite element analysis.

1.5.5 Meshing options

Depending of the CT scan technique and the operations over the images, the model will have certain element type and element size (Depalle et al. 2013).

The tetrahedral mesh and the hexahedral mesh might be the more common meshing options used in bone strength studies. The hexahedral mesh is commonly used when doing a direct conversion from voxel into element. This is the most common technique used in HR-pQCT studies. Some of the advantages of hexahedral meshes are their aspect ratio, which gives more stability under the simulations. Hexahedral meshes are particularly efficient in cases involving dynamic loading (Ruffoni & Lenthe 2011).

One of the most interesting options when using a hexahedral mesh is the possibility of assigning the material properties directly from the grey level assigned to the voxel.

A first problem when using hexahedral meshes would be connectivity between hexahedral mesh. This problem, which is caused by a partial volume effect, has been solved by most part of imaging software through their particular segmentation algorithm (Ulrich et al. 1998)

Hexahedral elements have been used by many authors, to create for example a generic and subject-specific finite element model of the upper femoral extremity (Duchemin et al. 2008). Only a few studies with acquisitions from HR-pQCT have decided to create models with a different meshing option (Varga et al. 2009). . These authors decided to use a tetrahedral mesh for the trabecular bone, and meshed the cortical bone with a penta (wedge) mesh. For the distal embedding they use a second order solid tetra mesh.

On the contrary, the tetrahedral mesh has been commonly used in models created from typical CT-scans. The tetrahedral mesh gives a smoothed surface and a good connectivity between elements. Studies using tetrahedral meshes of 1st order with 4 nodes (Hazrati Marangalou et al. 2012) can be found as well as others using tetrahedral meshes of 2nd order with 10 nodes (Schileo et al. 2007b)(Taddei, Martelli, et al. 2006).

The element shape is important, in order to ensure a correct aspect ratio. Although, it is also important to verify that the model adhere to the basic physical laws, such as the

conservation of the energy (Burkhart et al. 2013).Theoretically, models with very small element size (high number of elements) will have a better description of the sample, then, the behavior of this model would be closer to the reality. Nevertheless, there is no need of a very small value of element size to have a good prediction of bone strength (Gray et al. 2008) (Schileo et al. 2007b). For these studies the images were obtained using a typically CT-scan which do not perform a high resolution acquisition. Then, after the reconstruction, and meshing, the selected value of element size, when indicated, was around 2mm. They have successfully predicted the superficial strain with R^2 equal or superior to 0.9.

The synthesis of the parameters used to develop different finite element models of bone and their estimation results are given in the Appendix 3: FEM Parameters from CT-Scat and HR-PQCT for the finite element model created from CT-scan data, and created using data from HR-pQCT.

1.5.6 Risk of fracture definition

The risk of fracture is can be defined according to a mechanical point of view as shown in the Equation 1-4 (Hayes et al. 1991).

$$\varphi = \frac{External\ Load}{Bone\ strenght}$$

Equation 1-4 : Risk of fracture definition.

If this ratio is higher than 1, then, a fracture could occur.

This ratio has been used in several studies. It was used to deduce the potential mechanisms underlying vertebral fractures (Bouxsein et al. 2006) and also, as an effective method to explain age- and sex-specific incidence rates in fragility fractures of the hip (Riggs et al. 2005). In these studies, the external loads correspond to values found in literature from experimental protocols.

1.5.7 Failure criteria

The assessment of a failure criterion has been the aim of several studies. Two of the most common criteria are: Von Mises stress and maximum principal stress. The study of Schileo et al. on femur has compared this two classical approach with a criterion based in the

maximum principal strain (Schileo et al. 2008b). The models for this study where obtained using a classic CT-scan. The bone material was considered as heterogeneous (mapped using the ash density), with a linear and isotropic behavior.

To evaluate the capacity to identify the actual failure risk, the superficial area of failed elements was computed. They stated that an accurate model should predict a minimal amount of the bone surface failing for the application of the actual failure load. Then, to discriminate the better predictor they performed a comparison by plotting the experimental load against the failed area in the model (Figure 1-14).

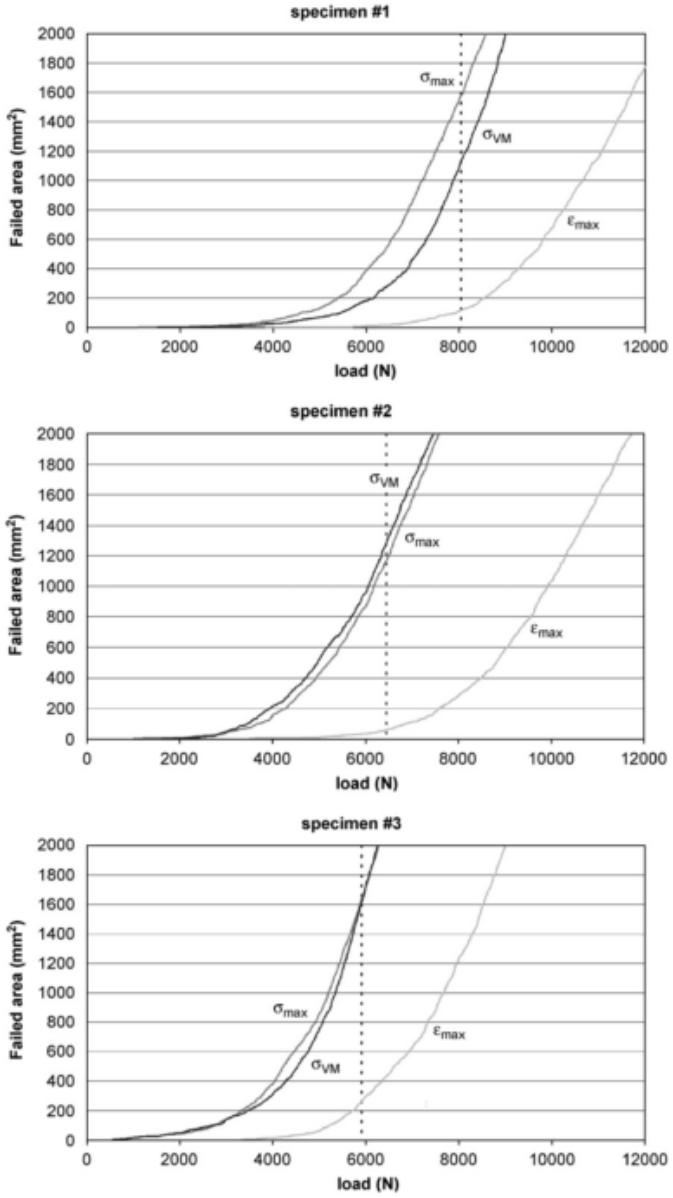

Figure 1-14 : Results from (Schileo et al. 2008), comparing Von Mises stress, maximum principal stress and maximum principal strain for the identification of fracture patterns.

They concluded that the proposed criterion of Maximum Deformation allows to identify fracture patterns in a femur in a stance configuration.

The HR-pQCT FEA uses the Pistoia's criterion (Pistoia et al. 2002) as a measure of fracture risk. This study was performed in cadaveric arms under axial-static loading conditions (Figure 1-15). They assumed that the bone failure would be initiated if a certain percentage of the bone tissue (varied from 1% to 7%) would be strained beyond the tissue yield strain.

Figure 1-15 : Experimental Setup from (Pistoia et al. 2002)

In this study, the tissue yield strain is taken as the tissue level effective strain, which is calculated as a function of the strain energy density U, and the Young's modulus E (Equation 1-5).

$$\in_{eff} = \sqrt{\frac{2U}{E}}$$

where:

$\in_{eff}$: Effective Strain

U : strain-energy density

E : Young's modulus

Equation 1-5 : Effective strain definition. Consistent units to be used for U and E.

They have chosen 7000 microstrains as the bone tissue strain value, based on the studies of (Niebur et al. 2000). They concluded that the bone will fracture when 2% of the bone is loaded beyond 7000 microstrains.

1.6 Discussion: Selection of the loading conditions

As presented in this chapter, the gold standard method for the clinical diagnosis of the osteoporosis and the evaluation of the risk of fracture is the Dual X-ray Absorptiometry (DXA)(World Health Organization 2004). Nevertheless, it has been shown that this measurement, which is an x-ray 2D projection, presents an insufficient sensibility, because 50 % of fractures occur in patients considered non osteoporotic (Siris et al. 2001).

Another method discussed in this chapter was the estimation using the FRAX (WHO Fracture Risk Assessment Tool), which integrates clinical risk factors. Nevertheless, this method was criticized because the falls and the disturbances of the walking were excluded from the algorithm of prediction (Chapurlat 2013). In other words, this survey cannot currently take into account the external loading conditions that increase the risk of fracture.

Several finite elements were also presented in this chapter as an alternative for the assessment of bone fragility. These models can be very accurate when measuring bone strength. The prediction can reach values close to 98% (Macneil & Boyd 2008).

However, comparisons of several finite element models (FEM) of radius in cohorts (Rietbergen & Ito 2015) have shown that, despite the good prediction of bone strength, it is not possible to confirm that the bone fracture risk prediction has been improved with the use of these models. As a matter of fact, it cannot be confirmed that prediction levels of these FEM are superior to those coming from a clinical standard examination by DXA.

The risk of fracture can be defined by the ratio between external load and the bone strength (Hayes et al. 1991). Thus, because the FEM estimate correctly the bone strength, a better consideration of the external load should lead to an improved prediction of the risk of fracture.

For most of the radius models (Pistoia et al. 2002)(Macneil & Boyd 2008)(Varga et al. 2009)(Mueller et al. 2011) the loading condition was a quasi-static axial load. However, in case of a fall, only 15 % of cases are associated with an axial load on the radius (Melton et al. 2010) (Figure 1-16).

Figure 1-16 : Possible falls from standing height (Melton et al. 2010)

The most common angle between the floor and the arm found in the forward fall is 75° (Greenwald et al. 1998) (Chiu & Robinovitch 1998) and the average velocity when the subject hits the floor is 2 m/s (Tan et al. 2006)(Troy & Grabiner 2007a). this fall case is represented if Figure 1-17.

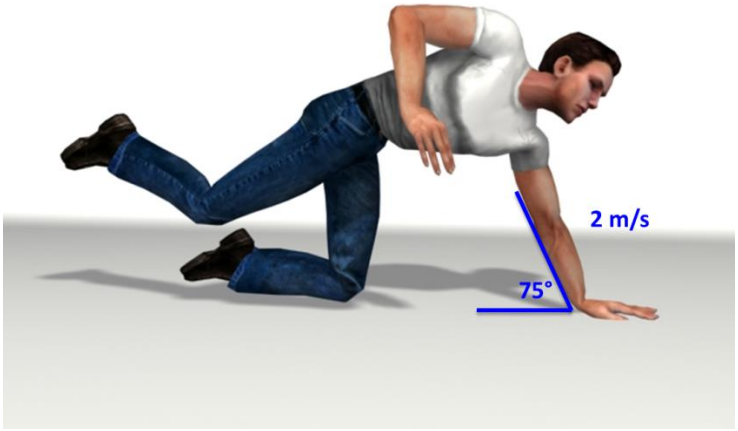

Figure 1-17 : Fall case of study: Forward fall with outstretched hand. The angle between the anterior face of the radius is 75 degrees and the velocity is 2 m/s.

In a previous study, about how the mechanical loading affect the ultimate behavior of bones, we deduced that the bone strength is sensitive to the orientation, position, speed and distribution (Eighth Bone Quality Seminar Proceedings 2013. 2014). The bone strength, however, have been estimated experimentally, in most of cases, by using quasi-static axial loadings. As a matter of fact, most of the fracture risk prediction models use also quasi-static axial loadings.

In consequence, we have made the hypothesis that a dynamic non-axial loading of the radius could be more discriminant of the risk of fracture. Other studies have also evocated the importance of the loading orientation in the assessment of the bone strength (Troy & Grabiner 2007b) and (Burkhart et al. 2014).

1.7 Conclusions and aims

We presented the different methodologies used to estimate the bone strength and the fracture risk, and the technical processing required to do these estimations.

It is well established that the FEM is a promising technique, and we hypothesized that numerical model prediction capability could be improved by considering realistic loading conditions, i. e, dynamic and non-axial. In this context the aims of the current work are:

Aim 1:

- To develop an ex-vivo experiment to reproduce a forward fall case on a human radius. This experiment will serve to evaluate the prediction capabilities of different finite element models

Aim 2:

- To evaluate the prediction capabilities of a radius segment model generated by HR-pQCT. This will be tested first for the standard axial configuration, and then, new non-axial configurations will be evaluated.

Aim 3:

- Evaluating the prediction capabilities of a FEM of the whole distal radius integrating dynamic and non-axial loading conditions.

Chapter 2. Experimental protocol to reproduce a forward fall leading to fractured and non-fractured radii

2.1 Introduction

As discussed in the previous chapter, we decided to evaluate the behavior of the radius under realistic loading conditions. We wanted to reproduce the case of a fall, in which the impact of the radius on the floor causes a fracture or not. Previous works evaluating fractured vs non-fractured cases on radius were made under not realistic conditions (axial loading)(Duma et al. 2003) and other using realistic conditions but compared pre-fracture and fracture cases under successive impacts (Burkhart et al. 2012). In this context, the aim of this study is to develop an ex-vivo experiment to reproduce the realistic conditions of a forward fall case, leading to fractured and non-fractured radii. This experiment will be helpful to evaluate the prediction capabilities of the finite element models presented in Chapter 3 and Chapter 4.

2.2 Methods

Thirty radii from elderly donors (50 to 96 y.o, ± 12 y.o, 13 males, 17 females) were considered. The bones were obtained after necropsy at the "Département Universitaire d'Anatomie - Rockefeller, Lyon, France". First, during the dissection, the 2/3 of the distal radius was cut and cleaned of soft tissues. The radii were then placed in a vacuum bag and frozen at -20° C before preceding any experiment. Before the experiments, the frozen bones were measured in DXA and scanned to retrieve the geometry of the bones to create finite element models: *1)* in a HR-pQCT (Scanco Medical, Switzerland) for the model described in Chapter 3, and *2)* in a Cone Beam CT (CBCT) (NewTom 5G - QR, Italy) for the model described in Chapter 4.

The day before the biomechanical experiments, bones were thawed using the following process. They were placed 16 hours at 4°C and then 6 hours at room temperature, while preparation took place. Proximal half of the previously cut radius were potted in a polyurethane resin (reference: 84A&B, Esprit Composite) in a steel cylinder (61 mm of diameter). Using a positioning laser, radii were potted with an alignment of 75° between

the anterior face of the radius and the ground (anterior face looking up), without any tilt in any other planes (Figure 2-1). This position reproduces alignment of the radius in the most common forward fall. The third part of the distal radius was exposed after potted.

Alongside with the radius, we also potted an aluminum cylinder. This cylinder will have landmarks on the surface in order to verify the global velocity of the system (Figure 2-1).

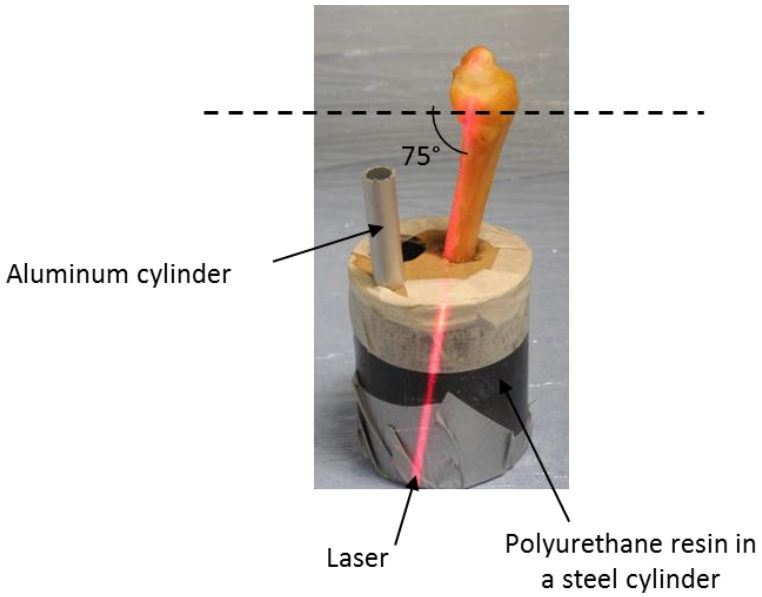

Figure 2-1 : Potting process of the radius. A positioning laser is used to set the radius in the forward fall case. The radius is potted in a polyurethane resin inside a metallic cylinder. An aluminum cylinder is also potted for general motion tracking purposes

Because the scaphoid and lunate are also both involved in the mechanism of fracture of the distal radius (Jupiter & Fernandez 1997), a rigid polyurethane mold was made to reproduce a simplification of this joint (scaphoid and lunate) for each articular surface of the radii. This process is shown in Figure 2-2. This mold attempts to distribute the loading uniformly on the articular surface of the radius during the impact. The steps for the construction of the articular mold are shown at the Figure 2-2. In summary, a shell of modeling clay was made surrounding the distal radius. Then, liquid silicone was sprayed over the articular surface. After that, the polyurethane resin was versed. Finally, when the resin has polymerized, the shell of modelling clay was removed. The fake white joint (called articular mold) was able to move and to be removed if needed.

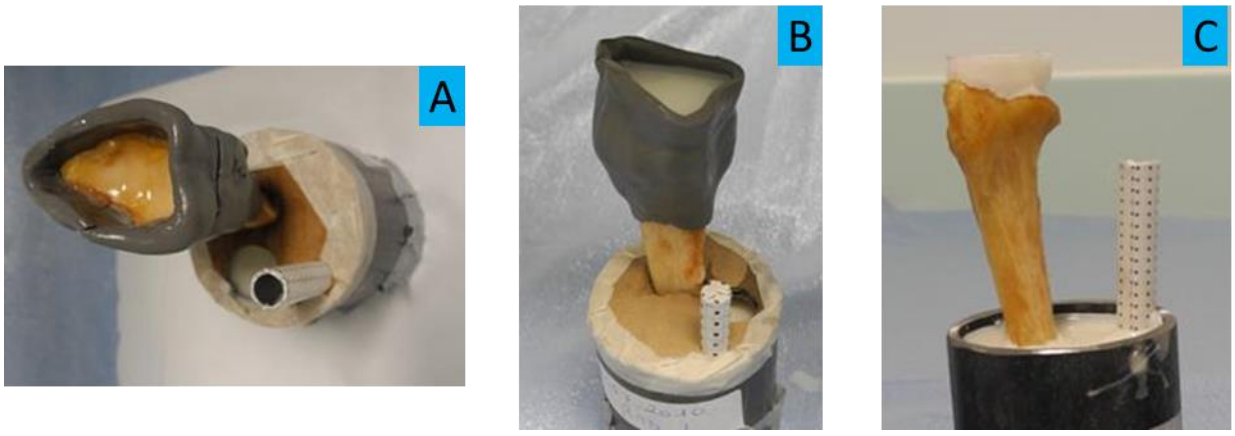

Figure 2-2 : Construction of the articular mold. A. Modelling clay shell is put on the distal radius to contain the resin. B. Polyurethane resin is versed. C. Modelling clay is removed.

Then, each radius was painted using a white makeup and a black painting pattern was made using a spray. This pattern allowed studying the surface strains using digital image correlations (Vic-3D, Correlated Solutions, Germany).

The articular mold was kept attached to the distal end of the radius using a silicon rubber. This silicon rubber kept the mold on the radius, but also allowed few displacements in perpendicular directions to the impact, as expected in real life Figure 2-3.

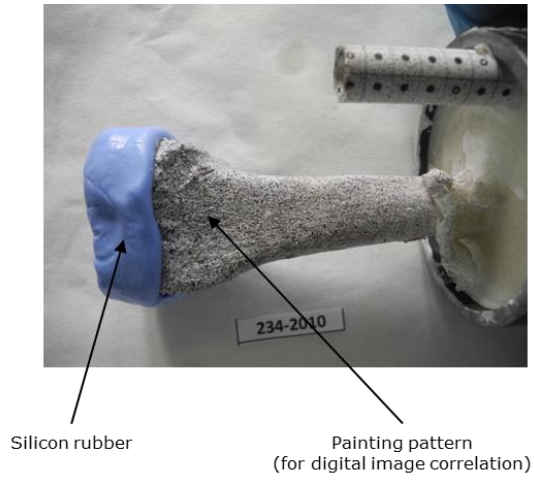

Figure 2-3 : Radius ready for test. A silicon rubber shell was used to hold the articular mold to the bone. A pattern was painted on the cylinder and on the radius to study surface strains using digital image correlations.

The pot was placed in a horizontal cylinder bar on a rail system, which was free to slide along the loading axis. This bar had a weight of 12.5 kg, which was an arbitrary value

representing the mass involved in a fall, i.e, a percentage of the body weight. This weight was the same for all the tests. A schematic of this experimental setup was shown on Figure 2-4.

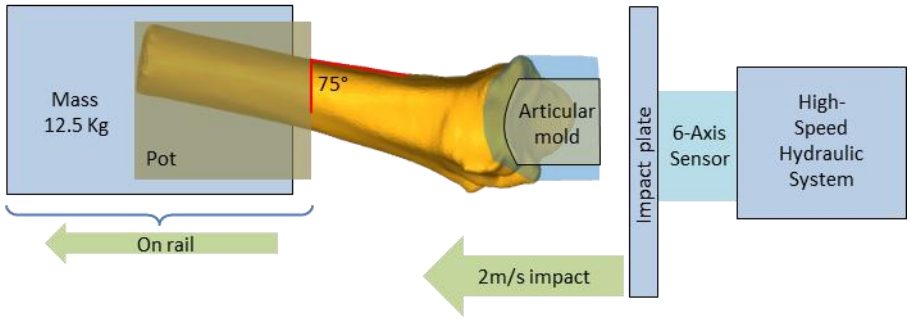

Figure 2-4 : Schematics of the experiment. This configuration loads the radius at 75° with a velocity of 2m/s, representing the forward fall case studied.

And the real experimental setup is depicted in the Figure 2-5.

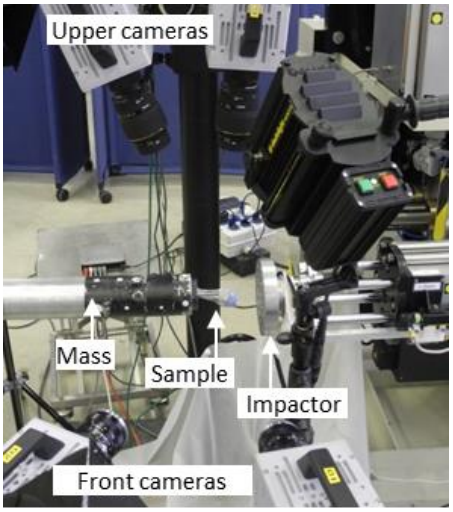

Figure 2-5 : Experimental set for testing the radii in a forward fall case configuration.

The instrumentation is detailed in the Figure 2-6. Four high-speed cameras (FASTCAM SA3, Photron, Japan) recorded the impact. Two cameras were placed facing the ulnar face of the radius, and recorded the test using 105mm F2.8 DG Macro sigma lenses. The other two cameras were placed facing the anterior face of the radius, and recorded the test using 50

mm Z1.4/50 mm ZF planar Zeiss lens. The cameras were set to record with a resolution of 1024x1024 pixels at 2000 images per second. Because of the velocity of the impact, it was necessary to set a high shutter speed on the cameras, which controls the exposure time on one frame. The drawback of taking very short exposure time is that the sample needs to be overexposed to light. The radii were then illuminated using three projectors (400D, Dedolight, Germany). Using this illumination, it was found that blurry images were avoided when using a shutter speed of 50µs.

Figure 2-6 : Main instrumentation on the ex-vivo protocol. A. Impact Machine (LF Technologies France), B. High-speed recording camera (FASTCAM SA3, Photron, Japan). C. Six-axis sensor (105515TF, Humanetics, Germany). D. projector (400D, Dedolight, Germany). E. Laser arm scan (Nikon, Japon). F. Positioning laser.

A six-axis sensor (105515TF, Humanetics, Germany) was tightened to the impactor. Velocities and positions were also obtained by instrumentation systems of the testing machine. Accelerations were obtained by adding an external accelerometer to the impact plate. The radius was then loaded through the mold at 2m/s using a hydraulic high speed testing machine (LF technologies, France). At the beginning of the test, the distance between the impactor and the mold was 50 mm. This distance allowed the acceleration of the impactor and stabilization of its speed to reach 2 m/s before impact. The displacement of the stroke was set to 10 mm before stops. The experimental final set-up is shown Figure 2-7.

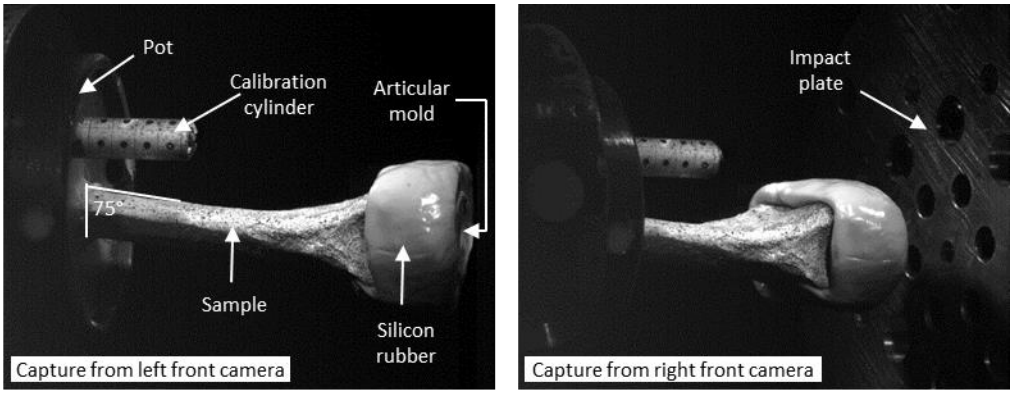

Figure 2-7 : Final set for the experimentations. Front cameras capture.

Two laser scans acquisitions were made. The first laser scan was made on the articular mold at the surface in contact with the articular surface of the radius. This procedure was performed before the fixation of the articular mold on the radius using the silicon rubber Figure 2-8. The second laser scan corresponds to the whole radius after positioning the pot into the cylinder, just before the impact. These two acquisitions were useful for the finite element model described in Chapter 4. The first one, of the articular mold, allows retrieving the loading surface on the radius, and the second one allows setting the finite element model in the same position as tested experimentally.

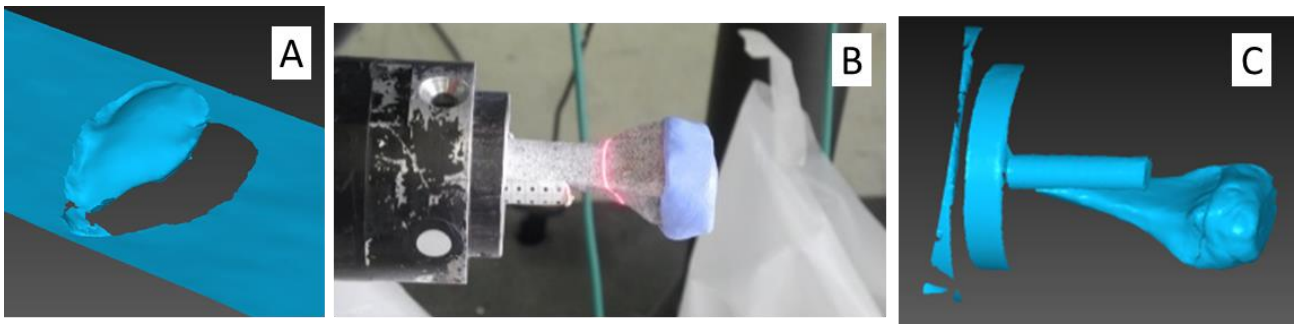

Figure 2-8 : Laser scan acquisitions using the laser arm Nikon. A. Surface acquired for the articular mold. B. Moment of acquisition on the radius after placement. C. Surface acquired for the radius after placement.

All the samples were impacted under the same conditions, expecting that some of them will fracture and others will not. According to rheumatologists at the Edouard Herriot Hospital in Lyon, the fracture of the radius could occur after several falls. In order to evaluate this, the impact was repeated if no fracture was detected. The maximum number of impacts for each bone was three.

2.3 Results

The main results of the experiment are: 1) Measurement of load over the time on the axial axis of the sensor, 2) the classification into two groups: experimentally fractured and not fractured, and 3) surface strains from the stereo-correlation analysis using the pattern painted on the radii.

2.3.1 Maximum Forces from the experiment

After the experiment, the forces, momentums and accelerations were saved in a .txt file. The data from this file must be treated before we can give a reaction force curve over the time and retrieve the maximum load on the test. The treatment of this curve considers the following steps: filtration, correction of parasite forces caused by the inertia of the moving mass, and finally, the correction of the initial offset. An example of the curve obtained from the six axis sensor (axial load) is shown in Figure 2-9. This untreated curve labelled as "Force" and is shown in green. The acquisition interval of this signal is $5x10^{-5}$ seconds. Then, 20 acquisitions is equivalent to 1 millisecond. The total number of acquisitions in the test is 10720, which is 535.95 milliseconds. Only the 100 ms around the impact are shown on the Force overtime curves in Figure 2-9.

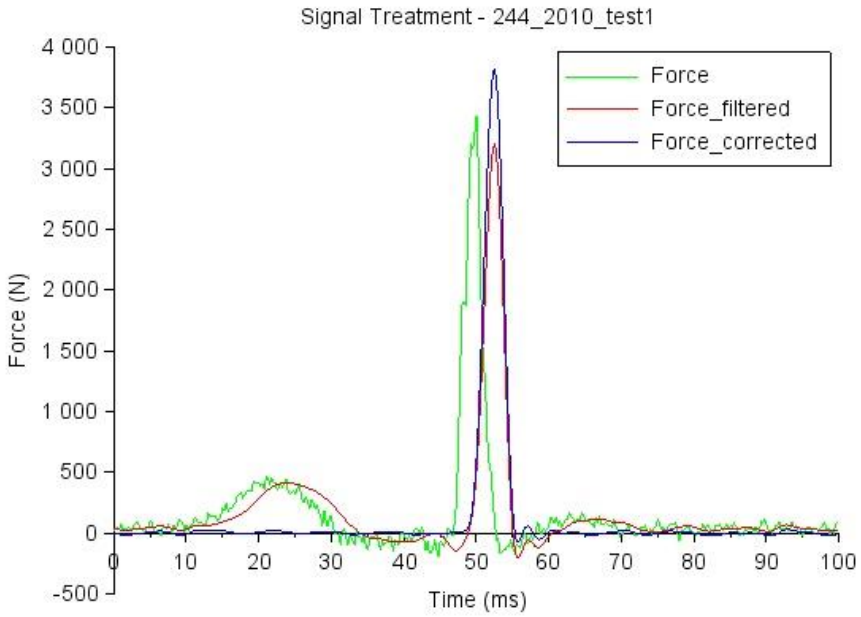

Figure 2-9 : Example of the treatment process of the curve obtained from the six axis sensor (axial load). The green curve, labelled as "Force" shows the raw data. The red curve, labelled as "force-filtered" shows the curve after the filtration process. The blue curve is the final curve, which is obtained after corrections of inertia and zero value measure. The graphic is centered at the maximum value of the untreated signal, and only shows 100 ms of the total acquisition.

The first treatment considers a frequency analysis. Using the Fast Fourier transform, implemented in Scilab as an external function (which is based on the Matlab algorithm), it is possible to evaluate the spectrum of frequencies making part of the signal. This frequency analysis is shown in the Figure 2-10. Noises are detected in the signal in the low frequencies. Nevertheless, there is also a dominant peak of high frequencies. After evaluating the frequency spectrums of all the 30 samples (which can be found in the annex 2), it was decided to build a Butterworth frequencies filter to processing this signal. The low peak attenuation frequency was set to 300 Hz and the high peak attenuation coefficient was set to 5000 Hz. The red curve labelled "Force_filtered" in the Figure 2-9 shows the result after applying this filter. There was a notorious improvement regarding the noise on the signal. There was also a translation of the curve over the temporal axis. This phase translation is a typical feature when using these kinds of band-pass filters. In our case, this did not affect the result, because we are interested in the maximum load.

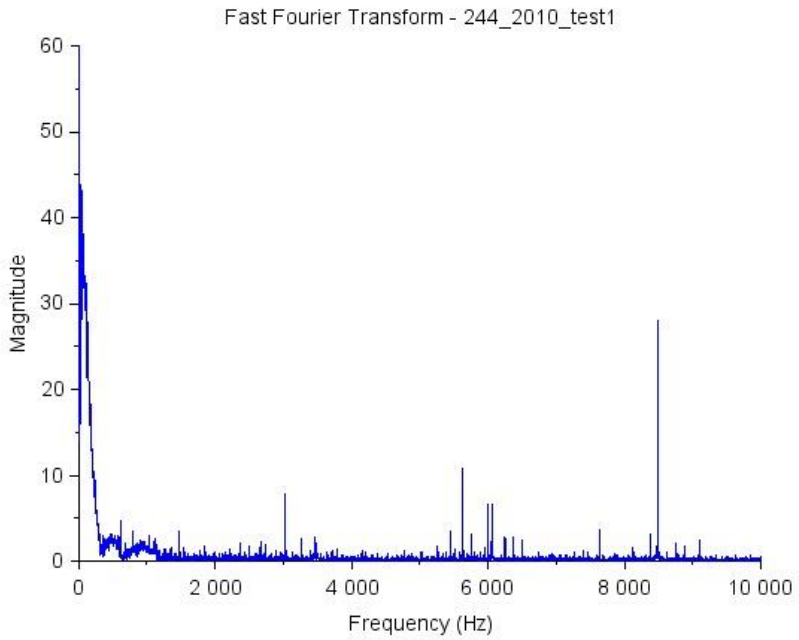

Figure 2-10 : Example of a Fast Fourier transform analysis of one of the samples.

In the force curve treatment, it was also necessary to retrieve the inertial load due to the moving mass (the impact plate and the six axis sensor). The instrumentation that caused this inertial load was weighted. These elements, which included: the impact plate, the screws and the six axis sensors, had a weight of 1.7 Kg. An empty impact test, i.e, without sample, was performed in order to retrieve the force and acceleration. If this weight influencing the parasite force is correct, then, its product with the acceleration curve should result in the curve of force measured by the six axis sensor.

As shown in Figure 2-9 the inertial load is correctly assessed.

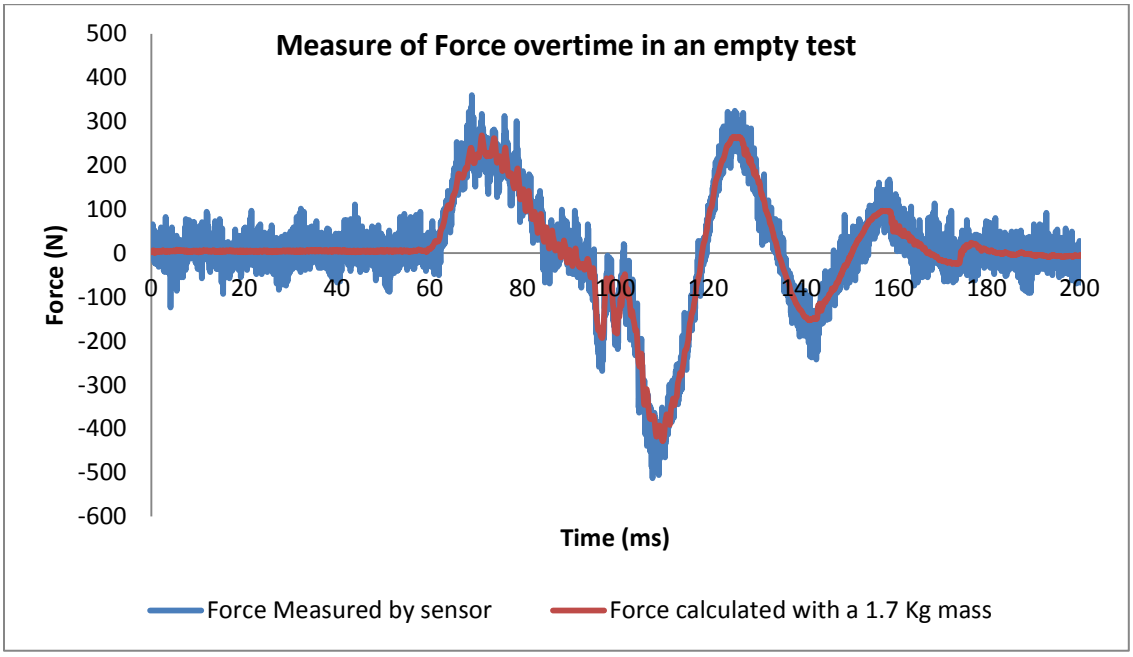

Figure 2-11 : The blue curve is the force measured without treatment, from the six axis sensor. The red curve corresponds to the product between the acceleration on the empty test and the weight of the components inducing parasite loads.

To correct the curve, the mass of 1.7 Kg was multiplied with the acceleration curve (filtered) of this test. Then, this inertial load was subtracted from the filtered load curve. The last correction was related to the measure of the zero value. It can be noticed that there was an offset of a few newtons on the filtered curve (Figure 2-11). To correct this, we took a zero value after the impact. Specifically, the script took the last 1720 acquisition values of the "force_filtered" curve, which corresponded to 0.086 milliseconds. On these acquisitions, the measured force was supposed to be zero. Then, the average of this offset was estimated, and this value was subtracted from the "force_filtered" curve. An example of the resulting force overtime curve, after processing and correcting the signal, is shown in the Figure 2-12. This graphics was centered at the maximum value of force and only shows 16 milliseconds surrounding the impact.

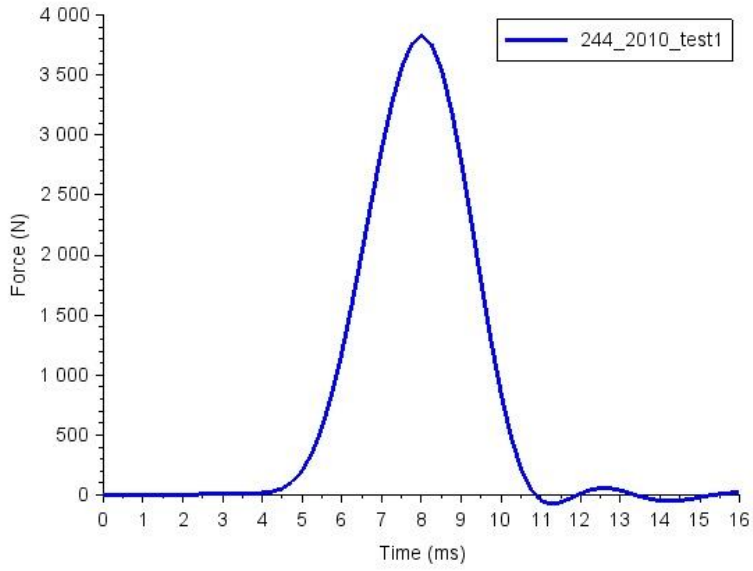

Figure 2-12 : Force overtime curve after processing and correcting the experimental curve.

From these curves, it is then possible to retrieve the maximal force for each impact. The results are shown in the Table 2-1.

Sample	Maximum Force (N) Test 1	Fx T1	Maximum Force (N) Test 2	Fx T2	Maximum Force (N) Test 3	Fx T3	No Fx	Type of Fracture
013_2010	849	Yes						Proximal
024_2011	2971	Yes						Colles
056_2010	4203		3419	Yes				Colles
057_2010	2182	Yes						Barton
067_2010	4178		5986		4656		Yes	
090_2012	3990		3817	Yes				Barton
121_2010	2927	Yes						Complex
138_2011	3674		4180		3720		Yes	
154_2012	3925		2825	Yes				Barton
161_2012	2206		1592		1186		Yes	
166_2012	2478		1623		1793		Yes	
203_2012	2697		1421		723		Yes	
204_2012	1965	Yes						Colles
206_2010	4344		3465		2216		Yes	
211_2010	2903	Yes						Barton
213_2009	3486		2953	Yes				Barton
214_2009	1777	Yes						Proximal

215_2009	5818		4759	Yes				Colles
224_2009	1692		1341		1250		Yes	
225_2009	2936		2616		2625	Yes		Colles
229_2009	1629	Yes						Colles
230_2009	6265		4234	Yes				Barton
232_2009	2634	Yes						Barton
233_2009	2178		1640		1898		Yes	
234_2010	2381	Yes						Barton
239_2010	1176	Yes						Colles
243_2010	2055	Yes						Complex
244_2010	3825	Yes						Barton
246_2010	1625	Yes						Colles
250_2010	3929		3137		2197		Yes	
Average Force ± SD (N)	2963 ± 1003		3063 ± 1062		2226 ± 864			

Table 2-1 : Maximum forces during the experiments. FX T*n* indicates there is detected fracture at the *n* test. The column "No FX" indicates if the sample did not experienced fracture after the three impacts. The last column indicates the type of fracture. The predominant types of fractures are Barton's and Colles'.

2.3.2 Fracture cases and type of fractures

Among the 30 radii, 14 had a fracture after the first impact, 6 after the second impact and only one radius presented a fracture after the third impact. Nine radii had no fracture Figure 2-13.

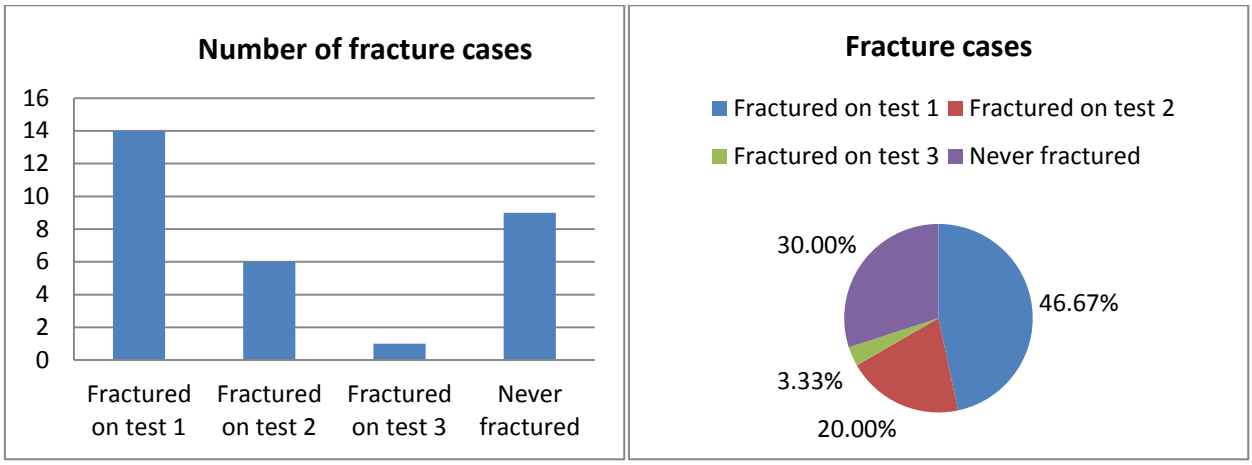

Figure 2-13 : Fracture Cases, expressed in number and percentage.

The type of fracture is also indicated in the Table 2-1. As it can be seen, the prevalent fractures types are Colles' and Barton's (explained before 1.4.5) Main fractures types are shown in the Figure 2-14

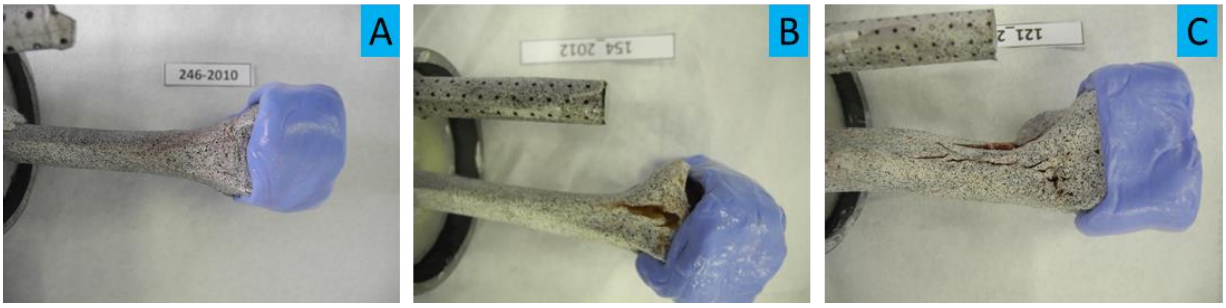

Figure 2-14 : Main type of fracture found in the experiments. A. Colles' fracture (Radial shortening). B. Barton fracture (volar). C. Complex fracture.

The Colles' fractures featured radial shortening. They were stable, and the fracture was barely visible by a simple overview of the bone.

The Barton's fracture corresponds to a dislocation of the volar rim of the radius. In this experiment, the movement of the volar rim causes the opening of the radius into two main parts, along its longitudinal axis.

Confirmation of the type of fracture was made by using the high speed recordings, but also by a radiologist who saw the final results of the impacting. These recordings allowed seeing in detail the fracture pattern and the time of impact.

Two causes of complex fractures where also found. This is the result of various types of fractures, i.e., several fractures propagate simultaneously from different directions. However the displacement pattern appreciated was mainly volar and radial.

2.3.3 Strain analysis

The surface strain was computed from a stereo correlation analysis using the images from the high speed cameras, which allows visualizing and estimating two different 3D strain fields. For the strongest bone (Radius n°250_2010), von Mises strain reached a maximum value of 0.9% on the anterior region and 2% on the ulnar side. For the weakest bone (radius n°013_2010), the maximum measured von Mises strain value before fracture was 1.5% on

the anterior region, and 3.1% on the ulnar side. Surface strains for the anterior region are shown in the Figure 2-15.

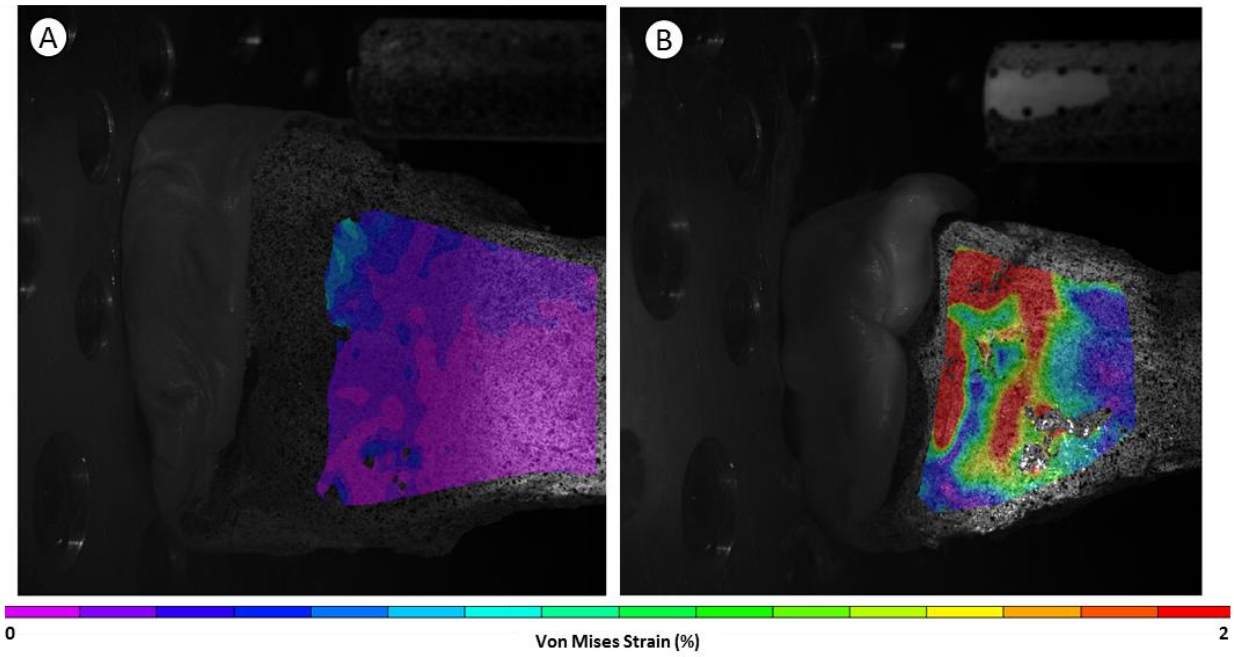

Figure 2-15 : von Mises Strain distribution in the anterior region, for the strongest (A)and weakest bone (B). A) Non-Fractured radius at the maximum load. B) Fractured radius (Colles' type fracture). First frame after fracture (the red part of the strain pattern is equal to or above 2%).

2.4 Discussion

This study provides a protocol to reproduce a forward fall on the radius. Most previous studies evaluated bone strength under static conditions. Moreover previous studies loaded radii until failure in all cases (Pistoia et al. 2002)(Macneil & Boyd 2008)(Varga et al. 2009)(Mueller et al. 2011).

The average value of the experimental peak forces are in agreement with those reported in the literature: 2142 (1229) N (Burkhart et al. 2014).

In the current protocol, a unique loading case was considered for all radii to get fractured and non-fractured groups. This goal was then achieved. Among the 30 radii tested, 14 had a fracture after the first impact. Having these two groups with known loading conditions (orientation and speed) will be of great interest to assess the predictive capability of finite element models. When observing the high speed videos, it was found that, among the 30 radii, 8 presented a sliding effect of the mold over the articular surface. This effect occurred because the articular surface tilted with respect to the surface of the impact plate. This angle is called the Radial inclination Figure 2-16.

Figure 2-16 : An example of a radiography showing the radial angle of inclination.

The observations suggest that during an impact caused by a forward fall, the scaphoid and lunate could slide over the articular surface if this radial inclination is important.

Among those 8 cases that presented sliding of the mold, 7 never presented a fracture, and 1 presented a fracture only at the third impact.

This is not a drawback of the experiment. It is revealing an expected behavior of the joint in the real life. Indeed, during a forward fall over the forearm, the scaphoid and lunate move partially in the plane perpendicular to the longitudinal axis of the radius (Belloti et al. 2013). Thus, the loading can change compared to the initial loading conditions. As a consequence, bone with a titled articular surface may not fracture, not because its strength is high but because the loading was lowered due to the joint shape.

Regarding the strain analysis, highest strain was found at the ulnar side, as presented in literature before (Burkhart et al. 2014). Further analysis will provide a more detailed description of the localization and the value of these strains over time.

2.5 Conclusions

Thirty radii were tested under a dynamic non-axial loading to reproduce the most common forward fall configuration. Most previous studies have evaluated the bone strength under static conditions. Moreover previous studies loaded radii until failure in all cases. In the current protocol, a unique loading case was considered to get fractured and non-fractured groups. Having these two groups with known loading conditions (orientation and speed) will be of great interest to assess the predictive capability of finite element models.

Chapter 3. Numerical study: effect of the loading direction

3.1 Introduction

As presented in the subchapter 1.4.3, the HR-pQCT (Scanco Medical) has a finite element analysis module (iplfe, μFEM) that allows the evaluation of numerical bone strength. The evaluation is realized on distal bones: radius or tibia. Several studies (Boutroy et al. 2008; Macneil & Boyd 2008; Liu et al. 2010) have shown that this FEA algorithm routine correctly estimates the bone strength. This routine uses an axial configuration for the load. As discussed before (subchapter 1.4.3). If we take the case of the falls from the standing height, only 15 percent of the case involve an axial loading of the radius (Melton et al. 2010). Furthermore, despite the good level of prediction of the bone strength by the μFEM, it has not been possible to confirm that μFEM estimates the risk of fracture better than the bone mineral density measurements by DXA (Rietbergen & Ito 2015). We assume that using a non-axial loading could improve the prediction capabilities of the model. In order to test this hypothesis, we used the results obtained from Chapter 2. We created a μFEM of a 9 mm segment (called "segment model") of the bones tested experimentally, and we used the classification obtained, (i.e. fractured and non-fractured groups), to estimate the prediction capabilities using the axial and non-axial loading.

Firstly, we clinically analyzed the bones, created a new FE model and compared the behavior of the segment model under the standard axial loading and under an arbitrary non-axial loading configuration. Secondly, we evaluate five more non-axial loadings related to different fall cases. Finally, we compared the estimations of bone strength with the value measured experimentally, and also with the capability to estimate the risk of fracture.

The aim of this chapter is then to evaluate the prediction capability of the radius segment FEM using different orientations of loading in a static configuration.

3.2 Methods and results

The samples tested here correspond to the 30 bones tested ex-vivo (described in the Chapter 2) and two more samples, that were not tested experimentally because they were not longer enough to be included in the protocol. The bones were measured using Dual X-

Ray Absorptiometry (DXA) (HOLOGIC, USA), in order to follow the standard diagnosis evaluation for osteoporosis. Using the DXA, ultra-distal third part of the radius was analyzed and measurement of areal bone mineral density (aBMD, g/cm^2) and T-score were retrieved. The region of analysis is shown in the Figure 3-1.direction

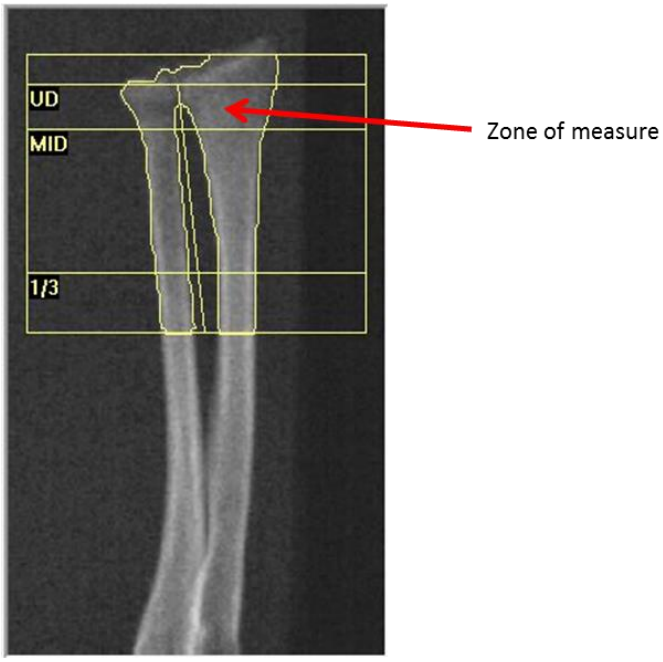

Figure 3-1 : Indication of the zone of measurement selected for this study in the DXA Software. UD: Ultra-distal, MID: Medial 1/3: distal third.

These measurements allow the classification of the radius as osteoporotic, osteopenia, or normal. Results are shown in Table 3-1.

Sample	Age	Sex	Bone Mineral Density (BMD)	T SCORE UD	Evaluation
250-2010	80	F	0.52	2.02	Normal
233-2009	79	F	0.50	1.44	Normal
211-2010	80	M	0.50	-0.16	Normal
213-2009	76	F	0.41	-0.43	Normal
166-2012	56	F	0.41	-0.44	Normal
154-2012	50	F	0.41	-0.50	Normal
244-2010	83	M	0.48	-0.55	Normal
206-2010	67	M	0.44	-1.10	Osteopenia
067-2010	75	M	0.44	-1.12	Osteopenia
230-2009	88	M	0.44	-1.13	Osteopenia
234-2010	95	F	0.38	-1.14	Osteopenia

215-2009	79	M	0.44	-1.16	Osteopenia
090-2012	89	M	0.44	-1.20	Osteopenia
245-2010	78	M	0.42	-1.41	Osteopenia
138-2011	77	M	0.42	-1.45	Osteopenia
161-2012	76	M	0.41	-1.68	Osteopenia
056-2010	74	M	0.40	-1.71	Osteopenia
225-2009	94	M	0.40	-1.84	Osteopenia
240-2010	68	F	0.33	-2.25	Osteopenia
024-2011	65	M	0.34	-2.69	Osteoporotic
121-2010	66	M	0.32	-2.98	Osteoporotic
204-2012	57	F	0.30	-2.99	Osteoporotic
229-2009	85	F	0.30	-3.00	Osteoporotic
232-2009	86	F	0.30	-3.01	Osteoporotic
203-2012	91	F	0.29	-3.24	Osteoporotic
243-2010	87	F	0.28	-3.32	Osteoporotic
224-2009	98	F	0.28	-3.36	Osteoporotic
057-2010	96	F	0.25	-3.94	Osteoporotic
246-2010	73	F	0.22	-4.61	Osteoporotic
214-2009	88	F	0.21	-4.88	Osteoporotic
013-2010	74	F	0.19	-5.45	Osteoporotic
239-2010	95	F	0.16	-6.14	Osteoporotic

Table 3-1 : Results of the DXA measurement over the segment of ultra-distal radius.

Over the 32 radii, 13 were classified by the DXA as osteoporotic, 12 as osteopenia and 7 as normal bones.

The samples collection was then scanned using the HR-pQCT (XtremeCT, Scanco Medical, Switzerland), with a resolution of 82µm isotropic voxel size. Using the Scanco software, an automatic segmentation of the clinical Volume of Interest (VOI) of the radius was performed. This VOI corresponds to a 9.02mm length reconstruction in the axial direction. The clinical VOI of the HR-pQCT can be seen in the Figure 3-2. This segmentation uses a 3D Laplace Hamming filter and fixes a global threshold. Hamming cut-off frequency was 0.4 of the Nyquist frequency, weighting factor equal to 0.5 and threshold was set to 400/1000 of the maximal grayscale value (Christen et al. 2014) (Laib & Rüegsegger 1999)

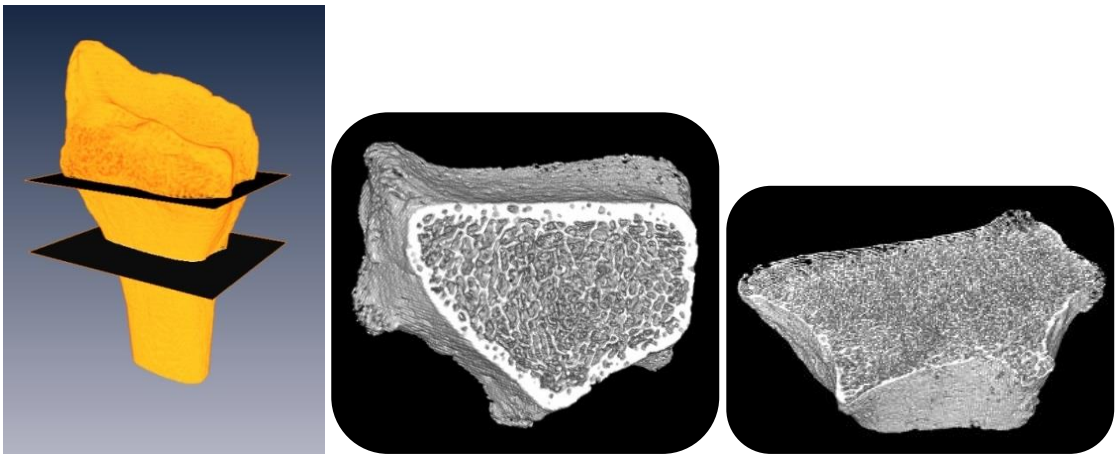

Figure 3-2 : Clinical Volume of interest in the HR-pQCT and segmentation, 9.02 mm length in height (between the two black planes on the left figure)

Finite element models were generated using the iplfe module, from the Scanco Software. Models were obtained by converting each segmented bone voxel to an 8-nodes linear hexahedral element with reduced integration element. The models had a total number of elements varying from 1 to 5 million elements. Bone mechanical properties have been assumed isotropic, homogenous and to follow a linear elastic constitutive law (Young's modulus: 10 GPa, Poisson's ratio: 0.3). An example of the model can be seen in Figure 3-3

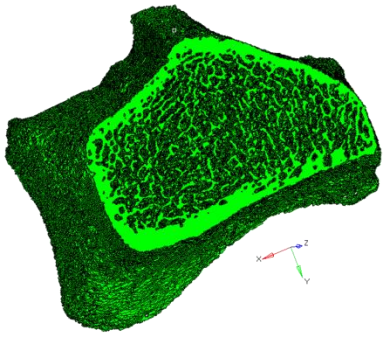

Figure 3-3 : Example of one radius segment mesh generated by the iplfe module (Scanco Medical).

The HR-pQCT software has a set of different loading conditions that can be run. However, we decided to export the segmented model as an input file (*.INP), to be tested using SIMULIA Abaqus (Dassault Systèmes, France). This allowed us to apply our own set of non-axial conditions, but on top of this, using this software we can have access to specific variables that could be used for failure criterion (e.g. the Strain Energy Density).

Before using the model on Abaqus, we made some preprocessing tasks using Hypermesh (Altair, Hyperworks). First, every isolated element or groups of elements, not belonging to the bigger connected group of elements, were deleted. Second, the radius segment was rotated around the longitudinal axis. The purpose of this was to match the anterior face of the radius in the same position for all the radii. The anterior face of the radius was selected as a geometric reference to place all the samples in the same position. The original mispositioning of the samples is caused by the position of the radius during the acquisition, which were not exactly aligned along the main axis.

Images of the segmented radius, before the rotation process, are shown in the Figure 3-4.

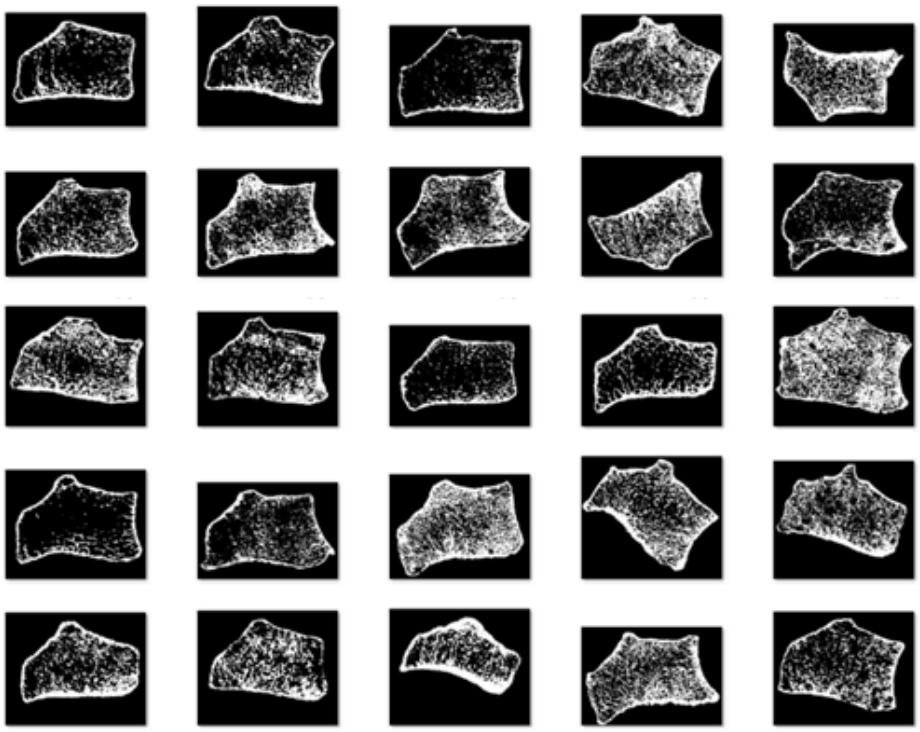

Figure 3-4 : Cross-section images of 30 segmented radius.

Examples of the rotation applied on the radius can be seen at the Figure 3-5.

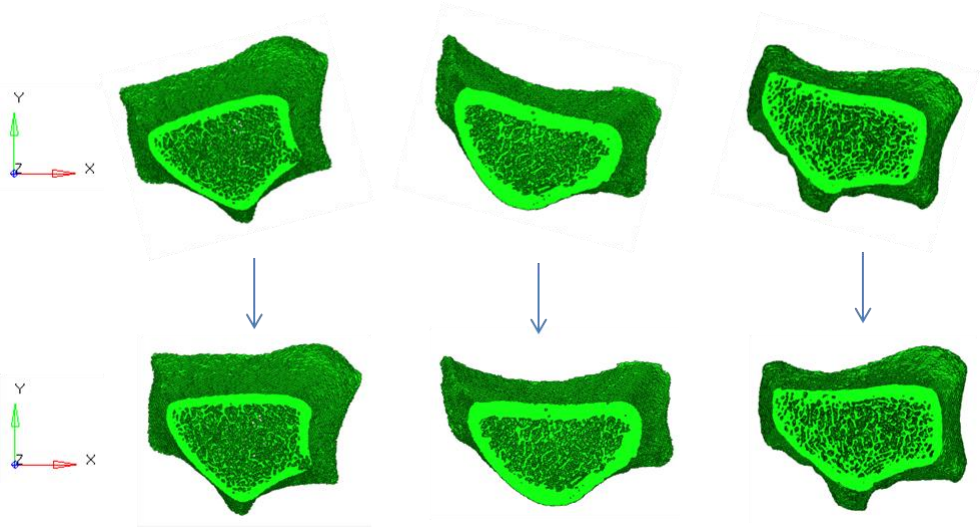

Figure 3-5 : Example of the rotation of the radius segment. The anterior face of the radius was selected as a geometric reference to place all the samples in the same position.

After this operation, the model was finally exported into Abaqus, where different loading conditions were imposed.

3.2.1 Validation Study

The first step was to validate that the micro finite element model (μFEM) implemented on Abaqus (Simulia - Dassault Systèmes) gave similar results compared to the one obtained from the iplfe software (Scanco Medical), when performing the standard estimation of Failure Load (Boutroy et al. 2008). This validation was done on 12 radii (six osteoporotic samples and six normal samples from female subjects). The radius segment was constrained at the proximal cross-section and a compressive displacement (Z axis) of 1% of total length of the segment was applied to the nodes of the distal cross-section. The simulations of the models implemented on ABAQUS were run on a SGI ALTIX ICE computer at the "Centre Informatique National de l'Enseignement Supérieur" (CINES, Montpellier, France). Each simulation used 65 CPUs and took between 10.5 and 12.5 min. In the tests using Abaqus and in the validation simulation performed using the Scanco Software, the failure load was assessed based on Pistoia's criterion (Pistoia et al. 2002). As mentioned before, this criterion suggests that failure occurs when 2% of bone material is charged beyond 7000 micro-strains of effective strain. This effective strain is defined by the Equation 3-1

$$\epsilon_{eff} = \sqrt{\frac{2U}{E}}$$

where:

ϵ_{eff} : Effective Strain

U : strain-energy density

E : Young's modulus

Equation 3-1 : Effective Strain definition. Consistent units to be used for U and E.

Using the Equation 3-1 it is possible to deduce the value of the strain-energy density U needed to achieve a deformation of 7000 micro-strain in a mesh element of 10 GPa. This value is 0.250. In Abaqus, this value of U corresponds to the variable called ESEDEN: Elastic Strain Energy Density. The Figure 3-6 shows the result of one of the simulations in Abaqus.

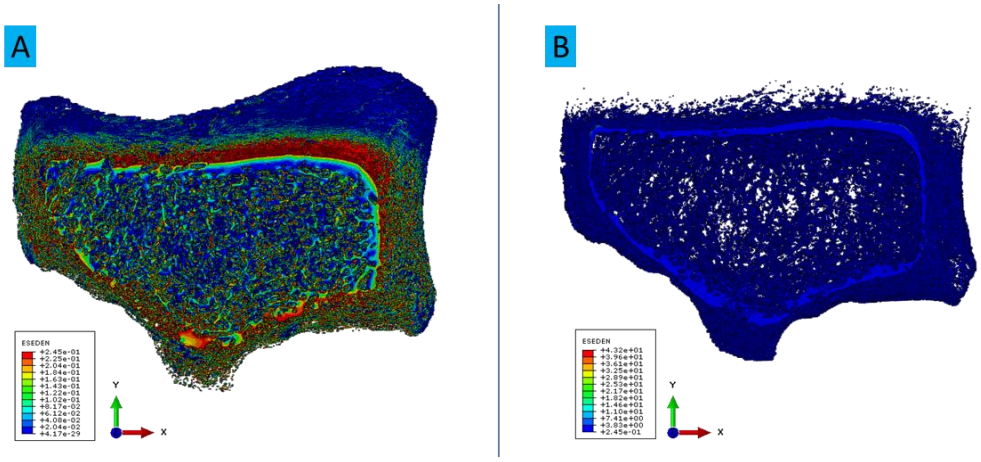

Figure 3-6 : ESEDEN values at the end of the simulation of non-axial loading in a radius bone segment.
A. Elements below the fracture criterion (ESEDEN<0.250).
B. Elements beyond the fracture criterion (ESEDEN>0.250)

A Matlab script was written in order to evaluate the criterion using the results obtained from Abaqus simulation. At the end of the simulation, we obtained the final value of ESEDEN for each of the elements. We used the Equation 3-1 to deduce the value of effective strain. The script collected the value of the effective-strain in a matrix. As assumed by Pistoia, the effective strain was considered increasing linearly. With the time of simulation known (1 millisecond), it is possible to estimate the strain energy density of an element at any time. Thus, the original time of simulation was divided into 10 sub-intervals of times Figure 3-7. We created a matrix of effective strain for each interval. Then, for each matrix,

the script counts how many elements (components) have a value of strain energy beyond the 7000 micro strains limit. Then, between the ten effective-strain matrices, we selected the one in which the quantity of elements beyond the 7000 micro-strains represented the 2% of the total number of elements of each model. As it was expected, the 2% value was not found in this first iteration. Instead, we selected the matrix giving the closest value to 2%, and we created new intervals of times around this value. After three more successive iterations, we assumed the 2% value with a two digits precision. The failure time was then retrieved. Another matrix held the force value at each node of the distal cross-section at the end of the simulation. As it was also assumed that the force value has increased linearly, we could estimate the force at any time. Because we just found the time corresponding to the Pistoia's criterion, we were able to find the related force which corresponds to the computed failure load. A graphical representation of this algorithm is shown in the Figure 3-7.

For the twelve simulations performed directly in the Scanco software, the failure load was a direct output implemented in the standard algorithm analysis. The calculation of the Pistoia's criterion was automatically achieved.

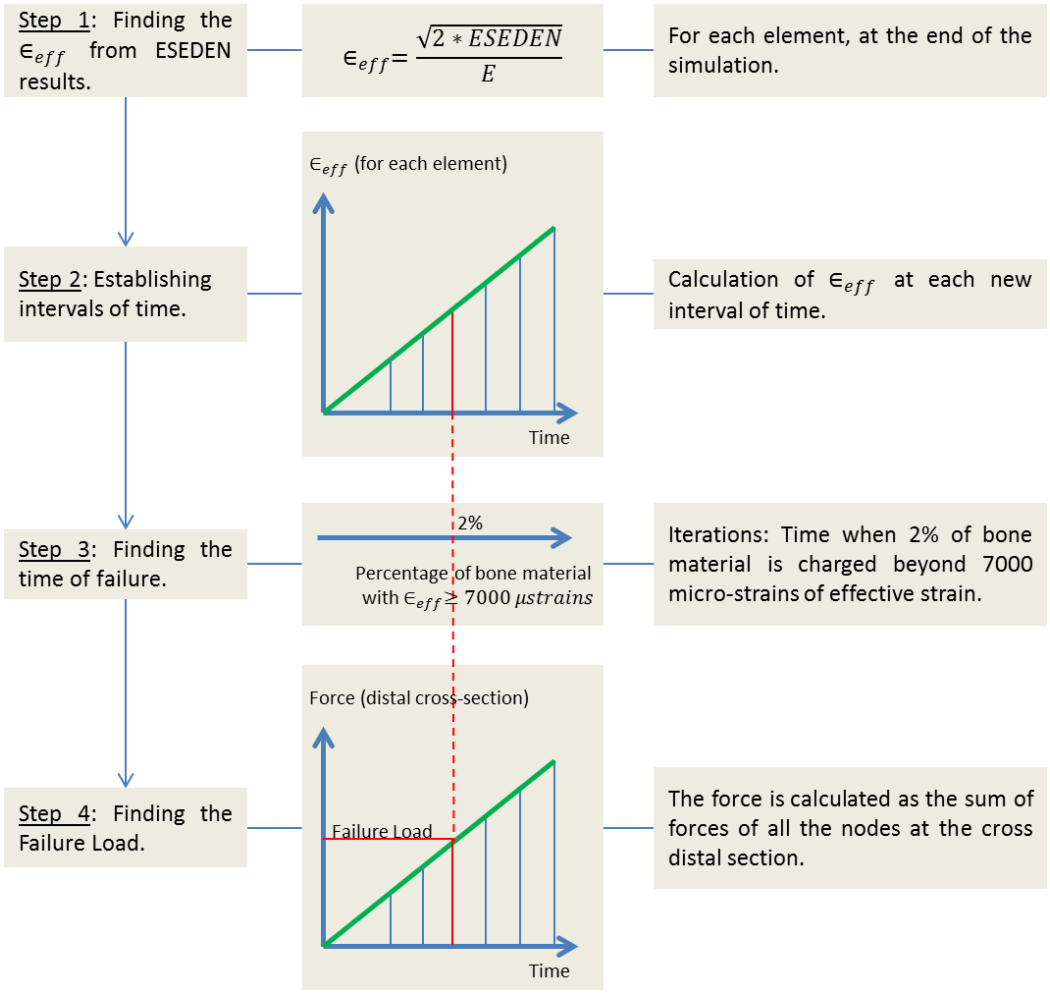

Figure 3-7 : Processing of the simulation results to retrieve the failure load.

The results of the validation test, over 12 radii are shown Table 3-2. The average error was 2.1%.

Axial Failure Load (N) ABAQUS	Axial Failure Load (N) SCANCO
1490	1406
2510	2506
2337	2139
1942	1836
2441	2341
2362	2295
3162	3083
3266	3160

	3944	3919
	5834	6104
	3443	3464
	6211	6507
Average ± SD	3245 ± 1465	3230 ± 1601

Table 3-2 : Comparison between the axial failure load estimated by Abaqus and the one estimated by the Scanco software.

The values of failure load of these 12 radii well also compared with three different studies from literature (Vilayphiou et al. 2010; Varga et al. 2010; Zysset et al. 2013). It was found that all the failure load values are in agreement with these previous studies. This comparison can be seen in Figure 3-8.

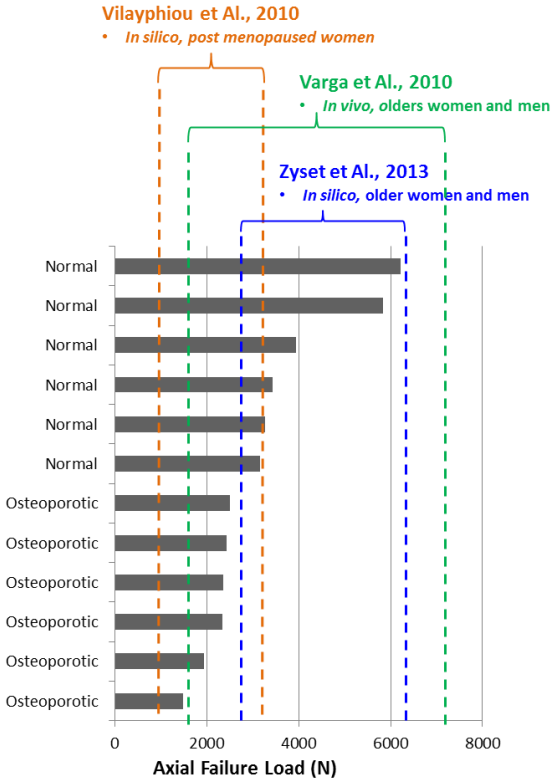

Figure 3-8 : Comparison of the failure load obtained with values from similar studies in literature(Vilayphiou et al. 2010; Varga et al. 2010; Zysset et al. 2013). the grey bars represents the current values.

The axial Failure Load obtained by HR-pQCT iplfe & Abaqus softwares were strongly correlated (n=12, r=0.999, p<0.0001). Moreover, the Bland-Altman plot (Bland et Altman, 1986) showed that the difference obtained between software was within the mean of

difference ±1.96SD. Mean difference in Failure load is 15.15±150 N [-296 N, 198 N], which is inside the limits.

In conclusion, the results showed that the simulations obtained with another simulation code were similar to the reference ones, in axial loading, meaning that the same code could be used to apply different loading conditions (see below).

3.2.2 Effect of the loading direction

3.2.2.1 Comparison: Axial vs non-axial

A non-axial 45° loading (YZ direction) was evaluated by adding another equally displacement component on the Y axis. The total time of simulation was 1 millisecond. A graphical explanation of the loading can be found Figure 3-9.

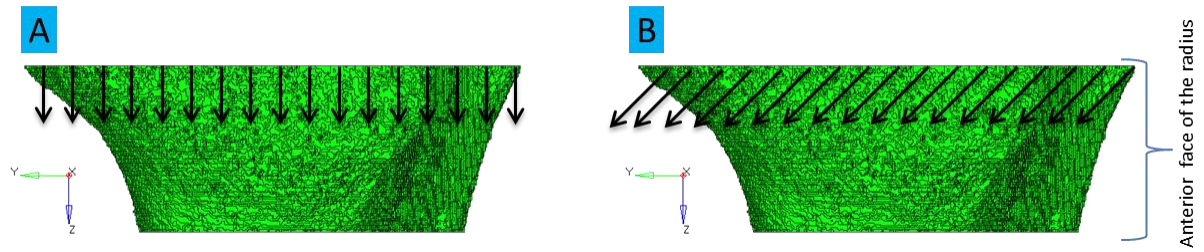

Figure 3-9 : Orientation of the simulated load on the radius segment models. A. Axial B. Non-axial (45°)

The results of axial and non-axial loading of the simulations performed over the distal segment of the radius, using Abaqus, are shown Table 3-3.

Sample	Age	Sex	Failure Load (N) - Axial	Failure Load (N) - non-axial (45°)	Percentage of difference between axial and non-axial load (%)
154-2012	50	F	3162	2430	23.1
166-2012	56	F	3266	2527	22.6
213-2009	76	F	3944	3016	23.5
244-2010	83	M	4641	3674	20.8
211-2010	80	M	5303	4530	14.6
233-2009	79	F	5834	4948	15.2
250-2010	80	F	6211	5145	17.2
240-2010	68	F	2764	2172	21.4
056-2010	74	M	3320	2701	18.6
234-2010	95	F	3443	2738	20.5
138-2011	77	M	4036	3102	23.1

225-2009	94	M	4071	3441	15.5
161-2012	76	M	4157	3508	15.6
090-2012	89	M	4456	3695	17.1
230-2009	88	M	4560	3629	20.4
206-2010	67	M	4570	3520	23.0
245-2010	78	M	4695	4056	13.6
067-2010	75	M	5055	4048	19.9
215-2009	79	M	5241	4486	14.4
239-2010	95	F	1390	1130	18.7
013-2010	74	F	1490	1172	21.3
214-2009	88	F	1942	1502	22.7
246-2010	73	F	2131	1657	22.3
243-2010	87	F	2250	1924	14.5
224-2009	98	F	2326	1904	18.1
204-2012	57	F	2337	1699	27.3
232-2009	86	F	2362	1883	20.3
229-2009	85	F	2441	1945	20.3
203-2012	91	F	2447	2003	18.1
121-2010	66	M	2462	2010	18.4
057-2010	96	F	2510	2004	20.2
024-2011	65	M	2750	2088	24.1
Average ± SD			3486 ± 1303	2821 ± 1117	19.6 ± 3.3

Table 3-3 : Results of the simulations using Abaqus : axial and non-axial (45°) loading in a distal radius segment.

For the 32 samples, average values of axial and non-axial loadings showed statistically significant difference (Friedman test, $p<0.0001$). We also performed a Wilcoxon paired test to compare between the axial and non-axial groups for each classification (Normal, Osteopenia and Osteoporotic). This test also found statistically significant differences (Table 3-4) In order to compare the axial and non-axial loading, the differences between these two loading directions were plotted along axial failure load. The result can be found Figure 3-10.

	n	Failure Load (N) Axial ± SD (N)	Failure Load (N) Non-axial (-45°) ± SD (N)	WILCOXON paired test
Normal	7	4623 ± 1217	3753 ± 1138	p=0.018
Osteopenia	12	4197 ± 729	3425 ± 655	p=0.002
Osteoporotic	13	2218 ± 395	1763 ± 317	p=0.001
TOTAL	32	3486 ± 1303	2821 ± 1117	p<0.001

Table 3-4 : Average failure load for the distal radius segment: Comparison between Normal, Osteopenia and Osteoporotic bone, under axial load and non-axial load (45°).

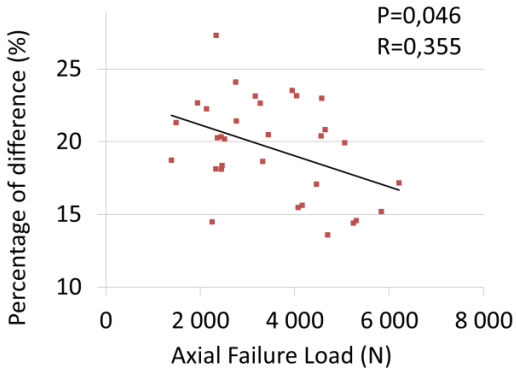

Figure 3-10 : Loading orientation effect on failure strength for 32 radii (7 Normal, 12 Osteopenia and 13 Osteoporotic), difference between axial and non-axial compression (Percentage) vs axial Failure Load (N).

As it can be seen, differences between the two loading directions and axial failure load showed a negative trend. The weaker the bone in the axial direction the greater the difference between the two loading directions.

Our results suggest that the bones having the lower strength may be more sensitive to the direction of loading. This is an argument in favor of our assumption stating that non-axial loading might be discriminant to assess bone fracture.

3.2.2.2 Comparison of several non-axial fall related loadings

The subchapter 3.2.2.1 has shown that the bone segment performed a different behavior depending of the loading direction. This behavior was expected, because of the structure, and because of the intrinsic anisotropy of the structure, which is related to the disposition of the bone network. The angle of 45° selected in the previous subchapter was an arbitrary value to check whether there were notorious differences between the axial and the non-

axial loading. It was shown that indeed there was a statistically significant difference between these two types of loading (mean difference of 20%). As it has been discussed in the Chapter 1, the most common fracture in the radius occurs during a forward fall of 75° between the anterior face of the radius and the ground. Therefore, it is important to estimate this non-axial loading (75°). We also considered additional orientations to see whether there is any specific direction presenting better discrimination capabilities.

Thus, for this study, we evaluated different angles that could occur during a fall. We studied: the axial loading (90°), angle 75° (common fall), and other three angles (60°, 45° and 30°). In the forward fall case with angle 90° the entire load is transmitted along the bone axis, instead, for the forward fall case with an angle of 30° the load is barely found along the bone axis. Figure 3-11 illustrates the position of the bone under these angles.

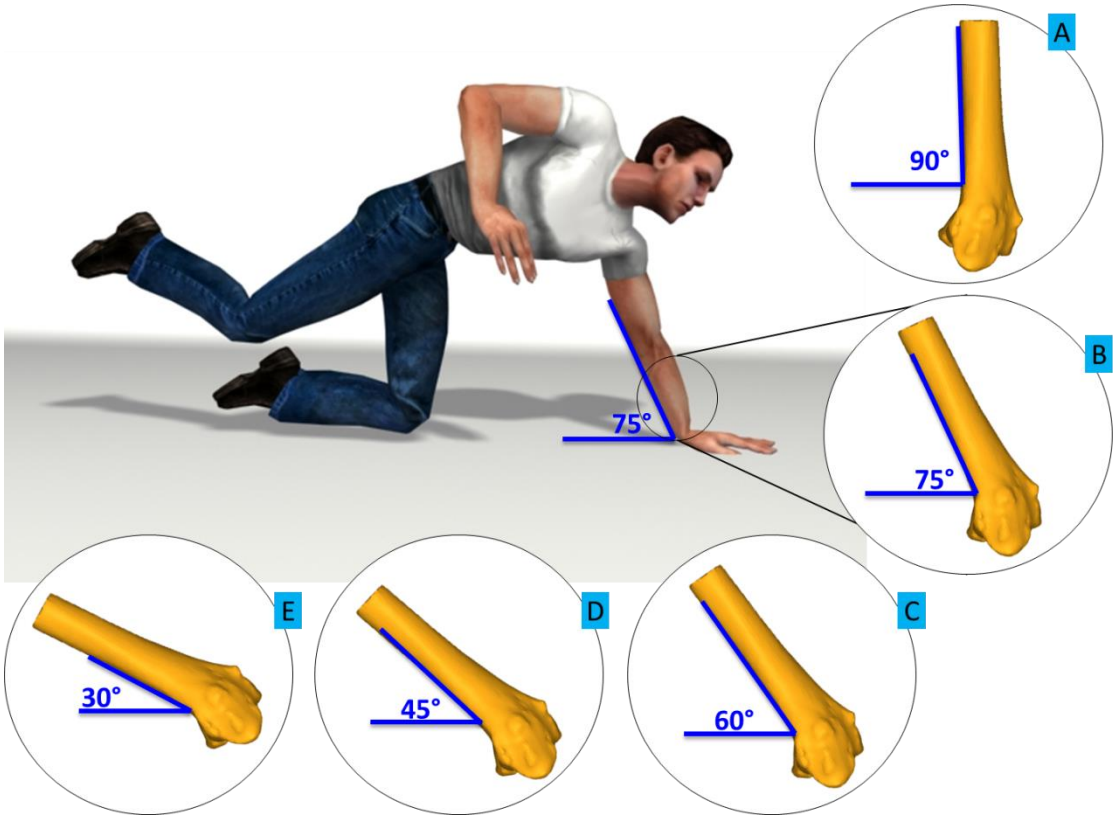

Figure 3-11 : Representation of some possible angles during a forward fall. A. Axial B. 75° C. 60° D. 45° E. 30°.

The distal bone radius segment previously simulated was used for this assay. In order to load this segment in the correct direction of a specific forward fall case, it was important to

position the segment according to the loading direction. The segment was positioned according to the entire radius, to represent a forward fall Figure 3-12.

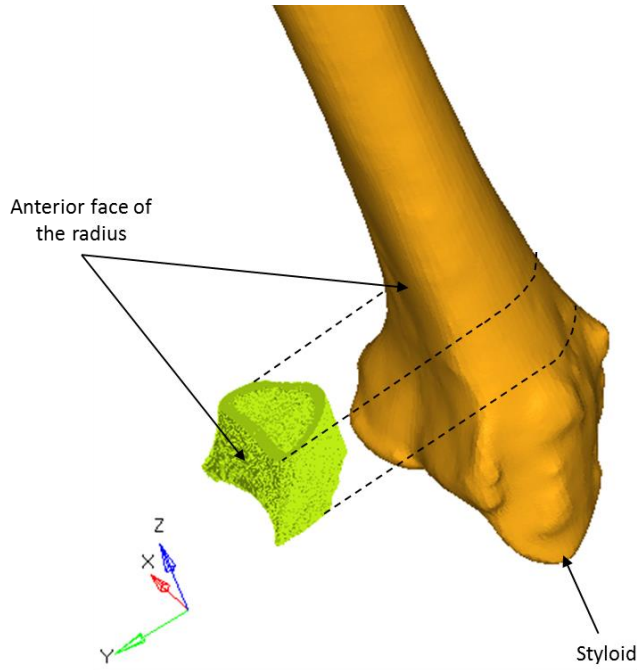

Figure 3-12 : Positioning of the distal radius segment to simulate a forward fall configuration.

From this position, it is necessary to deduce the loading components for each case of fall. The details about these loadings are shown Figure 3-13. In our study we assumed that the loading is transmitted axially from the ground to the bone. This force (in red Figure 3-13) has two main components in the coordinate system of the model: one negative component on Y and one positive component on Z. The methodology to simulate the loading of the distal radius segment is the same as the one presented in the sub-chapter 3.2.2.1, with the only difference stating in the value of the Y axis component of the loading. This Y component value (Figure 3-13) was deduced to assure the direction for each type of non-axial loading (75°, 60°, 45° and 30°). It can then be deduced that the Y component will be given by $y = \frac{0.0902}{\tan(\theta)}$

The results of these simulations were retrieved using a Scilab script.

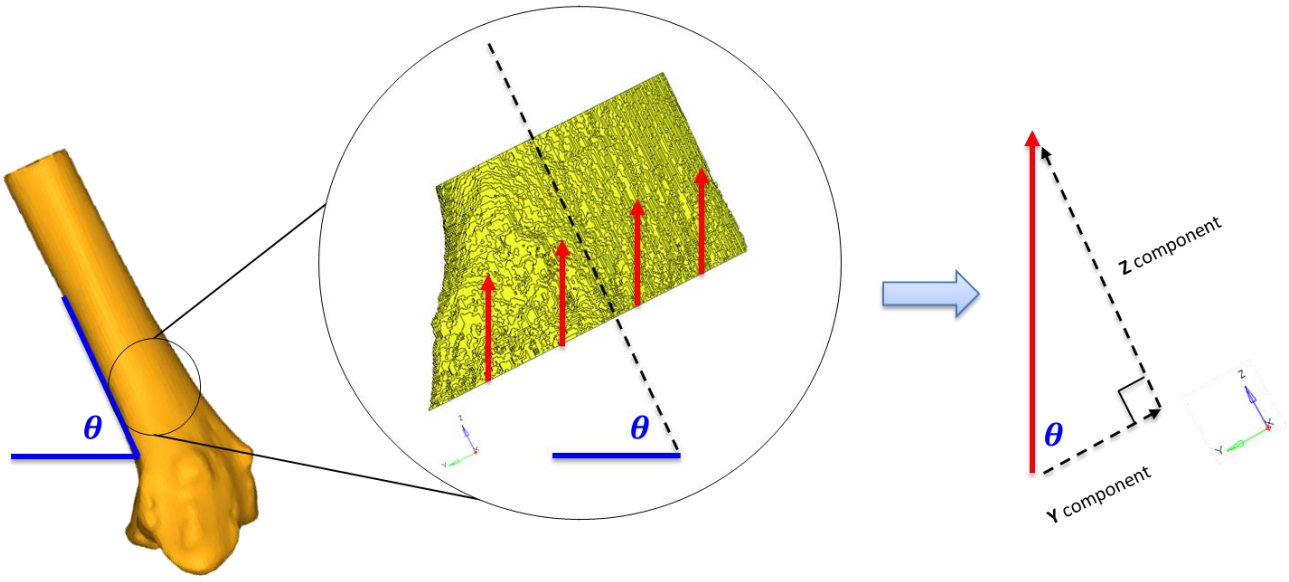

Figure 3-13 : Deduction of the loading components for the distal radius segment.

For the fractured cases from the ex-vivo experiment Chapter 2, the force retrieved (maximum load) corresponds to the failure load. It is then possible to compare these failure loads with the failure load predicted from the finite element models using the Pistoia's criterion.

3.2.3 Discrimination of the groups

In this subchapter we evaluated the discrimination capability of the models between fractured and non-fractured groups. We estimated the average values for the fractured and non-fractured groups, and we verified statistically significant differences by using the P-value (T-test). This analysis also included the ultra-distal measures of BMD and area by DXA, in order to compare with the standard method used in clinics. The results are shown Table 3-5.

	Average		
	fractured	**non-fractured**	**P - value**
DXA Area (Ultra distal) (cm^2)	3.79	4.12	0.052
DXA BMD (UD) (g/cm^2)	0.30	0.42	0.001
YZ Failure Load (N)	2140	3381	0.001

30° Failure Load (N)	2481	3789	0.001
45° Failure Load (N)	2660	4111	0.001
60° Failure Load (N)	2747	4245	0.001
75° Failure Load (N)	2743	4254	0.001
Axial Failure Load (N)	2675	4166	0.001

Table 3-5 : Average and P-value for the no-axial model 'YZ', the fall related non-axial and axial models, and the Area and BMD ultra-distal measured by DXA. (n=30).

It was found that all the segment FEM were able to assess the difference between fractured and non-fractured, except the measurement of the ultra-distal Area by DXA.

3.2.4 Accuracy of the models

It was found that the non-axial fall related models simulations have a higher accuracy than the axial model to assess the experimental failure (forward fall configuration). This accuracy is higher for the lower angle. Nevertheless, the improvement is limited. The SEE is improved by 5.5% using the 30° segment model compared to the axial segment model. (Table 3.5)

Numerical Model	Axial (=90°)	75°	60°	45°	30°	'YZ'
SEE (N)	532	521	512	508	503	559

Table 3-6 : Standard Error of Estimation (SEE) for the prediction of the experimental failure load by the segment FEM (axial and non-axial loadings).(n=14).

3.2.5 Correlations between model and experiment

It was found a good correlation between the experimental failure load and the estimations obtained with the fall related segment models (Figure 3-14). The magnitude of the experimental load was correctly estimated in all cases. The correlation coefficient of the fall related to non-axial models was slightly higher than the axial model. The 'YZ' model presented a good correlation with the experimental results, but it was lower than the correlated by the fall related models.

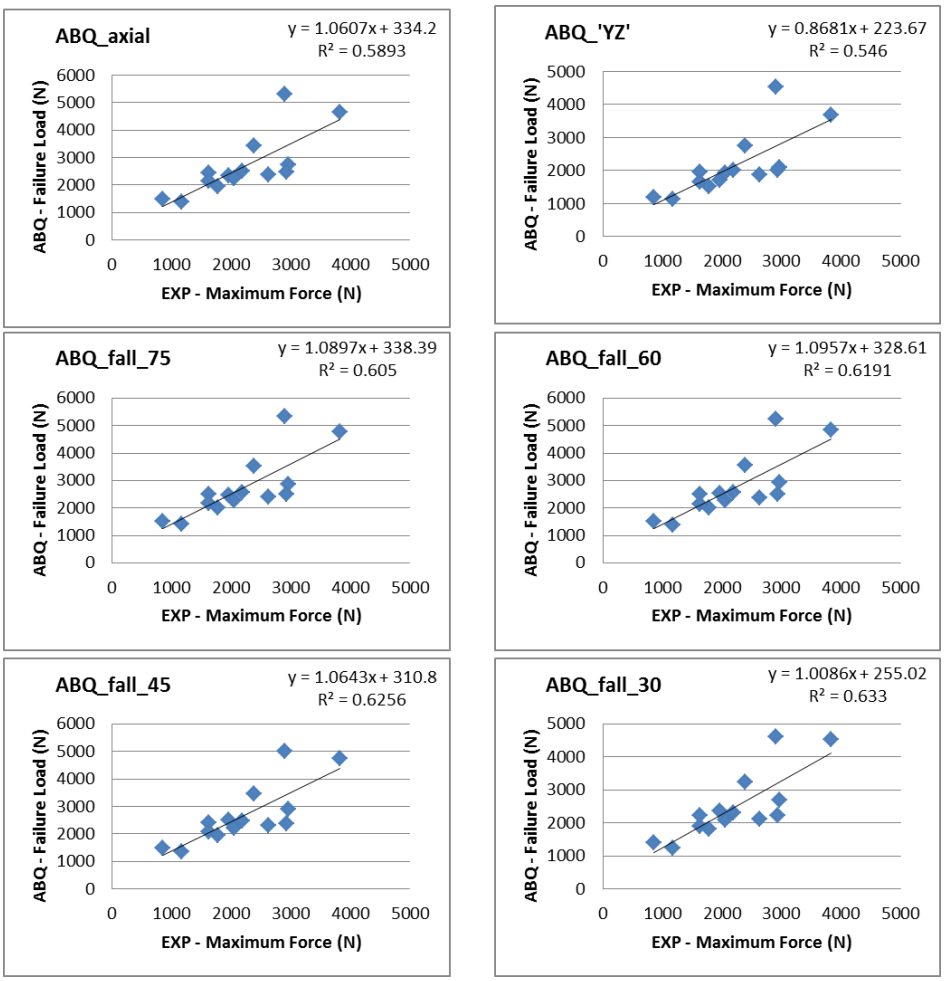

Figure 3-14 : Correlations between experimental failure load (n=14) and the failure load estimated using the Pistoia's criterion on the micro finite element models. Here we present the results for the 5 tested directions related with the fall.

3.2.6 Assessment of the risk of fracture

It is possible to evaluate the prediction capabilities of the FEM by estimating the φ ratio (Chapter 1, Equation 1-4) which is estimated as the ratio between external load (usually from literature) and the numerical bone strength. If this ratio is greater than one, a fracture should occur. It this present study, the external load is given by the maximal load recorded during the experiment and the failure load can be estimated by the different models. The results are summarized Table 3-7.

Sample	AGE	SEX	Experimental Maxium Force (N)	Numerical Failure Load - Axial (N)	Numerical Failure Load - 75° (N)	Numerical Failure Load - 60° (N)	Numerical Failure Load - 45° (N)	Numerical Failure Load - 30° (N)	Numerical Failure Load - 'YZ' (N)	Φ axial	Φ 75°	Φ 60°	Φ 45°	Φ 30°	Φ 'YZ'
013-2010	74	F	8.490E+02	1.490E+03	1.524E+03	1.524E+03	1.488E+03	1.406E+03	1.172E+03						
239-2010	95	F	1.176E+03	1.390E+03	1.416E+03	1.404E+03	1.348E+03	1.236E+03	1.130E+03						Yes
246-2010	73	F	1.625E+03	2.131E+03	2.179E+03	2.162E+03	2.073E+03	1.895E+03	1.657E+03						
214-2009	88	F	1.777E+03	1.942E+03	2.011E+03	2.023E+03	1.961E+03	1.819E+03	1.502E+03						Yes
204-2012	57	F	1.965E+03	2.337E+03	2.462E+03	2.537E+03	2.506E+03	2.357E+03	1.699E+03						Yes
243-2010	87	F	2.055E+03	2.250E+03	2.276E+03	2.265E+03	2.207E+03	2.085E+03	1.924E+03						Yes
057-2010	96	F	2.182E+03	2.510E+03	2.564E+03	2.560E+03	2.476E+03	2.303E+03	2.004E+03						Yes
234-2010	95	F	2.381E+03	3.443E+03	3.533E+03	3.549E+03	3.464E+03	3.248E+03	2.738E+03						
232-2009	86	F	2.634E+03	2.362E+03	2.409E+03	2.389E+03	2.295E+03	2.120E+03	1.883E+03	Yes	Yes	Yes	Yes	Yes	Yes
211-2010	80	M	2.903E+03	5.303E+03	5.339E+03	5.254E+03	4.998E+03	4.613E+03	4.530E+03						
121-2010	66	M	2.927E+03	2.462E+03	2.519E+03	2.515E+03	2.380E+03	2.218E+03	2.010E+03	Yes	Yes	Yes	Yes	Yes	Yes
024-2011	65	M	2.971E+03	2.750E+03	2.881E+03	2.945E+03	2.890E+03	2.687E+03	2.088E+03	Yes	Yes	Yes	Yes	Yes	Yes
229-2009	85	F	1.629E+03	2.441E+03	2.504E+03	2.500E+03	2.409E+03	2.231E+03	1.945E+03						
244-2010	83	M	3.825E+03	4.641E+03	4.790E+03	4.830E+03	4.742E+03	4.518E+03	3.674E+03						Yes
161-2012	76	M	2.206E+03	4.157E+03	4.218E+03	4.222E+03	4.154E+03	4.001E+03	3.508E+03						
166-2012	56	F	2.478E+03	3.266E+03	3.407E+03	3.486E+03	3.464E+03	3.298E+03	2.527E+03						
203-2012	91	F	2.697E+03	2.447E+03	2.455E+03	2.397E+03	2.280E+03	2.128E+03	2.003E+03	Yes	Yes	Yes	Yes	Yes	Yes
206-2010	67	M	4.344E+03	4.570E+03	4.702E+03	4.685E+03	4.488E+03	4.125E+03	3.520E+03					Yes	Yes
213-2009	76	F	3.486E+03	3.944E+03	4.116E+03	4.178E+03	4.083E+03	3.782E+03	3.016E+03						Yes
138-2011	77	M	3.674E+03	4.036E+03	4.226E+03	4.323E+03	4.269E+03	3.102E+03	3.102E+03					Yes	Yes
224-2009	98	F	1.692E+03	2.326E+03	2.369E+03	2.362E+03	2.293E+03	2.150E+03	1.904E+03						
225-2009	94	M	2.936E+03	4.071E+03	4.111E+03	4.066E+03	3.918E+03	3.647E+03	3.441E+03						
154-2012	50	F	3.925E+03	3.162E+03	3.273E+03	3.295E+03	3.196E+03	2.988E+03	2.430E+03	Yes	Yes	Yes	Yes	Yes	Yes
250-2010	80	F	3.929E+03	6.211E+03	6.291E+03	6.236E+03	6.020E+03	5.624E+03	5.145E+03						
233-2009	79	F	2.178E+03	5.834E+03	5.857E+03	5.747E+03	5.461E+03	5.035E+03	4.948E+03						
090-2012	89	M	3.990E+03	4.456E+03	4.500E+03	4.443E+03	4.260E+03	3.968E+03	3.695E+03					Yes	Yes
067-2010	75	M	4.178E+03	5.055E+03	5.171E+03	5.162E+03	4.985E+03	4.613E+03	4.048E+03						Yes
056-2010	74	M	4.203E+03	3.320E+03	3.406E+03	3.426E+03	3.361E+03	3.208E+03	2.701E+03	Yes	Yes	Yes	Yes	Yes	Yes
215-2009	79	M	5.818E+03	5.241E+03	5.233E+03	5.082E+03	4.749E+03	4.320E+03	4.486E+03	Yes	Yes	Yes	Yes	Yes	Yes
230-2009	88	M	6.265E+03	4.560E+03	4.727E+03	4.813E+03	4.798E+03	4.630E+03	3.629E+03	Yes	Yes	Yes	Yes	Yes	Yes

Table 3-7 : Prediction by using the φ ratio (External Load/Bone estimated failure load) for the fractured cases (shadowed in blue) and non-fractured cases. "Yes" means Phi>1 and there is a fracture risk.

Over the 14 cases of fracture, the criterion was only true (>1) for 3 cases for the model with fall related non-axial loading and for the axial loading. For the non-axial loading 'YZ' the estimation using this criterion has detected 9 cases over 14. For the non-fractured cases, the axial, 75°, 60°, 45° predicted correctly 11 over 16 cases; the 30° model detects 8 over the 16; cases and the 'YZ' model predicted only 6 over the 16 cases.

3.2.7 Assessment of a criterion

Another way to estimate the detection capability is by using a threshold criterion. This procedure is represented in the Figure 3-15 for the 'YZ', 75° and axial model.

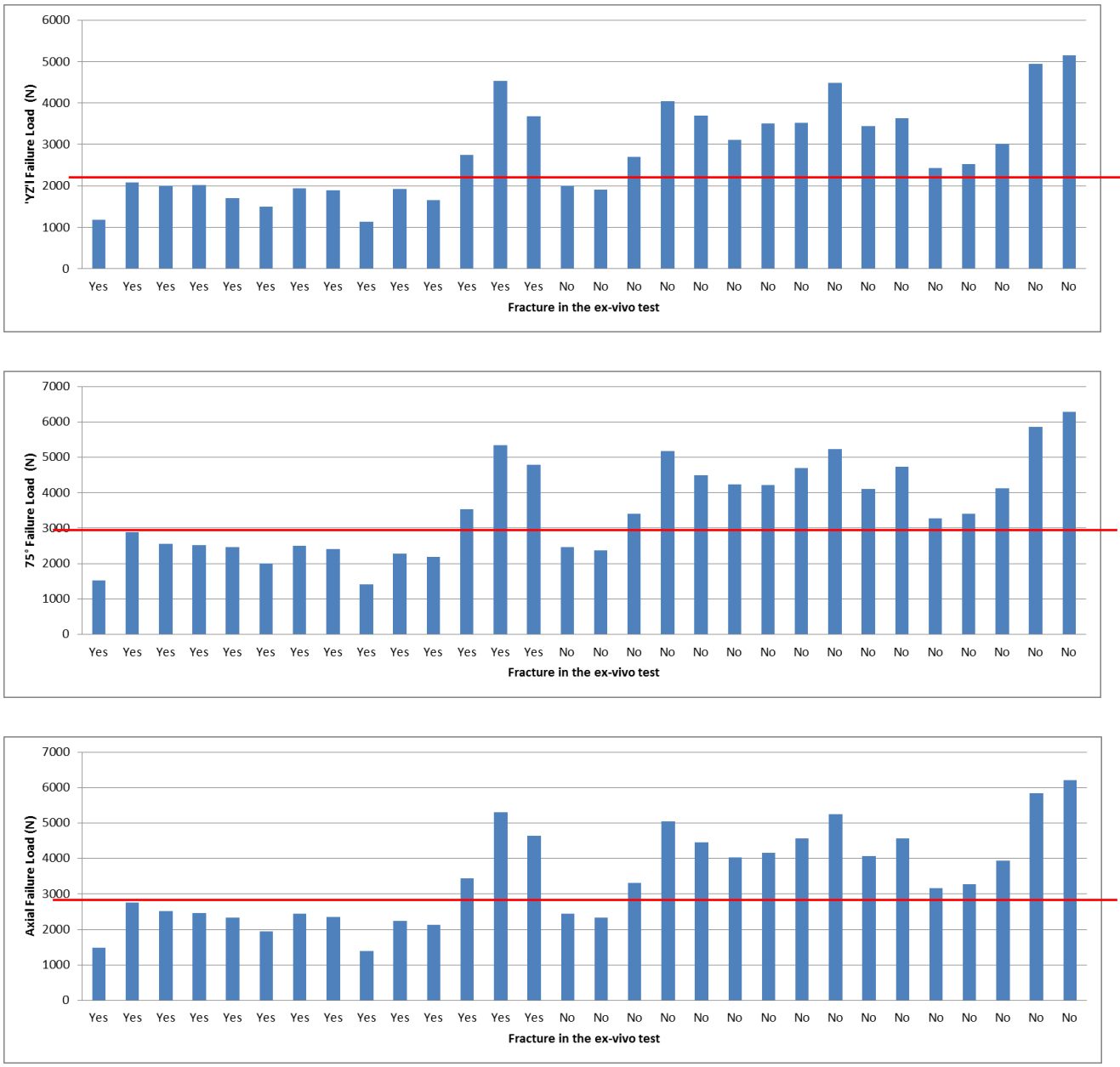

Figure 3-15 : Evaluation of the ratio Failure Load over the fractured and non-fractured cases at the first impact of the ex-vivo experiment Chapter 2. This figure presents the results for 1) Top: the model 'YZ' (-45°), 2) Middle: the fall case model (75°) and 3) Bottom: the axial model (standart HR-pQCT).

Drawing a graph with experimental data and numerical results in "y axis", a threshold could be set to a certain value to allow the distinction between both experimental groups (Figure 3.16).

For the 'YZ' model, the threshold value can be set to ~2200 N. In this case, the threshold detects 11 fractured radii over 14, and 14 non-fractured radii over 16. For all the non-axial

fall related models (75, 60, 30°), the threshold value is higher, with ~3000N. The capability prediction was the same as the 'YZ' model. For the axial model, the threshold value could be ~2900 N, and the capability of prediction remains the same that for the other non-axial models.

Previously, we found a statistically significant difference using the measure of BMD ultra-distal by DXA. Then, we can also evaluate its detection capabilities Figure 3-16.

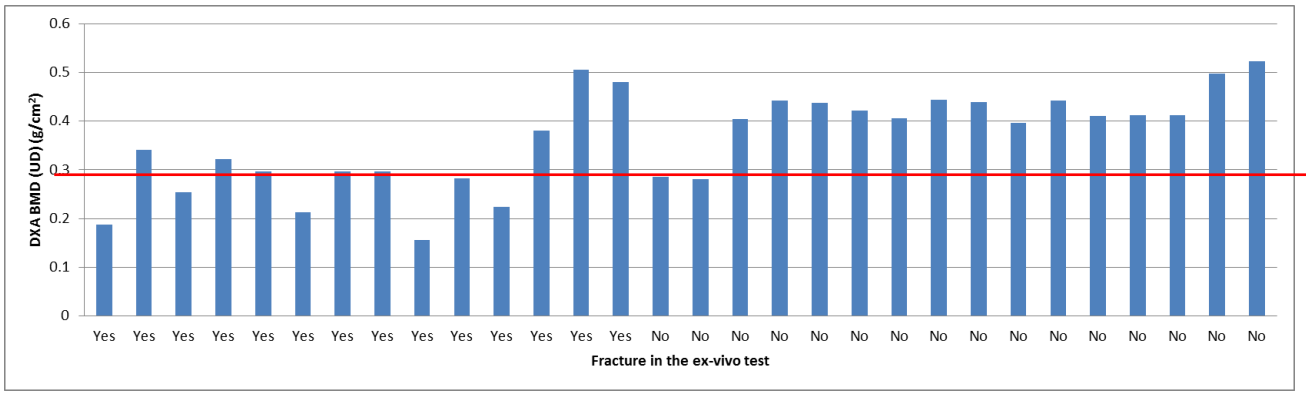

Figure 3-16 : Evaluation of the ratio DXA BMD (Ultra distal) over the fractured and non-fractured cases at the first impact of the ex-vivo experiment Chapter 2.

For this case, setting a threshold value is difficult and an accurate determination would need more advanced techniques (logistic regression curves). However, if we set a threshold value detecting the same non-fractured cases than for the threshold on the failure load of the segment models (14 cases over 16), we found a detection of 6 over 14 of fractured cases.

The detection results are summarized in Table 3-8.

	% of detection	
	fractured	non-fractured
BMD DXA	42.96	87.5
Axial Failure Load	78.6	87.5
75° Failure Load	78.6	87.5
60° Failure Load	78.6	87.5
45° Failure Load	78.6	87.5
30° Failure Load	78.6	87.5
YZ Failure Load	78.6	87.5

ϕ axial	21.4	68.7
ϕ 75°	21.4	68.7
ϕ 60°	21.4	68.7
ϕ 45°	21.4	68.7
ϕ 30°	21.4	50.0
ϕ 'YZ'	64.2	37.50

Table 3-8 : Detection percentage for the segment model and for the DXA.

Using a threshold criterion of Failure Load allowed the detection of the fractured (79%) and the non-fractured (87.5%) cases. Using the ratio φ for the detection of the fractured and non-fractured bones was not effective. Indeed, the group of fall related models had a low detection level of the fracture cases (21.4%). This detection level of the fracture cases is higher on the 'YZ' model (64.2%), but, for this model, the level of prediction of the non-fractured cases was low (37.5%).

3.3 Discussion

The first results suggest that the bones having the lower strength may be more sensitive to the direction of loading. This is an argument in favor of our assumption stating that non-axial loading might be discriminant to assess bone fracture.

Using non-axial loading simulations improve slightly the prediction experimental failure load. The SEE using the non-axial model was improved by 5.5% compared to the axial model.

We obtained statistically significant differences between the fractured and non-fractured groups using the BMD and all the numerical models.

In our simulations, in static configuration, Pistoia's criterion was able to predict the bone strength even in the non-axial directions. Nevertheless, confrontation of the models with the φ factor, to estimate their prediction capabilities, has shown a lower quota of prediction. Only 3 cases were predicted over the 14 fracture cases (21.4%). The 'YZ' model presented a better prediction of the fractured cases (64.3%) but a low prediction of the non-fractured cases (37.5%).

This could mean that the φ ratio as calculated with a "real fall condition in term of angle" is not an adequate way to predict the risk of fracture for the radius segment model compared to experimental data. Based on our experiment, we know the value of this load, but in real life it will remain unknown. However, we can notice that a Phi calculate with an improbable loading angle discriminate more the fractured group. Thus, it is important to consider evaluating the risk of fracture under another loading condition when using the radius segment FEM from HR-pQCT.

3.4 Conclusions

We were able to manipulate a µFEM segmented by the HR-pQCT on Abaqus. This allowed us to assess different loading conditions. The estimation of the experimental failure load was achieved using the standard axial loading. The accuracy of estimation did not improve by changing the direction of the load (only 5.5%). However, all the models allowed the discrimination of the fractured and not fractured groups.

The prediction of the risk of fracture remains low when using the φ ratio. However, by using a threshold value of the failure load it was possible to estimate ~79% of the fracture cases and ~88% of the non-fractured cases.

In summary, the non-axial loadings tested were not able to improve the prediction of the risk of fracture made by the axial loading. The improvement may be only achieved by doing important changes in the finite element model such as adding dynamic loading conditions in the segment or by selecting another loading condition.

Chapter 4. Finite element model reproducing an ex-vivo forward fall on the distal radius.

4.1 Introduction

As it was shown in the previous chapter, we found that segment model is sensitive to the direction of the loading. Nevertheless, when comparing the segment models with the ex-vivo experiments, we found that the accuracy, the discrimination and the detection level were not notoriously improved by the use of non-axial models. Anyhow, the segment model presented different limitations. First, the sample itself consists only in a segment of a few less than one centimeter length. Even if this part could be representative of the measure of the bone quality in different parameters (for example BV/TV, cortical thickness, cortical area, etc) (Macneil & Boyd 2008), this model may lacks of a global understanding about how the failure occurs.

As it was shown in the Chapter 2, in the case of a fall exists a notorious influence of the radial inclination. This angle, which measures the inclination of the articular surface, could play an important role in the bone strength. Higher values of the radial inclination may cause a deviation of the impact load during a fall. Then, the capability prediction of a finite element model taking only a section of the radius could be limited.

In addition, the evaluation of the bone failure risk should include an analysis under realistic loading conditions in term of speed. If we consider the case of the falls, the radius will be in most of the cases affected by dynamic non-axial loadings.

This is why we decided to develop a finite element model of the distal radius simulating the loading conditions (orientation and speed) of the fall, the same forward fall case as the one reproduced experimentally in the Chapter 2.

We made the hypothesis that a finite element model of the distal radius, reproducing the loading conditions of a fall case, could be more predictive than models which evaluate the bone strength under static axial loading.

This chapter presents the development of a heterogeneous model and the estimation of its prediction capabilities for the bone strength. The accuracy of this model is at the end compared with the segment FEM described Chapter 3.

4.2 Methods and results

We created a heterogeneous FEM of the whole distal radius, where the direction and speed conditions of the ex-vivo protocol, described in the Chapter 2, were implemented.

We used the data scans from the Cone Beam Computer Tomography (CBCT), acquired before the experimentation. The field acquired was a cylindrical region (diameter 15 cm and width 12 with) with 150µm of resolution. The DICOM images were exported into the Mimics software (Materialise, Belgium) to create the model. The creation of the model was done into two parts: one part create a binarized model to select the region of interest, and the second part use a mapping of the gray levels to convert in material properties. The two parts are then matched together into one to finally obtain the mesh with associated properties. Those steps are detailed below. We chose a personalized importation in order to keep the original bit map (16 bits) of the images. This avoided the automatic conversion into 12 bit (typical medical data), which, in our case, would imply a loss of accuracy for the subsequent task: segmentation and properties assignment.

First we made the segmentation, which consist in the selection of bone tissue in the images. In our case, this is made by selecting a global threshold value in the gray level histogram Figure 4-1. This selection was made by the examination of the highest and lowest density bones based on DXA measurement. We looked for a value that dodges over selection in the denser bone, but guaranteeing that the bone tissue in the lowest density bone was not underestimated Figure 4-1. Thus, any voxel above the threshold value of 1650 was considered as bone tissue over the 30 samples.

This segmentation was followed by a growth region algorithm. The growing region was selected from the cortical bone. This operation allows having a unique interconnected region mask. This is useful to have later a model composed by a unique interconnected part. It is assumed that the not connected region has a despicable roll in the behavior of the model.

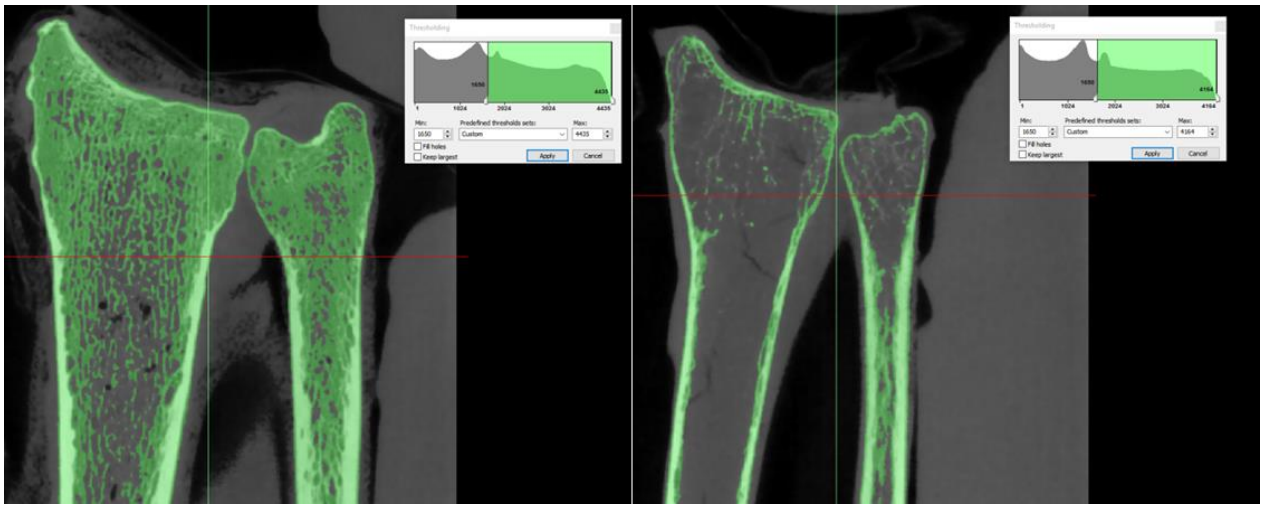

Figure 4-1 : Segmentation of the highest and lowest density bones. This visual inspection allowed establishing a 1650 gray value as the threshold for the set of 30 samples.

After the segmentation, a volume mesh was created. The meshing was generated doing a resize from 3 voxels into one. Then, the final voxel resolution is 450µm. No smooth option was used. The number of elements of the model range between 83 580 and 287 859.

Secondly, the material properties can be assigned by using the gray levels of the images at 150 µm. Indeed, the gray levels were mapped from the image and assigned to the recent created mesh at 450µm. Thus, each element had a corresponding gray level value. However, to know the equivalence between gray values and mechanical properties we need to perform a calibration by using a phantom, as described in subchapter 1.5.2. In this step, we compared the theoretical and experimental value of a material with known density. To do this, we used the values of the phantom used alongside with the bone during the acquisitions.

The phantom used was the QRM-Forearm-Phantom (QRM – Quality Assurance in Radiology and Medicine; Moehrendorf, Deutschland). This phantom has two rods: One rod simulating water, and one with a bone equivalent insert. The physical appearance of the phantom is shown Figure 4-2, and properties Table 4-1.

Figure 4-2 : The QRM-Forearm-Phantom

Base material	tissue-equivalent resin
Phantom cross section	70 x 25 mm^2
Phantom length	150 mm
Phantom weight	225 g
Bone eqv insert specified	200 mg HA/cm^3
Water equivalent insert	0 HU (80 - 140 kV)

Table 4-1 : Specifications of the QRM-Forearm-Phantom

Six bones with different DXA densities, including those with the highest and lowest density were chosen for the calibration measurements. The measurements were made in two locations: the water equivalent rod and the bone equivalent rod, as shown in Figure 4-3 using ImageJ (National Institutes of Health, Unites States). The mean Hounsfield value was obtained.

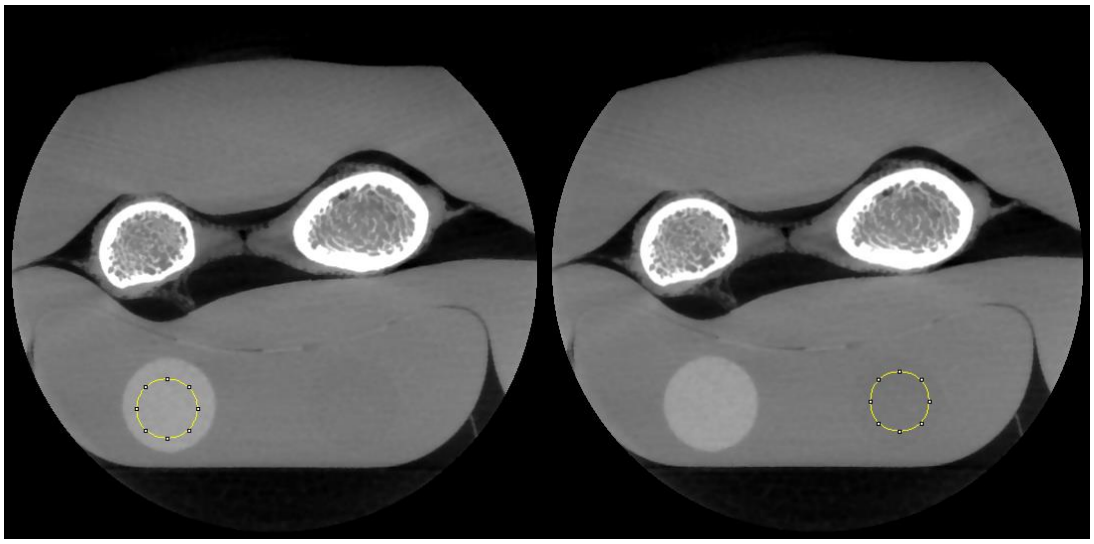

Figure 4-3 : Localization of the measures for the data calibration

Each acquisition stack consisted in 550 images. This measurement was replicated on four slices (100, 200, 300 and 400). The very firsts and very lasts slices of stack were avoided for the calibration measurements because a considerable variation of the grey level was found for some of the samples. This variation is one limitation of the scanner, but only affects a few slices at the edge of the acquisition volume.

The circular area used in the calibration measurement had a value of 72.81 mm^2.

The results of grey levels for all the measurements are shown in Table 4-2.

	250_2010	154_2012	215_2009	024_2011	243_2010	239_2010
Bone Equivalent (HU)	868.422	669.793	800.402	873.509	841.008	824.003
	865.098	665.507	779.925	873.515	829.545	798.852
	862.664	662.086	791.358	875.669	852.257	794.216
	870.741	676.823	789.559	882.176	872.824	789.988
Total Average 808.747 ± 72.369						
Water Equivalent (HU)	401.455	111.588	295.931	332.217	365.576	294.386
	385.612	113.057	274.106	336.837	347.935	287.775
	378.681	136.318	276.672	340.794	328.931	280.418
	389.389	133.366	290.807	343.230	325.324	279.926
Total Average 293.763 ± 86.528						

Table 4-2 : Hounsfield Units (HU) value at the water and bone equivalent rods

An equal sized area was also used on each image to verify that the value of the air was always -1000 Hounsfield units.

Now, using the average Hounsfield value measured at the equivalent inserts of bone and water of the phantom, we calibrated the Hydroxyapatite density value (mg HA/cm^3) with the theoretical value (from the phantom). The relationship is shown in Table 4-3.

	Gray level (HU + 1000)	Theoretical density (mg HA/cm3)
Equivalent Bone	1809	200
Equivalent water	1294	0

Table 4-3 : Relationship between the measured gray value at the CBCT Images and the theoretical value of density.

This relationship allows establishing the calibration curve, which is presented on Figure 4-4.

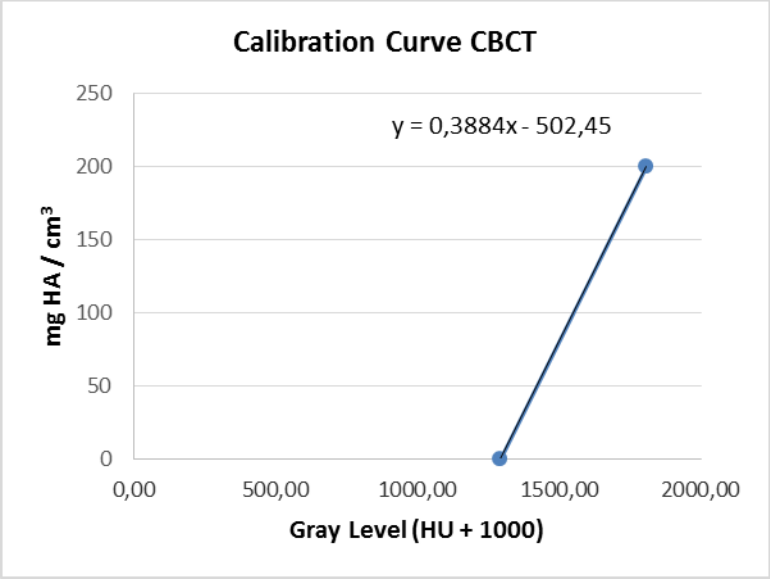

Figure 4-4 : Calibration curve for the CBCT using the QRM-forearm-phantom.

We can relate the apparent density and the Young's modulus using relationship from literature. We decided to use the relationships given par (Morgan et al. 2003) and (Duchemin et al. 2008) to create two different sets of models. These relationships are remembered Equation 4-1.

(Duchemin et al. 2008)	$E = 10.095\text{x}10^3\rho_{HA}$	E: MPa – Young's Modulus
(Morgan et al. 2003)	$E = 6850{\rho_{HA}}^{1.49}$	ρ_{HA}: g/cm^3 – Hydroxyapatite density

Equation 4-1 : Relationships used to estimate Young's modulus from the hydroxyapatite density.
(Morgan et al. 2003) measured for cortical and cancellous bone.
(Duchemin et al. 2008): measured for cortical bone.

Using these equations and the relationship from density to Young's modulus we can map the mechanical properties of each element of the mesh. To avoid defining a huge number of different materials, ten different groups (material cards) of materials were map for each bone.

When deducing the values of Young's modulus, it is possible that negative values appear (because the calibration curve used corresponds to an average curve of all the samples). For these cases, the Young's modulus value is corrected to 0.02 GPa, which is the Young's modulus of the marrow according to Burkhart et al. (Burkhart et al. 2014). Finally, The Young's modulus for the models using the relationship from (Morgan et al. 2003) varied between 0.02GPa and 15.27GPa, and between 0.02GPa and 10.82GPa for the model using relationship from Duchemin (Duchemin et al. 2008). The Poisson's ratio for all the elements was set to 0.3.

Models were exported to Hypermesh (Altair Engineering, USA) in order to reproduce all experimental conditions (Input file). First, the nodes of the articular surface, where the impact force is transmitted, were retrieved. In order to do this, the laser scan acquisition (STL file) of the articular mold was superimposed to the finite element model. The elements of the model in contact with this surface were selected. From this selection of elements, a Scilab script selected the nodes of the articular surface of the model. The velocity of impact was tracked from the high speed videos of the ex-vivo protocol, and assigned to all these nodes.

The laser scan acquisition (STL file) of the distal radius, scanned before the impact, was imported to Hypermesh. The model was superimposed over this surface (articular mold), to match the exact position from the experimentation. The proximal bottom of the radius was constrained in the perpendicular direction to the impact. Also, at the bottom of the radius,

rigid elements were created to represent the mass of 12.5 Kg, used in the experimental set-up. These elements were built using the nodes of the hexahedral elements at the bottom. The density of these elements was adjusted for each of the radius model, to get a total mass 12.5 Kg. The final models had a number of elements between 76526 and 291277. The simulation was performed in LS-dyna explicit (LSTC, Livermore, United States). The total time simulated was 4 milliseconds with an average time step of $8x10^{-5}$.

A Scilab program was developed to process the result files after the simulations. The algorithm executes a batch analysis sequence of the d3plot file generated by LS-dyna after the simulation. The force overtime curve was obtained by the addition of the forces measured at the nodes of the articular surface. An example of the curve obtained is shown inFigure 4-5. Only the forces along the impact axis were considered.

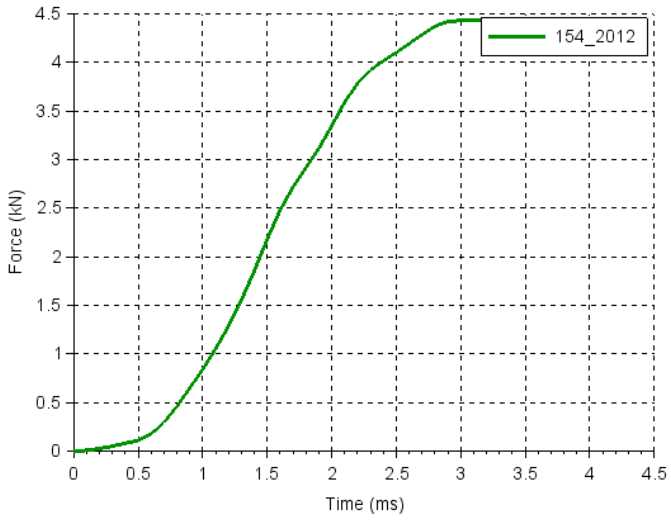

Figure 4-5 : Example of a force overtime curve for the whole distal radius model created using data from the ConeBeam CT. Force measured is the sum of the reaction forces of the nodes at the articular surface.

Maximum load during each experiment was compared to the corresponding subject specific-model.

The results are shown in the Figure 4-6.

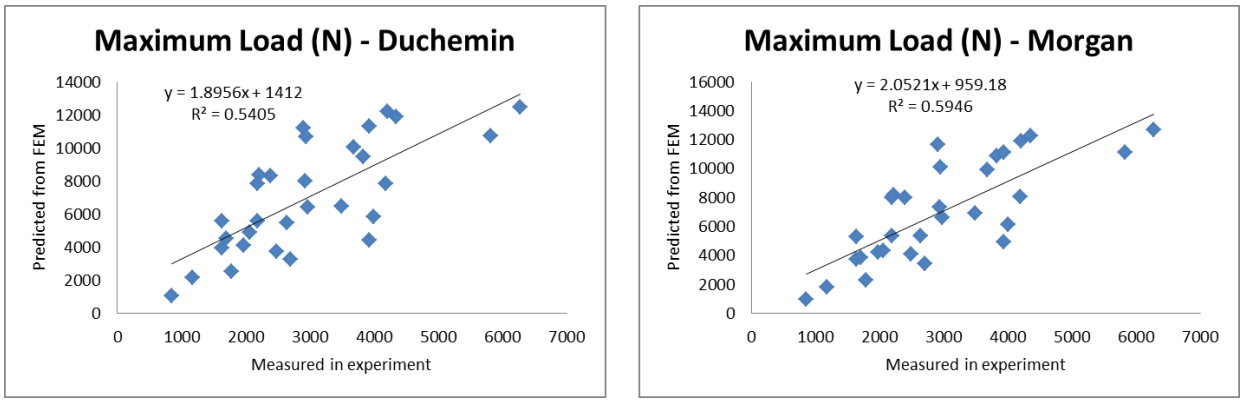

Figure 4-6 : Comparison between the experimental peak forces and the estimations from the heterogeneous model, with material properties deduced from the relationships a) left (Duchemin et al. 2008) and b) right (Morgan et al. 2003).

We can see that there is not a notorious difference for the models when using the relationships from (Duchemin et al. 2008) or (Morgan et al. 2003) for the material properties. Both models slightly overestimate the maximum load measured experimentally.

By using the standard error of the estimate (SEE), it is possible to quantify the accuracy of the estimations of the whole distal radius models. We can compare the results with the segment FEM. For this analysis we took the 14 fracture cases, in which the maximum load measured corresponds to the failure load. Table 4-4

	Segment Model						**Whole distal radius Model**	
Numerical Model (n=14)	Axial (=90°)	75°	60°	45°	30°	'YZ'	with properties from Duchemin	with properties from Morgan
SEE (N)	532	522	512	508	503	559	432	400

Table 4-4 : SEE value to measure the accuracy of the segment model and the whole distal radius model.(n=14).

Between the two whole distal radius models, we found that the model with the better accuracy was the one using the relationships from (Morgan et al. 2003).

This model performed also a better accuracy than any other of the segment models tested on Chapter 30. Indeed, when compared with the standard method (axial), the SEE of the whole distal radius is improved by 25%.

Finally, the Strain Energy density was visualized in the models of the bones that presented fractures types Colles' and Barton in the experimental behavior. The results are shown Figure 4-7.

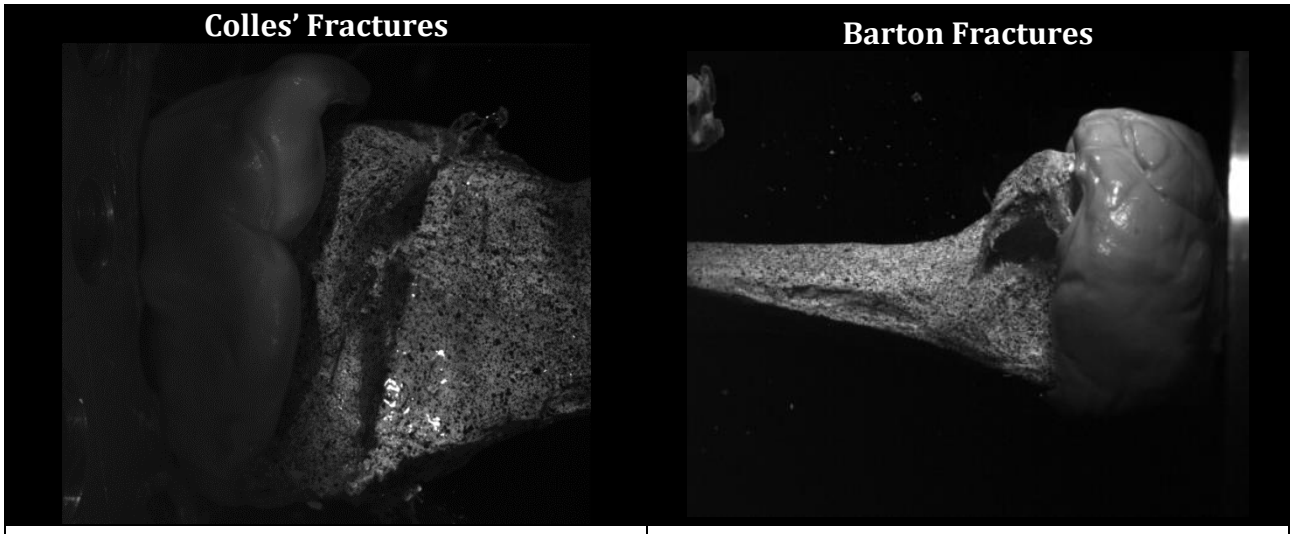

024_2011

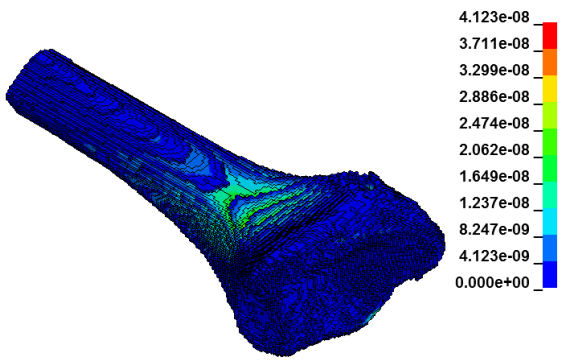

057_2010

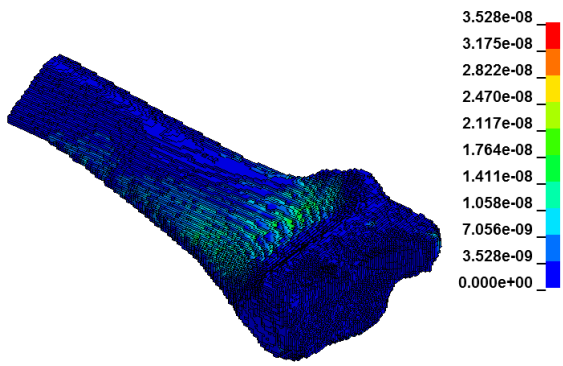

204_2012

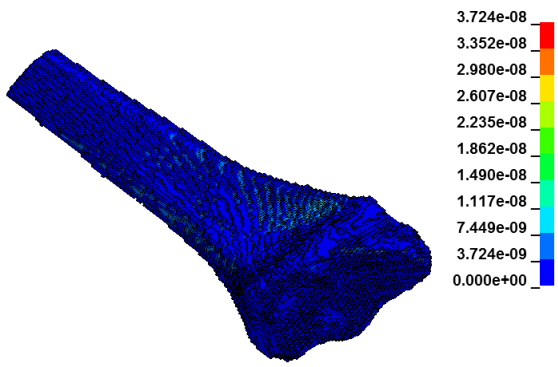

211_2010

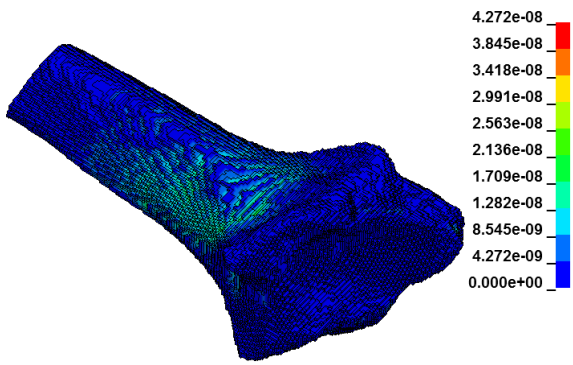

229_2009

232_2009

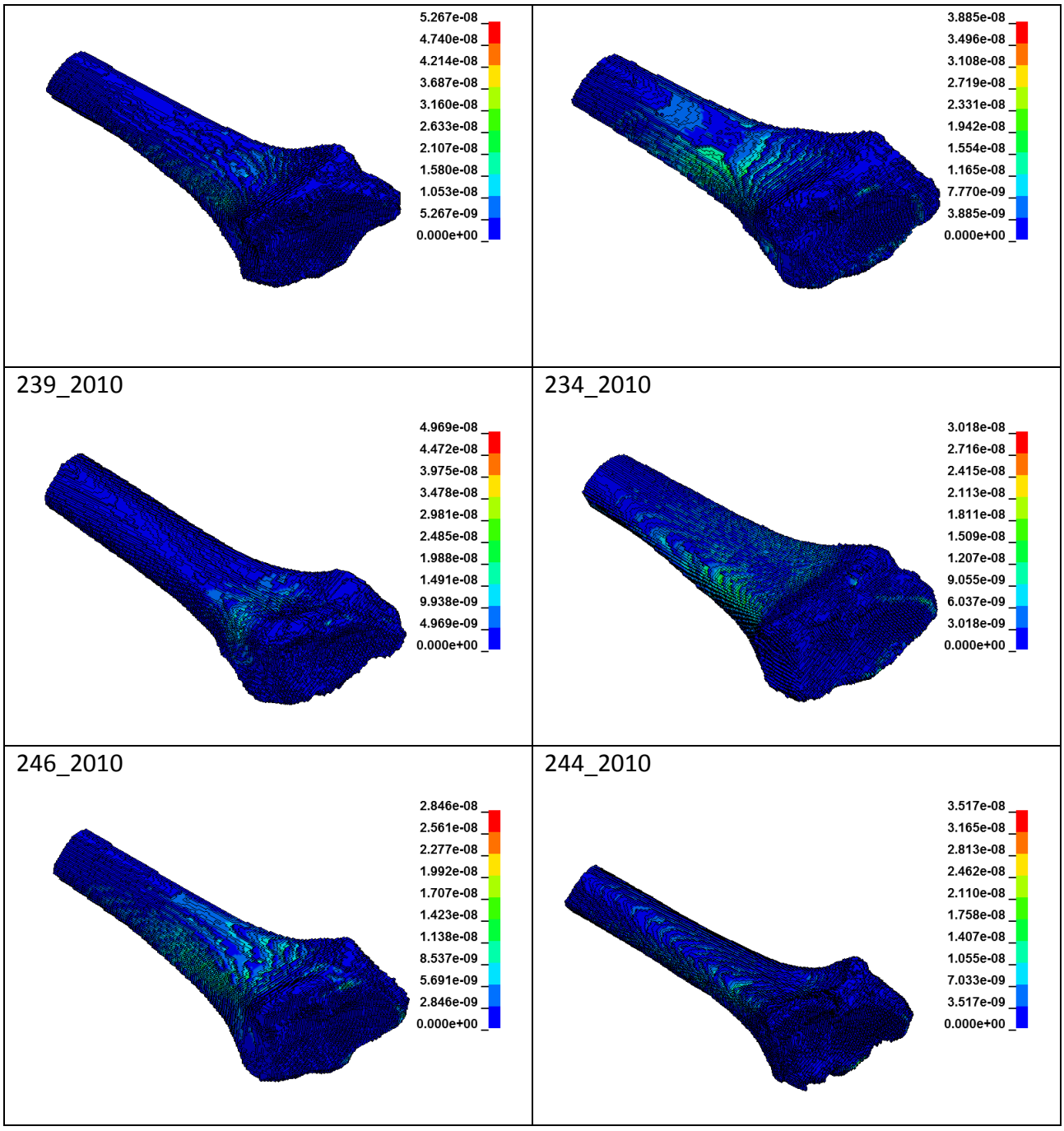

Figure 4-7 : Strain Energy density for the bones presenting a fracture type Colles or Barton in the ex-vivo test.

It was noticed that, in general, the Strain Energy Density is distributed along the axis for the bones that presents a Barton's fracture. A higher concentration is also found in the ulnar notch. In the model of bones that had Colles' fractures, the higher values of Strain energy density were located generally in the volar distal region.

4.3 Discussion

The model proposed presents a good accuracy, but some adjustments would need to be made before it can be used to develop a failure criterion. Particularly, the overestimation remains an issue. There are different reasons to explain this. First, the model was created using a voxel resize. Three voxels were converted into one. Thus, models underwent geometrical approximations, which probably affected the estimation of the cortical and trabecular thickness. These geometrical approximations seemed to lead to a stiffer model, probably because of the overestimation of thickness in the bone network. Nevertheless, this approximation is important from a calculation time perspective. Indeed, for one of the bones (medium density), which underwent a resize from 3 to 1, the number of elements was close to 45000, and more than one million and a half for the same bone without resize. The calculation time for the resized model was 4 minutes, and 2 hours for the non-resized model. Moreover, the scilab script failed to analyse the results of non-resized models.

As a perspective work, the models could be tested without resize and with a more sophisticated and efficient script to retrieve the results. However, for the medical diagnosis clinicians usually ask for as quick methods as possible and a method based on models demanding more than 2 hours of computation has limited interest in clinical practice.

Another problem with the estimation of the model could be found in the scan acquisitions. The samples were scanned using a Cone Beam CT scanner. Large fluctuations were found when doing the calibration. For example, for the bone 154-2012 the average value for the bone equivalent insert was (HU) 668.55, but the calibration curve was made with a value of 808.75. This means that for this bone, the calibration curve is 32% far from the average. This implies that the segmentation threshold is affected, as well as the material properties. A calibration made for each bone could outcome an improvement of the model. To quantify the difference between a mean and a specific calibration, we decided to compare the simulations obtained in a bone presenting large fluctuations (number 154-2012) with two calibration equations. The model using a specific calibration showed a maximum load value 11.8% lower than the measured by the model using the average calibration. A material card with a higher number of groups might also improve the results.

We computed the Standard Error of Estimation (SEE) in order to determine the whole distal radius model accuracy, and we compared with the accuracy results for the segment models. We found that the whole distal radius performed the best accuracy (i.e. lower SEE). This accuracy was found to be 25% better than using the segment model in standard axial loading. This result suggests that considering the velocity conditions and topology of the whole distal radius is able of improving the accuracy of the model.

The first qualitative analysis of the Strain energy density has shown, in most of the cases, a different pattern depending on the type of fracture observed experimentally (Barton or Colles). Further quantitative analysis should be able to show the existence of this differentiation. Nevertheless, the distribution of the Strain Energy Density is absolutely related to the structure of the bone network. It is possible that the model itself might not be completely representative of this structure, for example, because of the resizing process or because of the segmentation. Thus, the differentiation of the patterns could not be quantitatively demonstrated.

A further analysis will quantify the change over time of these measurements. We suggest that it is possible to find a threshold value of strain energy density, relating its distribution and magnitude, to predict the fracture. The distribution of this measurement seems to be different depending on the type of fracture. Then, different failure load criteria might came out to predict each type of fracture.

4.4 Conclusion

It was possible to create a model to estimate the maximum load in a forward fall case. The finite element model overestimate the maximum load observed experimentally. The precision of the model could be improved by avoiding resizing operations and by using particular calibrations for each sample. Nevertheless, it is important to keep in mind that a final clinical application would require a method with low calculation time. A good compromise should be found between the precision and the calculation time.

Beside these limitations, we were able to build a model for the estimation of the maximum loading during a forward fall case. By the measure of the standard error of the estimate, it

was found that the whole distal radius was 25% more accurate than the segment model to estimate the experimental failure load.

Using this whole distal radius model, we were able to have a first qualitative analyze of the results of the Strain Energy Density. This parameter might be useful to propose a failure criterion.

As a perspective, the model would be able of estimate the failure load by using measurements of strain energy density. In order to find this criterion, a logistic analysis could be made. Thus, it would be possible to evaluate the prediction of the fracture by changing the threshold value of strain energy density. This criterion could also involve a threshold value related to the quantity of material, which means, expressing the criterion also as function of the volume of bone involved. To better represent the experimental loading conditions in the model, it would be important to model the articular mold free to slide over the radial joint surface.

General Conclusion

Fragility fractures are a worldwide health problem. The standard method used in clinics to assess bone fragility uses bone density measurements by Dual X-ray absorptiometry (DXA). However this technique has shown limitations to predict the risk of fracture (Siris et al. 2001). The analysis of the bone fragility by micro-finite elements models (µFEM), created from High Resolution peripheral Quantitative Computed Tomography (HR-pQCT) is a promising method. The efficiency of this method has been probed to measure bone strength *in vivo*. However, it cannot be confirmed that the risk of fracture can be better assessed using µFEM than the classical density measurements by DXA (Rietbergen & Ito 2015).

The standard method of analysis of this µFEM is the static-axial loading. In this thesis, the assumption is that consideration of realistic loading conditions (orientation and velocity), in finite element models, could improve the assessment of the bone strength and the fracture risk.

The realistic condition considered was the forward fall, because it represents the most common case of fracture of the distal radius. Under this condition, the average angle between the volar face of the radius and the ground was 75° and the average velocity when impacting the ground was 2 m/s.

Experimental study: In the first phase we developed an ex-vivo experiment on 30 human radii, obtained after necropsy, to reproduce a forward fall case. This protocol applied an equal loading condition leaded to a classification into two groups: fractured and non-fractured radius. From this experiment, we were able to retrieve the maximum load at the articular surface of the radius, and also, strain values on the volar region and on the ulnar notch of the radius. This experiment leaded to 14 fractured bones over 30.

This data set was used for the evaluation of two types of radius FEM.

Segment model: One model was created using data from the HR-pQCT. This is the classical "9 mm radius segment model" used in the standard analysis by HR-pQCT. Another model was created and validated, based on HR-pQCT images, into Abaqus to apply different loading conditions (angles). Both models were similar.

Different angles for non-axial loading were used (forward fall: 75°, 60°, 45°, 30°, and backward fall: -45°). All the simulations (static, axial and non-axial) allowed significant distinction of the two groups: fractured and non-fractured. These models should then be able to discriminate the fracture. The magnitude of the experimental load was correctly estimated in all cases. For a non-axial loading, we found that the weaker the bone in the axial direction the higher the difference of failure load between the axial and non-axial direction.

The accuracy of the model was measured using the Standard Error of Estimation (SEE). It was found that the non-axial forward fall related models simulations have a higher accuracy than the axial model. This accuracy was higher for the lower angle. Nevertheless, the improvement is limited (5.5%).

The prediction of the risk of fracture remains low when using the φ ratio. However, using a threshold value of the failure load it was possible to estimate ~79% of the fracture cases and ~88% of the non-fractured cases, whatever the segment model used.

Improvements may be only achieved by doing important changes in the finite element model such as adding dynamic loading conditions in the segment or by selecting another loading condition, or constitutive law.

Whole distal radius model: The whole distal radius FEM was created using data from a Cone Beam Computed Tomography. This model simulated the dynamic non-axial loading conditions (2m/s and 75°) of the ex-vivo experiments representing one forward fall case. It was found that the whole distal radius model overestimated the maximum load observed experimentally by a factor of ~2. However, it was found that the whole distal radius model was 25% more accurate than the standard axial segment model, to estimate the experimental failure load (SEE = 400 N and 532 N respectively).

This study has different limitations. From the experimental part, the visual inspection of the fractured and non-fractured radii in the experimental protocol might lead to an over loaded bones. In case of a visual non fracture, the bone was re-loaded. This limitation was reduced using the videos, which allow replaying the test. For the whole distal model, the choice of

the resolution might have limited the accuracy, however a compromise had to be done between resolution, computational time and analysis of the results. Despite these limitations, the next step for this whole distal radius model would be the definition of a failure criterion, in order to assess fractured and non-fractured cases.

Perspectives:

In the ex-vivo protocol, we found that the articular mold (to simulate scaphoid and lunate) slides over the articular surface after the impact. A further more realistic whole distal radius model must include this feature in order to reproduce better what happens in real life.

A detailed strain analysis in the ex-vivo protocol, using the pattern painted in the bones and the high speed recordings will be part of a further work. This strain pattern will be useful for the validation of a failure criterion.

The estimation of fracture risk prediction, by the radius segment model from HR-pQCT, could be improved by using more complex loading than the uniaxial standard loading (compression and shear) in dynamic.

This study brought new data (ex vivo protocol with fractured and non-fractured groups) and modelling approaches to follow the work related to improvements of the fracture risk prediction.

Bibliography

Ackerman KE, Putman M, Guereca G, Taylor AP, Pierce L, Herzog DB, Klibanski A, Bouxsein M, Misra M. 2012. Cortical microstructure and estimated bone strength in young amenorrheic athletes, eumenorrheic athletes and non-athletes. Bone [Internet]. [cited 2013 Oct 14]; 51:680–7. Available from: http://www.pubmedcentral.nih.gov/articlerender.fcgi?artid=3482939&tool=pmcentrez&rendertype=abstract

Belloti JC, Santos JBG Dos, Erazo JP, Iani LJ, Tamaoki MJS, Moraes VY De, Faloppa F. 2013. A new method for classifying distal radius fracture: the IDEAL classification. Rev Bras Ortop (English Ed [Internet]. [cited 2014 Aug 8]; 48:36–40. Available from: http://linkinghub.elsevier.com/retrieve/pii/S2255497113000098

Bevill G, Keaveny TM. 2009. Trabecular bone strength predictions using finite element analysis of micro-scale images at limited spatial resolution. Bone [Internet]. 44:579–584. Available from: http://dx.doi.org/10.1016/j.bone.2008.11.020

Bhatia V a, Edwards WB, Troy KL. 2014. Predicting surface strains at the human distal radius during an in vivo loading task - Finite element model validation and application. J Biomech [Internet]. [cited 2014 Aug 11]; 47:2759–65. Available from: http://www.ncbi.nlm.nih.gov/pubmed/24882740

Blake GM, Fogelman I. 2007. The role of DXA bone density scans in the diagnosis and treatment of osteoporosis. Postgrad Med J. 83:509–517.

Boutroy S, Rietbergen B Van, Sornay-rendu E, Munoz F, Bouxsein ML, Delmas PD, Bmd A. 2008. Finite Element Analysis Based on In Vivo HR-pQCT Images of the Distal Radius Is Associated With Wrist Fracture in Postmenopausal Women. 23:392–399.

Bouxsein ML, Melton LJ, Riggs BL, Muller J, Atkinson EJ, Oberg AL, Robb R a, Camp JJ, Rouleau P a, McCollough CH, Khosla S. 2006. Age- and sex-specific differences in the factor of risk for vertebral fracture: a population-based study using QCT. J Bone Miner Res. 21:1475–1482.

Briot K, Cortet B, Roux C, Fardet L, Abitbol V, Bacchetta J, Buchon D, Debiais F, Guggenbuhl P, Laroche M, et al. 2014. 2014 update of recommendations on the prevention and treatment of glucocorticoid-induced osteoporosis. Joint Bone Spine [Internet]. [cited 2015 Sep 13]; 81:493–501. Available from: http://www.sciencedirect.com/science/article/pii/S1297319X14002206

Burkhart T a, Andrews DM, Dunning CE. 2012. Failure characteristics of the isolated distal radius in response to dynamic impact loading. J Orthop Res [Internet]. [cited 2014 Aug 11]; 30:885–92. Available from: http://www.ncbi.nlm.nih.gov/pubmed/22083972

Burkhart T a, Andrews DM, Dunning CE. 2013. Finite element modeling mesh quality, energy balance and validation methods: a review with recommendations associated with the modeling of bone tissue. J Biomech [Internet]. [cited 2014 Aug 11]; 46:1477–88. Available from: http://www.ncbi.nlm.nih.gov/pubmed/23623312

Burkhart T a, Quenneville CE, Dunning CE, Andrews DM. 2014. Development and validation of a distal radius finite element model to simulate impact loading indicative of a forward fall. Proc Inst Mech Eng H [Internet]. [cited 2014 Aug 11]; 228:258–71. Available from: http://www.ncbi.nlm.nih.gov/pubmed/24515978

Carter DR, Hayes WC. 1977. The compressive behavior of bone as a two-phase porous structure. J Bone Joint Surg Am [Internet]. [cited 2015 Apr 29]; 59:954–62. Available from: http://www.ncbi.nlm.nih.gov/pubmed/561786

Chapurlat R. 2013. Intérêt et limites du FRAX. Rev Rhum [Internet]. [cited 2014 Aug 11]; 80:334–336. Available from: http://linkinghub.elsevier.com/retrieve/pii/S1169833013000598

Chiu J, Robinovitch SN. 1998. Prediction of upper extremity impact forces during falls on the outstretched hand. J Biomech [Internet]. 31:1169–76. Available from: http://www.ncbi.nlm.nih.gov/pubmed/9882050

Christen D, Zwahlen A, Müller R. 2014. Reproducibility for linear and nonlinear micro-finite element simulations with density derived material properties of the human radius. J Mech Behav Biomed Mater [Internet]. [cited 2014 Nov 27]; 29:500–7. Available from: http://www.ncbi.nlm.nih.gov/pubmed/24216296

Crawford RP, Cann CE, Keaveny TM. 2003. Finite element models predict in vitro vertebral body compressive strength better than quantitative computed tomography. Bone [Internet]. [cited 2014 Aug 6]; 33:744–750. Available from: http://linkinghub.elsevier.com/retrieve/pii/S8756328203002102

Dalstra M, Huiskes R, van Erning L. 1995. Development and validation of a three-dimensional finite element model of the pelvic bone. J Biomech Eng. 117:272–278.

Depalle B, Chapurlat R, Walter-Le-Berre H, Bou-Saïd B, Follet H. 2013. Finite element dependence of stress evaluation for human trabecular bone. J Mech Behav Biomed Mater [Internet]. [cited 2013 Oct 14]; 18:200–12. Available from: http://www.ncbi.nlm.nih.gov/pubmed/23246384

Drake R, Vogl AW, Mitchell AWM. 2014. Gray's Anatomy for Students [Internet]. [place unknown]: Elsevier Health Sciences; [cited 2015 Oct 5]. Available from: https://books.google.com/books?id=Lh20BQAAQBAJ&pgis=1

Duchemin L, Mitton D, Jolivet E, Bousson V, Laredo JD, Skalli W. 2008. An anatomical subject-specific FE-model for hip fracture load prediction. Comput Methods Biomech Biomed Engin [Internet]. 11:105–111. Available from: http://www.tandfonline.com/doi/abs/10.1080/10255840701535965

Duma SM, Boggess BM, Crandall JR, MacMahon CB. 2003. Injury risk function for the small female wrist in axial loading. Accid Anal Prev. 35:869–875.

Eighth Bone Quality Seminar Proceedings 2013. 2014. Osteoporos Int [Internet]. [cited 2015 May 4]; 25 Suppl 3:S465–501. Available from: http://www.ncbi.nlm.nih.gov/pubmed/24894315

Fernandez DL. 2001. Distal radius fracture: the rationale of a classification. Chir Main [Internet]. 20:411–25. Available from: http://www.ncbi.nlm.nih.gov/pubmed/11778328

Frost HM. 1994. Wolff's Law and bone's structural adaptations to mechanical usage: an overview for clinicians. Angle Orthod. 64:175–188.

Genant HK, Engelke K, Fuerst T, Glüer CC, Grampp S, Harris ST, Jergas M, Lang T, Lu Y, Majumdar S, et al. 1996. Noninvasive assessment of bone mineral and structure: state of the art. J Bone Miner Res. 11:707–730.

Graeff C, Marin F, Petto H, Kayser O, Reisinger A, Peña J, Zysset P, Glüer C-C. 2013. High resolution quantitative computed tomography-based assessment of trabecular microstructure and strength estimates by finite-element analysis of the spine, but not DXA, reflects vertebral fracture status in men with glucocorticoid-induced osteoporosis. Bone [Internet]. [cited 2014 Nov 14]; 52:568–77. Available from: http://www.ncbi.nlm.nih.gov/pubmed/23149277

Grassi L, Schileo E, Taddei F, Zani L, Juszczyk M, Cristofolini L, Viceconti M. 2012. Accuracy of finite element predictions in sideways load configurations for the proximal human femur. J Biomech [Internet]. [cited 2013 Sep 28]; 45:394–9. Available from: http://www.ncbi.nlm.nih.gov/pubmed/22079387

Gray H a, Taddei F, Zavatsky AB, Cristofolini L, Gill HS. 2008. Experimental validation of a finite element model of a human cadaveric tibia. J Biomech Eng [Internet]. [cited 2014 Aug 8]; 130:031016. Available from: http://www.ncbi.nlm.nih.gov/pubmed/18532865

Greenwald RM, Janes PC, Swanson SC, McDonald TR. 1998. Dynamic impact response of human cadaveric forearms using a wrist brace. Am J Sports Med. 26:825–830.

Hayes WC, Piazza SJ, Zysset PK. 1991. Biomechanics of fracture risk prediction of the hip and spine by quantitative computed tomography. Radiol Clin North Am [Internet]. [cited 2015 May 7]; 29:1–18. Available from: http://www.ncbi.nlm.nih.gov/pubmed/1985322

Hazrati Marangalou J, Ito K, van Rietbergen B. 2012. A new approach to determine the accuracy of morphology-elasticity relationships in continuum FE analyses of human proximal femur. J Biomech [Internet]. [cited 2014 Aug 11]; 45:2884–92. Available from: http://www.ncbi.nlm.nih.gov/pubmed/23017379

Hosseini HS, Pahr DH, Zysset PK. 2012. Modeling and experimental validation of trabecular bone damage, softening and densification under large compressive strains. J Mech Behav Biomed Mater [Internet]. [cited 2013 Oct 14]; 15:93–102. Available from: http://www.ncbi.nlm.nih.gov/pubmed/23032429

Jayakar RY, Cabal A, Szumiloski J, Sardesai S, Phillips E a, Laib A, Scott BB, Pickarski M, Duong LT, Winkelmann CT, et al. 2012. Evaluation of high-resolution peripheral quantitative computed tomography, finite element analysis and biomechanical testing in a pre-clinical model of osteoporosis: a study with odanacatib treatment in the ovariectomized adult rhesus monkey. Bone [Internet]. [cited 2014 Aug 8]; 50:1379–88. Available from: http://www.ncbi.nlm.nih.gov/pubmed/22469953

Jupiter JB, Fernandez DL. 1997. Clinical Perspective Comparative Classification for Fractures of the Distal End of the Radius.

Kanis J a., Johnell O, Oden a., Johansson H, McCloskey E. 2008. FRAX??? and the assessment of fracture probability in men and women from the UK. Osteoporos Int. 19:385–397.

Kanis J a., Kanis J a. 1994. Assessment of fracture risk and its application to screening for postmenopausal osteoporosis: Synopsis of a WHO report. Osteoporos Int. 4:368–381.

Kanis JA, McCloskey E V, Johansson H, Cooper C, Rizzoli R, Reginster J-Y. 2013. European guidance for the diagnosis and management of osteoporosis in postmenopausal women. Osteoporos Int [Internet]. [cited 2015 Jul 26]; 24:23–57. Available from: http://www.pubmedcentral.nih.gov/articlerender.fcgi?artid=3587294&tool=pmcentrez&rendertype=abstract

Kazakia GJ, Nirody J a, Bernstein G, Sode M, Burghardt AJ, Majumdar S. 2013. Age- and gender-related differences in cortical geometry and microstructure: Improved sensitivity by regional analysis. Bone [Internet]. [cited 2013 Oct 14]; 52:623–31. Available from: http://www.ncbi.nlm.nih.gov/pubmed/23142360

Keller TS. 1994. PREDICTING THE COMPRESSIVE MECHANICAL BEHAVIOR OF BONE *. 27.

Laib a, Rüegsegger P. 1999. Comparison of structure extraction methods for in vivo trabecular bone measurements. Comput Med Imaging Graph [Internet]. 23:69–74. Available from: http://www.ncbi.nlm.nih.gov/pubmed/10227372

Laulan J, Bismuth J-P, Clément P, Garaud P. 2007. [An analytical classification of fractures of the distal radius: The “M.E.U.” classification]. Chir Main [Internet]. [cited 2014 Sep 29]; 26:293–9. Available from: http://www.ncbi.nlm.nih.gov/pubmed/18023236

Liu XS, Cohen A, Shane E, Yin PT, Stein EM, Rogers H, Kokolus SL, McMahon DJ, Lappe JM, Recker RR, et al. 2010. Bone density, geometry, microstructure, and stiffness: Relationships between peripheral and central skeletal sites assessed by DXA, HR-pQCT, and cQCT in premenopausal women. J Bone Miner Res [Internet]. [cited 2014 Nov 27]; 25:2229–38. Available from: http://www.pubmedcentral.nih.gov/articlerender.fcgi?artid=3128822&tool=pmcentrez&rendertype=abstract

Liu XS, Zhang XH, Sekhon KK, Adams MF, McMahon DJ, Bilezikian JP, Shane E, Guo XE. 2010. High-resolution peripheral quantitative computed tomography can assess microstructural and mechanical properties of human distal tibial bone. J Bone Miner Res [Internet]. [cited 2014 Aug 8]; 25:746–56. Available from: http://www.pubmedcentral.nih.gov/articlerender.fcgi?artid=3130204&tool=pmcentrez&rendertype=abstract

Macneil J a, Boyd SK. 2008. Bone strength at the distal radius can be estimated from high-resolution peripheral quantitative computed tomography and the finite element method. Bone [Internet]. [cited 2013 Sep 30]; 42:1203–13. Available from: http://www.ncbi.nlm.nih.gov/pubmed/18358799

MacNeil J a M, Adachi JD, Goltzman D, Josse RG, Kovacs CS, Prior JC, Olszynski W, Davison KS, Kaiser SM. 2012. Predicting fracture using 2D finite element modelling. Med Eng Phys [Internet]. [cited 2014 Aug 11]; 34:478–84. Available from: http://www.pubmedcentral.nih.gov/articlerender.fcgi?artid=4071042&tool=pmcentrez&rendertype=abstract

Mah P, Reeves TE, McDavid WD. 2010. Deriving Hounsfield units using grey levels in cone beam computed tomography. Dentomaxillofacial Radiol. 39:323–335.

Marshall D, Johnell O, Wedel H. 1996. Meta-analysis of how well measures of bone mineral density predict occurrence of osteoporotic fractures. BMJ [Internet]. [cited 2015 Mar 27]; 312:1254–9. Available from: http://www.pubmedcentral.nih.gov/articlerender.fcgi?artid=2351094&tool=pmcentrez&rendertype=abstract

Melton LJ, Christen D, Riggs BL, Achenbach SJ, Müller R, van Lenthe GH, Amin S, Atkinson EJ, Khosla S. 2010. Assessing forearm fracture risk in postmenopausal women. Osteoporos Int [Internet]. [cited 2014 Feb 28]; 21:1161–9. Available from: http://www.pubmedcentral.nih.gov/articlerender.fcgi?artid=2889027&tool=pmcentrez&rendertype=abstract

Morgan EF, Bayraktar HH, Keaveny TM. 2003. Trabecular bone modulus–density relationships depend on anatomic site. J Biomech [Internet]. [cited 2014 Jul 16]; 36:897–904. Available from: http://linkinghub.elsevier.com/retrieve/pii/S002192900300071X

Mosekilde L, Mosekilde L, Danielsen CC. 1987. Biomechanical competence of vertebral trabecular bone in relation to ash density and age in normal individuals. Bone. 8:79–85.

Mueller TL, Christen D, Sandercott S, Boyd SK, van Rietbergen B, Eckstein F, Lochmüller E-M, Müller R, van Lenthe GH. 2011. Computational finite element bone mechanics accurately predicts mechanical competence in the human radius of an elderly population. Bone [Internet]. [cited 2014 Nov 27]; 48:1232–8. Available from: http://www.ncbi.nlm.nih.gov/pubmed/21376150

Mueller TL, Stauber M, Kohler T, Eckstein F, Müller R, van Lenthe GH. 2009. Non-invasive bone competence analysis by high-resolution pQCT: an in vitro reproducibility study on structural and mechanical properties at the human radius. Bone [Internet]. [cited 2013 Oct 2]; 44:364–71. Available from: http://www.ncbi.nlm.nih.gov/pubmed/19027092

Niebur GL, Feldstein MJ, Yuen JC, Chen TJ, Keaveny TM. 2000. High-resolution " nite element models with tissue strength asymmetry accurately predict failure of trabecular bone. 33:1575–1583.

Pahr DH, Zysset PK. 2009. A comparison of enhanced continuum FE with micro FE models of human vertebral bodies. J Biomech [Internet]. [cited 2013 Oct 14]; 42:455–62. Available from: http://www.ncbi.nlm.nih.gov/pubmed/19155014

Pistoia W, van Rietbergen B, Lochmüller E-M, Lill C a, Eckstein F, Rüegsegger P. 2002. Estimation of distal radius failure load with micro-finite element analysis models based on three-dimensional peripheral quantitative computed tomography images. Bone [Internet]. 30:842–8. Available from: http://www.ncbi.nlm.nih.gov/pubmed/12052451

Popp AW, Windolf M, Senn C, Tami A, Richards RG, Brianza S, Schiuma D. 2012. Prediction of bone strength at the distal tibia by HR-pQCT and DXA. Bone [Internet]. [cited 2013 Oct 14]; 50:296–300. Available from: http://www.ncbi.nlm.nih.gov/pubmed/22088678

Rietbergen B Van, Ito K. 2015. A survey of micro- fi nite element analysis for clinical assessment of bone strength : The fi rst decade. J Biomech [Internet]. 48:832–841. Available from: http://dx.doi.org/10.1016/j.jbiomech.2014.12.024

Rietbergen B Van, Weinans H, Huiskes R, Odgaardt A. 1995. A NEW METHOD TO DETERMINE TRABECULAR BONE ELASTIC PROPERTIES AND LOADING USING MICROMECHANICAL FINITE-ELEMENT MODELS. 28:69–81.

Riggs BL, Melton LJ, Robb R a, Camp JJ, Atkinson EJ, Oberg AL, Rouleau P a, McCollough CH, Khosla S, Bouxsein ML. 2005. Population-Based Analysis of the Relationship of Whole Bone Strength Indices and Fall-Related Loads to Age- and Sex-Specific Patterns of Hip and Wrist Fractures. J Bone Miner Res [Internet]. 21:315–323. Available from: http://doi.wiley.com/10.1359/JBMR.051022

Roux C, Briot K. 2014. How long should we treat? Osteoporos Int [Internet]. [cited 2015 Oct 7]; 25:1659–1666. Available from: http://link.springer.com/10.1007/s00198-013-2433-3

Ruffoni D, Lenthe GH Van. 2011. Computational Method Relating Structure to Mechanical Function . In : P . Ducheyne , Author ' s personal copy 3 . 307 . Finite Element Analysis in Bone Research : A Computational Method Relating Structure to Mechanical Function. [place unknown]: Elsevier Ltd. Available from: http://dx.doi.org/10.1016/B978-0-08-055294-1.00093-3

Sapin-de Brosses E, Jolivet E, Travert C, Mitton D, Skalli W. 2012. Prediction of the vertebral strength using a finite element model derived from low-dose biplanar imaging: benefits of subject-specific material properties. Spine (Phila Pa 1976) [Internet]. [cited 2014 Nov 27]; 37:E156–62. Available from: http://www.ncbi.nlm.nih.gov/pubmed/22290213

Schileo E, Dall'ara E, Taddei F, Malandrino A, Schotkamp T, Baleani M, Viceconti M. 2008. An accurate estimation of bone density improves the accuracy of subject-specific finite element models. J Biomech [Internet]. [cited 2014 Aug 6]; 41:2483–91. Available from: http://www.ncbi.nlm.nih.gov/pubmed/18606417

Schileo E, Taddei F, Cristofolini L, Viceconti M. 2008a. Subject-specific finite element models implementing a maximum principal strain criterion are able to estimate failure risk and fracture location on human femurs tested in vitro. J Biomech [Internet]. [cited 2013 Sep 20]; 41:356–67. Available from: http://www.ncbi.nlm.nih.gov/pubmed/18022179

Schileo E, Taddei F, Cristofolini L, Viceconti M. 2008b. Subject-specific finite element models implementing a maximum principal strain criterion are able to estimate failure risk and fracture location on human femurs tested in vitro. 41:356–367.

Schileo E, Taddei F, Malandrino A, Cristofolini L, Viceconti M. 2007a. Subject-specific finite element models can accurately predict strain levels in long bones. J Biomech [Internet]. [cited 2013 Oct 10]; 40:2982–9. Available from: http://www.ncbi.nlm.nih.gov/pubmed/17434172

Schileo E, Taddei F, Malandrino A, Cristofolini L, Viceconti M. 2007b. Subject-specific finite element models can accurately predict strain levels in long bones. 40:2982–2989.

Segaren N, Cresswell T. 2013. Fractures of the forearm and carpus. Surg [Internet]. [cited 2014 Aug 8]; 31:155–161. Available from: http://linkinghub.elsevier.com/retrieve/pii/S0263931913000148

Siris ES, Chen Y-T, Abbott T a, Barrett-Connor E, Miller PD, Wehren LE, Berger ML. 2004. Bone mineral density thresholds for pharmacological intervention to prevent fractures. Arch Intern Med. 164:1108–1112.

Siris ES, Miller PD, Barrett-Connor E, Faulkner KG, Wehren LE, Abbott T a, Berger ML, Santora a C, Sherwood LM. 2001. Identification and fracture outcomes of undiagnosed low bone mineral density in postmenopausal women: results from the National Osteoporosis Risk Assessment. JAMA [Internet]. 286:2815–22. Available from: http://www.ncbi.nlm.nih.gov/pubmed/11735756

Taddei F, Cristofolini L, Martelli S, Gill HS, Viceconti M. 2006. Subject-specific finite element models of long bones: An in vitro evaluation of the overall accuracy. J Biomech [Internet]. [cited 2014 Aug 6]; 39:2457–67. Available from: http://www.ncbi.nlm.nih.gov/pubmed/16213507

Taddei F, Martelli S, Reggiani B, Cristofolini L, Viceconti M. 2006. Finite-element modeling of bones from CT data: sensitivity to geometry and material uncertainties. IEEE Trans Biomed Eng [Internet]. 53:2194–200. Available from: http://www.ncbi.nlm.nih.gov/pubmed/17073324

Taddei F, Pancanti A, Viceconti M. 2004. An improved method for the automatic mapping of computed tomography numbers onto finite element models. Med Eng Phys [Internet]. [cited 2014 Aug 6]; 26:61–69. Available from: http://linkinghub.elsevier.com/retrieve/pii/S1350453303001383

Tan J-S, Eng JJ, Robinovitch SN, Warnick B. 2006. Wrist impact velocities are smaller in forward falls than backward falls from standing. J Biomech [Internet]. [cited 2014 Aug 8]; 39:1804–11. Available from: http://www.ncbi.nlm.nih.gov/pubmed/16011836

Troy KL, Grabiner MD. 2007a. Asymmetrical ground impact of the hands after a trip-induced fall: experimental kinematics and kinetics. Clin Biomech (Bristol, Avon) [Internet]. [cited 2014 Jul 24]; 22:1088–95. Available from: http://www.pubmedcentral.nih.gov/articlerender.fcgi?artid=2099579&tool=pmcentrez&rendertype=abstract

Troy KL, Grabiner MD. 2007b. Off-axis loads cause failure of the distal radius at lower magnitudes than axial loads: a finite element analysis. J Biomech [Internet]. [cited 2014 Jul 11]; 40:1670–5. Available from: http://www.ncbi.nlm.nih.gov/pubmed/17368466

Ulrich D, van Rietbergen B, Weinans H, Rüegsegger P. 1998. Finite element analysis of trabecular bone structure: a comparison of image-based meshing techniques. J Biomech [Internet]. 31:1187–92. Available from: http://www.ncbi.nlm.nih.gov/pubmed/9882053

Varga P, Baumbach S, Pahr D, Zysset PK. 2009. Validation of an anatomy specific finite element model of Colles' fracture. J Biomech [Internet]. [cited 2013 Oct 14]; 42:1726–31. Available from: http://www.ncbi.nlm.nih.gov/pubmed/19467661

Varga P, Pahr DH, Baumbach S, Zysset PK. 2010. HR-pQCT based FE analysis of the most distal radius section provides an improved prediction of Colles' fracture load in vitro. Bone [Internet]. [cited 2014 Sep 29]; 47:982–8. Available from: http://www.ncbi.nlm.nih.gov/pubmed/20692389

Viceconti M, Davinelli M, Taddei F, Cappello A. 2004. Automatic generation of accurate subject-specific bone finite element models to be used in clinical studies. J Biomech [Internet]. [cited 2014 Jul 23]; 37:1597–605. Available from: http://www.ncbi.nlm.nih.gov/pubmed/15336935

Vilayphiou N, Boutroy S, Sornay-Rendu E, Van Rietbergen B, Munoz F, Delmas PD, Chapurlat R. 2010. Finite element analysis performed on radius and tibia HR-pQCT images and fragility fractures at all sites in postmenopausal women. Bone [Internet]. [cited 2014 Nov 14]; 46:1030–7. Available from: http://www.ncbi.nlm.nih.gov/pubmed/20044044

Vilayphiou N, Boutroy S, Szulc P, van Rietbergen B, Munoz F, Delmas PD, Chapurlat R. 2011. Finite element analysis performed on radius and tibia HR-pQCT images and fragility fractures at all sites in men. J Bone Miner Res [Internet]. [cited 2014 Jul 24]; 26:965–73. Available from: http://www.ncbi.nlm.nih.gov/pubmed/21541999

Vilayphiou N. 2012. Evaluation de la microarchitecture trab ´ eculaire et des propri ´ et ´ es m ´ ecaniques osseuses in vivo chez l ' humain par scanner p ´ eriph ´ erique a haute r ´ esolution : application clinique ` a l ' ost ´ eoporose HAL Id : tel-00730979.

Wolff J. 1986. The Law of Bone Remodelling [Internet]. Berlin, Heidelberg: Springer Berlin Heidelberg; [cited 2015 Mar 25]. Available from: http://link.springer.com/10.1007/978-3-642-71031-5

World Health Organization. 2004. Who scientific group on the assessment of osteoporosis at primary health care level. [place unknown].

Zysset PK, Dall'ara E, Varga P, Pahr DH. 2013. Finite element analysis for prediction of bone strength. Bonekey Rep [Internet]. [cited 2014 Aug 8]; 2:386. Available from: http://www.pubmedcentral.nih.gov/articlerender.fcgi?artid=3765052&tool=pmcentrez&rendertype=abstract

Appendix 1: Personal Communications

1 - International conferences with reviewing process

1-a Oral presentations

E. Zapata, H. Follet, D. Mitton; Homogeneous and heterogeneous finite element models to predict radius bone strength in forward fall configuration. Société de Biomécanique (SB), Paris (France), 28-30 October 2015. Proceedings in Computer Methods in Biomechanics and Biomedical Engineering, In press.

E. Zapata, H. Follet, D. Mitton; Ex-vivo protocol to reproduce a forward fall leading to fractured and non-fractured radii. International Research Council on Biomechanics of Injury (IRCOBI), Lyon (France), 9-11 September 2015. IRC 15-33, 221-226.

E. Zapata. J-B Pialat, H. Follet, D. Mitton; Assessment of a finite element model to reproduce an ex-vivo forward fall protocol leading to fractured and non-fractured radii. European Society of Biomechanics (ESB), Prague (Czech Republic), 5-8 July 2015.

E. Zapata, F. Duboeuf, R. Ellouz, S. Boutroy, D. Mitton, H. Follet; A methodology to assess non-axial loading on the distal radius. Société de Biomécanique, Valence (France), 23-29 August 2014. Proceedings in Computer Methods in Biomechanics and Biomedical Engineering, 17:sup1, 44-45

1-b Poster presentation

E. Zapata, F. Duboeuf, R. Ellouz, S. Boutroy, D. Mitton, H. Follet; Can non-axial loading improve failure prediction at the distal radius?. World Congress of Biomechanics, Boston (United States), 6-11 July 2014.

2 - Invited lecture

D. Mitton, E. Zapata, H. Follet. "Mechanical loading at the organ level: which consequences for bones?" Séminaire qualité osseuse. Paris (France). 19 June 2013. Osteoporosis International, Volume 25, Issue 3 Supplement, pp 465-501.

Ex vivo protocol to reproduce a forward fall leading to fractured and non-fractured radii

E. Zapata[1, 2, 3, 4], H. Follet[1, 2, 4], D. Mitton[1,2,3]

[1]Université de Lyon, F-69622, Lyon, France

[2]Université Claude Bernard Lyon 1, Villeurbanne, France

[3]IFSTTAR, UMR_T9406, LBMC Laboratoire de Biomécanique et Mécanique des Chocs, F-69675, Bron, France

[4]INSERM, UMR 1033, F-69008 Lyon, France.

Research question/objective

Forward falls represent a risk of injury for elderly. The risk is increased in elderly suffering from bone diseases, such as osteoporosis. Finite element model have been proposed to improve the bone strength prediction. However, these models have considered quasi-static loadings and a loading orientation along the distal radius whereas the real loading conditions in case of a fall are non-axial loadings (in most of the cases) and the loading speed could reach 2m/s in average. Thus, our research aims to consider more realistic loading conditions on the radius simulating a forward fall. The current ex vivo protocol was designed to load the radii with the same loading case expecting that some of them will fracture and others will not. These experimental data will be useful to assess the predictive capability of finite element models.

Methodology used

Six left radii from elderly donors (50 to 96 y.o.) were considered. Distal third of the radius was cut and cleaned of soft tissues. Samples were then potted in a polyurethane resin on a steel cylinder. Radii were placed with an alignment of 15° between the frontal anatomical plane and the anterior face of the radius, without any tilt in any other plane. This position reproduces alignment of the radius in the most common forward fall (Greewald et al, 1998). Each sample was then attached to 12.5 kg- mass (simulating part of the body mass) free to slide along the loading axis.

A rigid polyurethane mold was made for each radius. This mold is a simplified reproduction of the joint contact to spread the loading during the impact and was attached to the distal end of the radius.

The radius was then loaded trough the mold at 2m/s using a hydraulic testing machine (LF technologies, France). Loads, acceleration and displacement were recorded. In addition, four high speed videos (Photron SA3, Japan) recorded the impact. 3D surfacic strain during impact was computed using stereo-correlation (Vic-3D, Correlated Solutions, Germany).

Results

Among the 6 radii, 4 fractured and 2 did not. To illustrate the results, the example of two radii is considered in this abstract. The reaction load were respectively 1185 N and 2920 N. These results are in agreement with those reported in the literature (Burkhart et al., 2014). For the fractured radius, surfacic strain reached 2% on the anterior region of the radius and 3% on the ulnar side when fracture occurs. For the non-fractured radius, surfacic strain reached 1.5% on the anterior region of the radius and 2% on the ulnar side when fracture occurs.

Novelty.

This study provides a protocol to reproduce a fall on the radius. Most of the previous studies evaluate bone strength under static conditions. Moreover previous studies loaded radii until failure in all cases. In the current protocol a unique loading case was considered to get fractured and non-fractured radii. Having this two groups with known loading conditions (orientation and speed) will be of great interest to assess the predictive capability of finite element models.

Homogeneous and heterogeneous finite element models to predict radius bone strength in forward fall configuration

E. Zapata[abcd], H. Follet[abd], and D. Mitton*[abc]

[a]*Université de Lyon, F-69622, Lyon, France;* [b]*Université Claude Bernard Lyon 1, Villeurbanne, France;*

[c]*IFSTTAR, UMR_T9406, LBMC Laboratoire de Biomécanique et Mécanique des Chocs, F-69675, Bron, France ;*

[d]*INSERM, UMR 1033, F-69008 Lyon, France.*

Keywords: Forward fall, Bone strength, Distal radius, Finite element model.

1. Introduction

Fragility fractures of bones are a worldwide health problem. Actual golden standard methods to assess bone fragility have shown to be insufficient (Siris et al. 2004)(Chapurlat 2013). Finite element models (FEM) have been proposed to evaluate bone strength. The High-Resolution peripheral Quantitative Computed Tomography (HR-pQCT) uses a FEM to evaluate bone strength under a static axial load. Nevertheless, neither the golden standard methods nor FEM from HR-pQCT has considered realistic loading conditions. One important realistic condition is the forward fall, which is the most common kind of fall (Melton et al. 2010).

Previously, we developed and ex-vivo protocol to reproduce a forward fall. In this study we seek to develop a FEM capable of assess the strength of distal radius on this configuration.

2. Methods

2.1 Ex-vivo protocol

Six left radii from elderly donors (50 to 96 y.o) were tested in a fall configuration. The radius was potted in a polyurethane resin in a steel cylinder, with an angle of 75° (Figure 1) between the anterior face of the radius and the impactor.

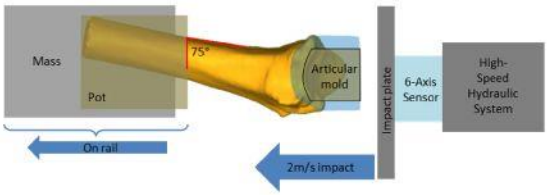

Figure 1. Schema of the impact test.

This position reproduces alignment of the radius in the most common forward fall (Chiu & Robinovitch 1998). The pot was placed in a horizontal cylinder bar on a rail system, which is free to slide along the loading axis. The radius was then loaded through a mold at 2m/s using a hydraulic high speed impact machine (LF technologies, France).

2.2 Finite Element Models

Previously acquired Cone Beam CT (CBCT) scans (NewTom 5G, QR, Verona, Italy) were used to create finite elements models. Because images from CBCT scans has shown not to be an accurate technique to deduce bone mineral densities (Kim 2014), thus we cannot deduce Young's moduli from DICOM images. We decide to evaluate one homogeneous model and four heterogeneous models using properties founded in literature (Burkhart et al. 2014)(Bosisio et al. 2007)(Vilayphiou et al. 2010). Details are shown on the section "properties" of the table 1.

The homogeneous models was segmented using CTAn (Bruker, Belgium). An adaptive threshold was defined to select bone from DICOM images. Then, hexahedral meshes were generated using an in-house software.

The heterogeneous models were segmented with a global threshold using Mimics (Materialise, Belgium). Thresholded selection were mapped into ten different masks, which were used later to assignate material properties. Hexahedral meshes were generated.

Models were exported to Hypermesh (Altair Engineering, USA) in order to reproduce all experiment conditions. In all the models, bone was considered as a linear elastic and isotropic material. Element size was 0.45mm. Measured velocity of the impactor in the experiment was imposed in the model at the loading region. Maximun load from the experiment were compared with the results from the simulation.

***Corresponding author. Email: david.mitton@ifsttar.fr**

		Input data		Prediction	
	FEM	**E (GPa)**	**Variation of E**	**Regression equation**	**R^2**
Homogeneous	**1**	10	No variation	$F_{FEM}=2.2*F_{EXP}-0.8$	0.91
Heterogeneous	**2**	From 0.02 to 17	Exponential	$F_{FEM}=3.1*F_{EXP}-2.4$	0.87
	3	From 0.02 to 10		$F_{FEM}=2.3*F_{EXP}-1.9$	0.87
	4	From 0.02 to 17	Linear	$F_{FEM}=5.1*F_{EXP}-1.0$	0.94
	5	From 0.02 to 10		$F_{FEM}=4.2*F_{EXP}-1.8$	0.94

Table 1. FEM input data and prediction capabilities (maximal loads in a forward fall)

3. Results and discussion

Experimental peak forces are in agreement with those reported in the literature (Burkhart et al. 2014). Determination coefficient R^2 and regression equations are shown in Table 1.

It was found that all the models overestimate the maximal load (with a ratio of 2.2 to 5.1). This can be due to the re-sizing (3 voxels merge into 1) made on the images before segmentation.

The homogeneous model has shown the lower overestimation. It is possible that the adaptive segmentation enhanced the porosity description and gave a more accurate description of cortical bone geometry.

Heterogeneous models were segmented using a global threshold. In order to avoid the loss of trabecular bone a wide threshold range was used, where marrow elements and remaining soft tissue was taken into account. Because of this segmentation, we decided to use a low Young's moduli for the weaker material (0.02 GPa), which is, in fact, a value previously used for marrow (Burkhart et al. 2014). According to the results, this technique could outcome in a stiffer model.

4. Conclusions

Maximal loads in the radius during a forward fall can be estimated using a homogeneous finite element model. Further analysis over 24 more oncoming samples will be performed to confirm this result.

Acknowledgements

We would like to thank Leila Ben Boubaker, Yves Caire, and Stéphane Ardizzone for their technical support. Also, J-L Milan, (Institut du Mouvement et de l'appareil Locomoteur - Team GIBoc, Hôpital Sainte-Marguerite, Université Aix Marseille), for his help with the software Mimics.

References

Bosisio MR, Talmant M, Skalli W, Laugier P, Mitton D. 2007. Apparent Young's modulus of human radius using inverse finite-element method. J Biomech. 40:2022–8.

Burkhart T a, Quenneville CE, Dunning CE, Andrews DM. 2014. Development and validation of a distal radius finite element model to simulate impact loading indicative of a forward fall. Proc Inst Mech Eng H. 228:258–71.

Chapurlat R. 2013. Intérêt et limites du FRAX. Rev Rhum. 80:334–336.

Chiu J, Robinovitch SN. 1998. Prediction of upper extremity impact forces during falls on the outstretched hand. J Biomech. 31:1169–76.

Kim D. 2014. Can Dental Cone Beam Computed Tomography Assess Bone Mineral Density ? Corresponding author. J Bone Miner Metab. 21:117–126.

Melton LJ, Christen D, Riggs BL, Achenbach SJ, Müller R, van Lenthe GH, Amin S, Atkinson EJ, Khosla S. 2010. Assessing forearm fracture risk in postmenopausal women. Osteoporos Int. 21:1161–9.

Siris ES, Chen Y-T, Abbott T a, Barrett-Connor E, Miller PD, Wehren LE, Berger ML. 2004. Bone mineral density thresholds for pharmacological intervention to prevent fractures. Arch Intern Med. 164:1108–1112.

Vilayphiou N, Boutroy S, Sornay-Rendu E, Van Rietbergen B, Munoz F, Delmas PD, Chapurlat R. 2010. Finite element analysis performed on radius and tibia HR-pQCT images and fragility fractures at all sites in postmenopausal women. Bone. 46:1030–7.

A methodology to assess non-axial loading on the distal radius

E. Zapata[1, 2, 3], F. Duboeuf[2, 3], R. Ellouz[2, 3], S. Boutroy[2, 3], D. Mitton[1], H. Follet[2, 3]

[1]*Université de Lyon, F-69622, Lyon; IFSTTAR, LBMC, UMR_T9406; Université Lyon 1, France.*

[2]*INSERM, UMR 1033, F-69008 Lyon, France.*

[3]*Université de Lyon, UMR 1033, F-69008 Lyon, France*

Keywords*:* High Resolution peripheral Quantitative Computed Tomography (HR-pQCT); Micro finite element analysis; Failure Load; Non-axial loading.

1. Introduction

Osteoporosis is a worldwide health problem related to bone fragility. Micro Finite Element Analysis (µFEA) based on High Resolution peripheral Quantitative Computed Tomography (HR-pQCT, Scanco) images are used to evaluate *in vivo* biomechanical properties (Boutroy et al. 2008). Most of the previous studies used an axial loading to assess bone strength. However, among fractures due to a fall from the standing height, only 15% are related to an axial loading (Melton et al. 2010). We assumed that a non-axial loading might be more discriminant to assess bone fracture. The main aim of our study is to develop a method to compare forearm strength using axial and non-axial loadings. To reach this goal a first step consists in 1/ developing a methodology to build a micro finite element model allowing non-axial loadings and 2/ comparing the results along with the standard HR-pQCT µFEA axial loading.

2. Methods

Areal bone mineral density (aBMD, g/cm2) measurements and ultra-distal T-score for twelve radii obtained from elderly female donors (Département Universitaire d'Anatomie Rockefeller, Lyon, France) were made from Dual X-Ray Absorptiometry (DXA) scans. From the results 6 radii were classed as normal (T-score>-1) and 6 other were classed as osteoporotic (T-score ≤ -2.5). Samples collection aged between 50 and 96 Y.O. They were then scanned on HR-pQCT at 82µm voxel size.

Clinical volume of interest of the radii (VOI), that corresponds to a 9mm reconstruction in the axial direction beginning 9mm proximal to the distal endplate of the radius, were segmented using the Scanco Medical standard evaluation software (Boutroy et al. 2005). Finite element models were created by converting each segmented bone voxel to an equally sized brick element (1 to 3.5 million elements). Material properties were chosen isotropic and elastic. In the same way as Pistoia's Study (Pistoia et al. 2002), a Young's modulus of 10GPa and a Poisson's ratio of 0.3 were assigned to all elements in the model. A standard µFEA was performed on HR-pQCT images with iplfe software (Scanco Medical), as detailed by (Boutroy et al. 2008). The simulation consisted in a linear analysis of a uniaxial compression of 1000 N on the distal cross-section. The proximal cross-section was blocked in all directions, to avoid displacement. Failure Load was assessed based on Pistoia's criterion (Pistoia et al. 2002). This criterion suggests that failure occurs when 2% of bone material is charged beyond 7000 micro-strains of effective strain.

Effective strain is defined as:

$$\epsilon_{eff} = \sqrt{\frac{2U}{E}} \qquad \text{(eq.1)}$$

Where U is the strain-energy density and E is the Young's modulus.

µFE models were exported on Abaqus (Dassault Systèmes), where non-axial and complex loadings were performed. The same material properties than previously used were set for this FEA analysis. A pre-simulation treatment was made for the 12 models on Hypermesh (Altair Hyperworks), consisting in a rotation around Z axis (bone principal axis) to get identical position for all the radii. Flat face of the anterior part of the radius was set parallel to X axis. The axial loading was simulated the same way as the referenced method. Radius VOI was fixed at the proximal cross-section and a compressive displacement of 10% of total length of the section was applied to the nodes of the distal cross-section. A non-axial 45° loading (YZ) was also evaluated by adding another equally displacement component on the Y axis.

Simulations were performed on a SGI ALTIX ICE computer at the Centre Informatique National de l'Enseignement Supérieur (CINES, Montpellier, France). All 12 simulations used 65 CPUs and took between 10.5 and 12.5 min.

Corresponding author: helene.follet@inserm.fr

From Abaqus, U value can be obtained for each mesh element. Using (eq.1), effective strain can be calculated for each element at final time of the simulation. A Matlab script was written in order to evaluate the criterion using results obtained from Abaqus simulation, considering that the effective strain increases linearly. This script uses an iteration method in order to get failure time, according to Pistoia's criterion. Then, as reaction force is assumed to increase linearly, failure load can be calculated. Results were analyzed statistically by non-parametric test.

3. Results and Discussion

Axial Failure Load obtained by iplfe & Abaqus softwares were strongly correlated (n=12, r=0.999, p<0.0001). Moreover, the Bland-Altman plot (Bland et Altman, 1986) showed that the difference obtained between software was within the mean of difference ±1.96SD. Mean difference in Failure load is 15.15±150 [-296, 198], which is inside the limits.

We found that axial and non-axial loadings showed statistically significant difference (Friedman test, p<0.0001).

The differences between the two loading directions are plotted along axial failure load (Figure 1).

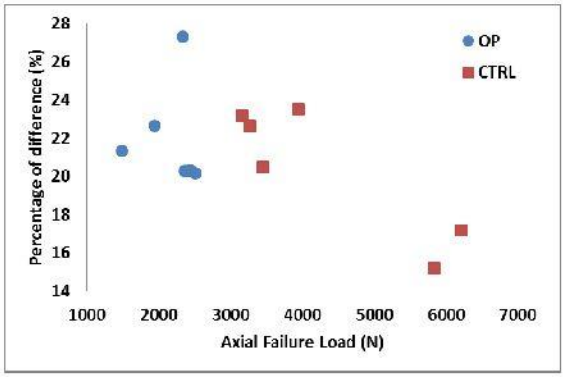

Figure 1 Loading orientation effect on failure strength for 12 radii (6 Normal – CTRL and 6 Osteoporotic - OP), difference between axial and non-axial compression (Percentage) vs axial Failure Load (N).

Our results suggest that the bones having the lower strength may be more sensitive to the direction of loading. This is an argument in favour of our assumption stating that non-axial loading might be discriminant to assess bone fracture.

4. Conclusions

The proposed method was in agreement with the referenced method and effective to measure the failure load under axial loading.
In addition our results suggest that non-axial loading might be of interest to assess bone fracture.

Acknowledgments

The authors are gratefully thankful to Dr. Frédéric Rongieras for his contribution to the bone collection.

References

Bland JM and Altman DG. 1986. Statistical Methods for Assessing Agreement between Two Methods of Clinical Measurement. Lancet. (8476): 307–10.

Boutroy S, Bouxsein ML, Munoz F, Delmas PD. 2005. In Vivo Assessment of Trabecular Bone Microarchitecture by High-Resolution Peripheral Quantitative Computed Tomography. J Clin Endocrinol Metab. 90(12): 6508–15.

Boutroy S, Van Rietbergen B, Sornay-Rendu E, Munoz F, Bouxsein ML, Delmas PD. 2008. Finite Element Analysis Based on In Vivo HR-pQCT Images of the Distal Radius Is Associated With Wrist Fracture in Postmenopausal Women. J Bone Miner Res. 23(3): 392–99.

Melton LJ 3rd, Christen D, Riggs BL, Achenbach SJ, Müller R, van Lenthe GH, Amin S, Atkinson EJ, Khosla S. 2010. Assessing Forearm Fracture Risk in Postmenopausal Women. Osteoporos Int. 21(7): 1161–69.

Pistoia W, van Rietbergen B, Lochmüller EM, Lill CA, Eckstein F, Rüegsegger P. 2002. Estimation of Distal Radius Failure Load with Micro-Finite Element Analysis Models Based on Three-Dimensional Peripheral Quantitative Computed Tomography Images. Bone. 30(6): 842–48.

Appendix 2: Summary in French

Introduction

Les fractures de fragilité sont un problème de santé publique dans le monde entier. Ces fractures, souvent causées par une chute de la position debout ou moins, sont liées à des maladies sous-jacentes générant fragilité osseuse. L'ostéoporose est l'une de ces maladies. Sa prévalence chez les femmes dans les plus grands pays de l'UE (France, Allemagne, Italie, Espagne et Royaume-Uni) est estimée à plus de 12 millions de cas (Kanis et al., 2013). Le diagnostic clinique s'effectue par mesure de la densité minérale osseuse par la méthode de référence: l'absorptiométrie bi-photonique à rayons X, (DXA). Cette mesure s'effectue sur différents sites anatomiques (fémur, radius, rachis), et est basée sur une projection 2D de la mesure du contenu minéral rapporté à la surface de projection. Malheureusement, la sensibilité de cette méthode est insuffisante et 50 % des fractures se produisent chez des patients considérés comme non ostéoporotiques (Siris et al., 2001). Les recherches en cours ont proposé différentes méthodes pour améliorer cette sensibilité. Une de ces méthodes est le FRAX, qui est un questionnaire combinant plusieurs facteurs (état de santé, taille, poids, BMD, …) pour estimer le risque de fracture survenant dix ans après. Cependant, cette méthode n'intègre pas les chutes et les troubles de la marche dans l'algorithme de prédiction (Chapurlat 2013). En d'autres termes, ce questionnaire ne prend pas en compte les conditions de chargement externes qui pourraient augmenter le risque de fracture. Une autre méthode qui a été proposée est l'analyse par des modèles de micro-éléments finis (µFEM) créés en utilisant un scanner clinique à très haute résolution (High resolution peripheric quantitative computed tomography, HR-pQCT) (Vilayphiou et al., 2010). Toutes les études de validation ont montré que l'estimation de la résistance osseuse est mieux réalisée par la µFEM (R^2 entre 0,73 et 0,92) que l'utilisation seule de mesures de la densité minérale par DXA (R^2 entre 0,31 et 0,71) (Rietbergen & Ito 2015). Malgré ce bon niveau de prédiction de la résistance osseuse, des études rétrospectives n'ont pas pu établir à ce jour que les µFEM sont de meilleurs prédicteurs du risque de fracture comparativement aux mesures de densité par DXA (Rietbergen & Ito 2015).

La méthode d'analyse standard en µFEM est l'application d'une charge statique axiale. Toutefois, dans le cas d'une chute, les vitesses d'application de cette charge peuvent atteindre 2 $m.s^{-1}$, ce qui est considéré comme un chargement dynamique. En outre, seul 15% des cas de chute est associé à une charge axiale sur le radius (Melton et al., 2010).

L'objectif de cette thèse est alors d'étudier l'influence de conditions réalistes de chargement (direction de chargement et vitesse), dans des modèles éléments finis pour l'évaluation de la résistance osseuse et la prédiction du risque de fracture. Cette étude a été réalisée en trois parties:

Dans la 1ère partie de ce travail, une expérimentation *ex-vivo,* sur radius humains obtenus après nécropsie, a été développée afin de reproduire un cas de chute. Cette expérimentation simulait le cas d'une chute vers l'avant, la main tendue, avec un angle entre la face antérieure du radius et le sol de 75 ° et une vitesse d'impact au sol de 2 $m.s^{-1}$. L'hypothèse de cette expérimentation est que le protocole choisit conduirait a deux groupes : un groupe « radius fracturé » et un « non fracturée » (Chapitre 2).

Dans la 2ème partie de ce travail, le modèle numérique clinique a été utilisé comme référence pour tester d'autres conditions de chargement. Ce modèle utilise de l'imagerie à très haute résolution (82 µm de taille de voxel isotropique) sur un segment de 9 mm au niveau du radius distal. Différents chargement non-axiaux en statique ont été testés et comparés à la configuration standard (Chapitre 3).

Dans la 3ème et dernière partie de ce travail, un modèle numérique hétérogène du radius « entier » a été créé. Pour se faire, les os ont été scannés sur un scanner dentaire classique à rayonnement conique New Tom, Verona, Italie). Les conditions limites de chargement expérimental ont été reproduites dans ce modèle (ie. Cas de chute vers l'avant), et les propriétés matérielles de l'os ont été considérés hétérogènes, et établies par identifications des niveaux de gris de l'imagerie scanner. L'essai à rupture a été simulé et la comparaison avec le modèle précédent a été effectuée (Chapitre 4).

Chapitre 1 : Contexte de l'étude

Les fractures de fragilité sont un problème de santé publique dans le monde entier. Ces fractures, souvent causées par une chute de la position debout ou moins, sont liées à des maladies sous-jacentes générant fragilité osseuse. L'ostéoporose est l'une de ces maladies. Sa prévalence chez les femmes dans les plus grands pays de l'UE (France, Allemagne, Italie, Espagne et Royaume-Uni) est estimée à plus de 12 millions de cas (Kanis et al., 2013). Le diagnostic clinique s'effectue par mesure de la densité minérale osseuse par la méthode de référence: l'absorptiométrie bi-photonique à rayons X, (DXA). Cette mesure s'effectue sur différents sites anatomiques (fémur, radius, rachis), et est basée sur une projection 2D de la mesure du contenu minéral rapporté à la surface de projection. Malheureusement, la sensibilité de cette méthode est insuffisante et 50 % des fractures se produisent chez des patients considérés comme non ostéoporotiques (Siris et al., 2001).

Les recherches en cours ont proposé différentes méthodes pour améliorer cette sensibilité. Une de ces méthodes est le FRAX, qui est un questionnaire combinant plusieurs facteurs (état de santé, taille, poids, BMD, …) pour estimer le risque de fracture survenant dix ans après. Cependant, cette méthode n'intègre pas les chutes et les troubles de la marche dans l'algorithme de prédiction (Chapurlat 2013). En d'autres termes, ce questionnaire ne prend pas en compte les conditions de chargement externes qui pourraient augmenter le risque de fracture.

Une autre méthode a été proposée comme une alternative pour l'évaluation de la fragilité osseuse. : La simulation numérique ou modèle en éléments finis. Ces modèles peuvent être très précis lors de la mesure résistance osseuse. La prédiction peut atteindre des valeurs proches de 98% (Macneil & Boyd 2008). En particulier, les modèles de micro-éléments finis (µFEM) créés en utilisant un scanner clinique à très haute résolution (High resolution peripheric quantitative computed tomography, HR-pQCT) (Vilayphiou et al., 2010). Toutes les études de validation ont montré que l'estimation de la résistance osseuse est mieux réalisée par la µFEM (R^2 entre 0,73 et 0,92) que l'utilisation seule de mesures de la densité minérale par DXA (R^2 entre 0,31 et 0,71) (Rietbergen & Ito 2015). Malgré ce bon niveau de prédiction de la résistance osseuse, des études rétrospectives n'ont pas pu établir à ce jour

que les µFEM sont de meilleurs prédicteurs du risque de fracture comparativement aux mesures de densité par DXA (Rietbergen & Ito 2015).

Le risque de fracture peut également être défini comme étant le rapport entre la charge externe appliquée à l'os sur la résistance osseuse (Hayes et al., 1991). Comme les µFEM estiment correctement la résistance osseuse, une meilleure prise en compte de la charge externe devrait conduire à une prévision améliorée du risque de fracture.

Pour la plupart des modèles numériques de radius, les conditions de chargement appliquées étaient une charge axiale quasi-statique. (Pistoia et al., 2002) (Macneil & Boyd 2008) (Varga et al., 2009) (Mueller et al., 2011) Or, en cas de chute, seulement 15% des cas sont associés à une charge axiale sur le radius (Melton et al., 2010) (Figure 0-1).

Figure 0-1 : Chutes possibles depuis la position debout (Melton et al., 2010)

Lors d'une chute vers l'avant, l'angle le plus communément trouvé entre le sol et le bras est de 75 ° (Greenwald et al., 1998) (Chiu & Robinovitch 1998) et la vitesse moyenne lorsque le sujet touche le sol est de 2 $m.s^{-1}$ (Tan et al . 2006) (Troy & Grabiner 2007a). Figure 0-2.

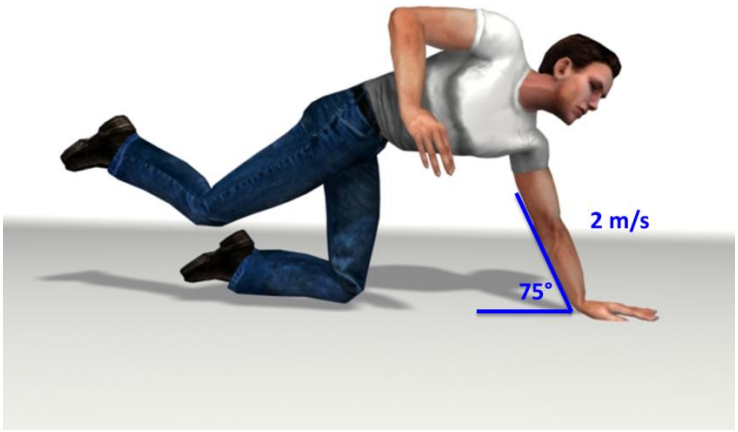

Figure 0-2 : Cas d'étude: chute vers l'avant, la main tendue. L'angle entre la face antérieure du radius est de 75 degrés et la vitesse est de 2 m / s

Dans une précédente étude, sur la façon dont le chargement mécanique affecte le comportement ultime des os, nous avons trouvé que la résistance osseuse est sensible à la fois à l'orientation, la position, la vitesse et la distribution (Actes du séminaire 2013. 2014). Expérimentalement, La résistance osseuse, a été estimée dans la plupart des cas, en utilisant des charges axiales quasi-statiques. De même, la plupart des modèles de prédiction du risque de fracture utilisent également des charges axiales quasi-statiques. D'autres études ont également évoqué à l'importance de l'orientation de chargement dans l'évaluation de la résistance osseuse (Troy & Grabiner 2007b) et (Burkhart et al. 2014).

En conséquence, nous avons fait l'hypothèse qu'une charge non axiale dynamique appliquée sur le radius pourrait être plus discriminante dans la détermination du risque de fracture et que le modèle numérique associé pourrait être amélioré en tenant compte de conditions de chargement réalistes, Dans ce contexte, les objectifs du travail de thèse sont les suivants:

Objectif 1:

• Développer une expérimentation ex-vivo sur radius humain afin de reproduire un cas de chute vers l'avant. Cette expérimentation servira à évaluer les capacités prédictives de différents modèles éléments finis.

Objectif 2:

• Evaluer les capacités de prévision d'un modèle numérique de segment de radius (9 mm) généré par HR-pQCT. Ce modèle sera tout d'abord testé pour la configuration axiale standard, puis, dans de nouvelles configurations non-axiales.

Objectif 3:

• Évaluer les capacités prédictive d'un modèle numérique de radius entier calé sur l'expérimental, afin d'évaluer l'effet de la géométrie et des conditions limites (conditions dynamiques et chargements non-axiaux).

Chapitre 2 : Protocole expérimental afin de reproduire une chute vers l'avant sur radius humain

Comme indiqué dans le chapitre précédent, nous avons décidé d'évaluer le comportement du radius dans des conditions de chargement réalistes. Nous avons voulu reproduire le cas d'une chute, dans lequel l'impact du radius sur le sol provoque une fracture ou non. Des travaux antérieurs ont évalué les cas de fractures vs non fractures sur radius dans des conditions non réalistes (charge axiale) (Douma et al., 2003), tandis que d'autres ont utilisé des conditions réalistes, mais ont plutôt étudié les cas de fractures par rapport à des pré-fractures sous impacts successifs. (Burkhart et al., 2012). Dans ce contexte, l'objectif de cette étude est de développer une expérimentation ex-vivo permettant de reproduire les conditions réalistes d'un cas de chute vers l'avant, ceci conduisant à un groupe de radius fracturé et un groupe non fracturé. Cette expérimentation servira à évaluer les capacités prédictives des modèles éléments finis présentés dans les chapitres 3 et 4.

Matériel et Méthodes :

Trente radius gauche de donneurs âgés (50-96 ans ± 12 ans, 13 hommes, 17 femmes) ont été prélevés après nécropsie. La partie distale du radius a été coupée et nettoyée des tissus mous. Les os ont ensuite été moulés dans une résine de polyuréthane dans un cylindre en acier. Les radius ont été positionnés avec un alignement de 15° entre le plan anatomique frontal et la face antérieure du radius, sans aucune inclinaison dans tout autre plan. Cette position reproduit l'alignement du radius lors de la chute la plus commune, soit vers l'avant (Greewald et al, 1998). Chaque os a ensuite été fixé à une masse de 12,5 kg (simulant une partie de la masse corporelle) libre de coulisser le long de l'axe de chargement.

Un joint rigide de polyuréthane a été fait pour chaque radius, reproduisant l'articulation « lunaute et scaphoïde ». Cette reproduction simplifiée a permis de répartir le chargement lors de l'impact et a été attaché à l'extrémité distale du radius.

Os	Effort Maximal (N) Test 1	Fx T1	Effort Maximal (N) Test 2	Fx T2	Effort Maximal (N) Test 3	Fx T3	Non Fx	Type de Fracture
013_2010	849	Oui						Proximale
024_2011	2971	Oui						Colles
056_2010	4203		3419	Oui				Colles
057_2010	2182	Oui						Barton
067_2010	4178		5986		4656		Oui	
090_2012	3990		3817	Oui				Barton
121_2010	2927	Oui						Complex
138_2011	3674		4180		3720		Oui	
154_2012	3925		2825	Oui				Barton
161_2012	2206		1592		1186		Oui	
166_2012	2478		1623		1793		Oui	
203_2012	2697		1421		723		Oui	
204_2012	1965	Oui						Colles
206_2010	4344		3465		2216		Oui	
211_2010	2903	Oui						Barton
213_2009	3486		2953	Oui				Barton
214_2009	1777	Oui						Proximale
215_2009	5818		4759	Oui				Colles
224_2009	1692		1341		1250		Oui	
225_2009	2936		2616		2625	Oui		Colles
229_2009	1629	Oui						Colles
230_2009	6265		4234	Oui				Barton
232_2009	2634	Oui						Barton
233_2009	2178		1640		1898		Oui	
234_2010	2381	Oui						Barton
239_2010	1176	Oui						Colles
243_2010	2055	Oui						Complèxe
244_2010	3825	Oui						Barton
246_2010	1625	Oui						Colles
250_2010	3929		3137		2197		Oui	
Moyenne ± SD (N)	2963 ± 1003		3063 ± 1062		2226 ± 864			

Table 0-1 : Forces maximales trouvées pendant l'expérimentation. FX Tn indique si une fracture a été detecté.. La colonne "Non FX" indique si l'échantillon n'a pas connu fracture après les trois impacts. La dernière colonne indique le type de fracture. Les principaux types de fractures sont de Barton et Colles.

Le radius a ensuite été testé par un impact à une vitesse de 2 $m.s^{-1}$ à l'aide d'une machine hydraulique (technologies de LF, France). Charges, accélération et déplacement ont été enregistrés. En outre, quatre caméras à grande vitesse d'acquisition (Photron SA3, Japon)

ont enregistré l'impact. La déformation 3D lors de l'impact a été calculée en utilisant de la stéréo-corrélation (Vic-3D, Solutions corrélés, Allemagne).

On récupère la force maximale pour chaque impact. Les résultats sont présentés dans le Table 0-1. Chaque os a été testé jusqu'à rupture, jusqu'à être chargé 3 fois max si la rupture n'était pas survenue après le 1er et le 2ème impact.

Parmi les 30 radius, 14 ont eu une fracture après le premier impact, 6, après le deuxième impact et un seul radius a présenté une fracture après le troisième impact. Neuf radius n'ont pas présenté de fracture (Figure 0-3).

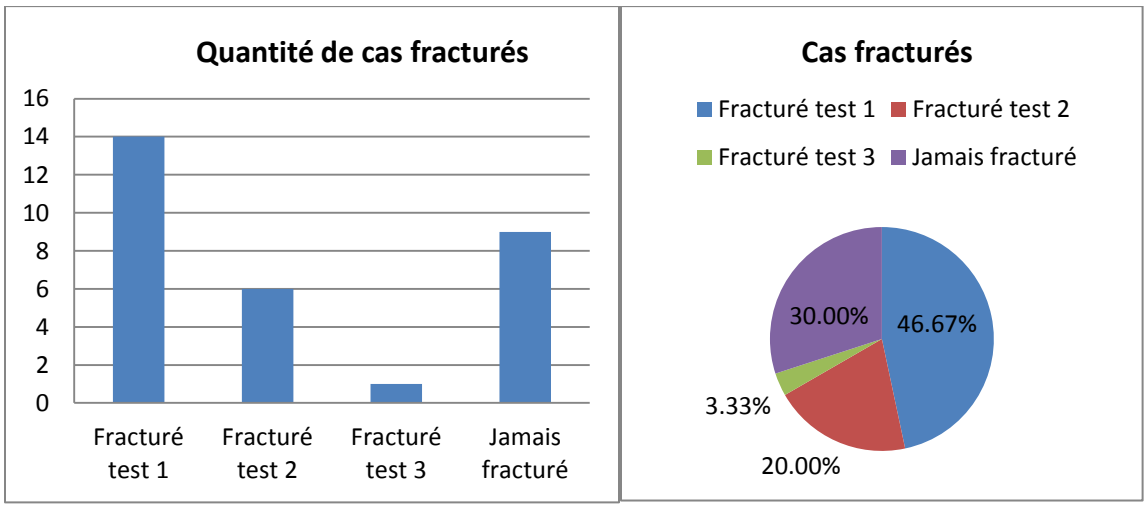

Figure 0-3 : Cas fracturés, exprimés en quantité et pourcentage

Le type de fracture est également indiqué dans le Tableau 2 1. Comme on peut le voir, les fractures prédominantes sont celles de type Colles et Barton 1.4.2. Les principaux types de fractures sont présentés dans la Figure 0-4.

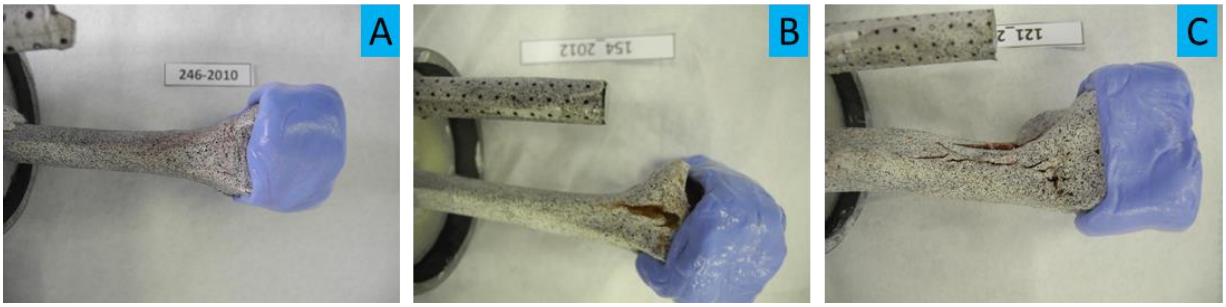

Figure 0-4 : Principale type de fracture trouve dans les expériences. A. Colles' fracture (raccourcissement radial). B. Barton fracture (volar). C. Fracture. Complèxe.

Les fractures de Colles sont sélectionnées par rapport au raccourcissement radial. Elles étaient stables, et la fracture était à peine visible par un simple aperçu de l'os.

La fracture de la Barton correspond à une dislocation de la face antérieure du radius. Dans cette expérimentation, le mouvement de la face antérieure provoque l'ouverture du radius en deux parties principales, le long de son axe longitudinal.

La confirmation du type de fracture a été faite en utilisant les vidéos à haute vitesse, mais aussi grâce à un radiologiste qui a vu les radios après impact. Ces vidéos ont permis de voir en détail le type de fracture et le moment de l'impact.

Deux autres fractures complexes ont également été trouvées. Ceci est le résultat de divers types de fractures, à savoir, plusieurs fractures propagent simultanément dans différentes directions. Cependant le mouchetis f s'était principalement déplacé de façon palmaire et radiale.

Discussion : cette expérimentation a fourni un protocole permettant de reproduire sur le radius une chute vers l'avant. La plupart des études précédentes ont évalué la résistance osseuse dans des conditions statiques.

La valeur moyenne des forces maximales expérimentales sont en accord avec celles rapportées dans la littérature: 2142 (1229) N (Burkhart et al 2014)..

Dans le protocole actuel, nous avons considéré un chargement unique pour tous les radius afin d'obtenir un groupe fracturés et un groupe non-fracturé. Cet objectif a été dès lors été atteint. Parmi les 30 radius testés, 14 ont eu une fracture après le premier impact. La

présence de ces deux groupes avec des conditions de chargement connus (orientation et de vitesse) sera nécessaire pour évaluer la capacité prédictive des modèles éléments finis. En observant les vidéos à haute vitesse, il a été constaté que, parmi les 30 radius, 8 présentaient un effet de glissement de l'articulation moulée sur la surface articulaire. La surface articulaire était en effet inclinée par rapport à la surface de la plaque d'impact. Cet angle est appelé l'inclinaison radiale (Figure 0-5).

Figure 0-5 : Un exemple d'une radiographie qui montre l'inclination radial.

Les observations suggèrent que lors d'un choc provoqué par une chute vers l'avant, le semi-lunaire et l'os scaphoïde peuvent glisser sur la surface articulaire si cette inclinaison radiale est importante.

Parmi ces 8 cas qui ont présenté un glissement du joint moulé, 7 n'ont jamais présenté une fracture, et 1 n'a présenté une fracture qu'au troisième impact.

Ceci n'est cependant pas un inconvénient de l'expérience. Il est en effet révélateur d'un comportement attendu de l'articulation dans une configuration réelle. En effet, lors d'une chute vers l'avant sur l'avant-bras, le semi-lunaire et l'os scaphoïde se déplacent partiellement dans le plan perpendiculaire à l'axe longitudinal du radius (Belloti et al.,

2013). Ainsi, le chargement peut changer par rapport aux conditions de charge initiales. En conséquence, les os avec une surface articulaire décalée peut ne pas fracturer, non pas du fait de sa force, mais tout simplement parce que le chargement a été diminué de fait.

En ce qui concerne l'analyse de la déformation par suivi de points, la plus haute déformation a été trouvée sur le côté cubital, tel que présenté dans la littérature (Burkhart et al., 2014). Une analyse plus poussée fournira une description plus détaillée de la localisation et de la valeur de ces déformations dans le temps.

En conclusion, trente radius ont été testés avec un chargement non-axial et dynamique afin de reproduire la chute la plus commune (chute vers l'avant). La plupart des études précédentes ont évalué la résistance osseuse dans des conditions statiques. En outre, dans tous les cas, les études précédentes ont chargés les radius jusqu'à la rupture. Dans le protocole actuel, un cas de chargement unique a été considéré pour obtenir des groupes fracturés et non fracturés. La présence de ces deux groupes avec des conditions de chargement connus (orientation et de vitesse) sera d'un grand intérêt pour évaluer la capacité prédictive des modèles éléments finis.

Chapitre 3 : Etude numérique: effet de la direction de chargement sur segment

Comme présenté dans le sous-chapitre 1.4.1.1, le HR-pQCT (Scanco médical) dispose d'un module d'analyse éléments finis (iplfe, μFEM) qui permet l'évaluation de la résistance osseuse numérique. L'évaluation est réalisée sur les os distaux: radius ou du tibia. Plusieurs études (Boutroy et al 2008; Macneil & Boyd 2008; Liu, , et al 2010) ont montré que cette FEA estime correctement la résistance des os. Ce programme utilise une configuration axiale de la charge. Comme évoqué précédemment (sous-chapitre 1.6.3), si nous prenons le cas de la chute de la position debout, seulement 15% des cas implique une charge axiale du radius (Melton et al., 2010). En outre, malgré le bon niveau de prédiction de la résistance osseuse par μFEM, il n'a pas été possible de confirmer que ces analyses numériques estiment mieux le risque de fracture que les mesures de la densité minérale osseuse par DXA (Rietbergen & Ito 2015). Nous supposons qu'avec une charge non axiale, on pourrait améliorer les capacités de prévision du modèle. Afin de tester cette hypothèse, nous avons utilisé les résultats obtenus à partir du chapitre 2. Nous avons créé un μFEM d'un segment de 9 mm (appelé "modèle de segment") des os testée expérimentalement, et nous avons utilisé la classification obtenue, (c.-à-fracturé et groupes non fracturé), pour estimer les capacités de prévision en utilisant le chargement axial et non-axial.

Tout d'abord, nous avons analysé les os de façon clinique, puis créé un nouveau modèle FE et comparé le comportement du modèle de segment sous la charge axiale standard et dans une configuration de chargement non-axiale arbitraire. Deuxièmement, nous évaluons cinq autres types de chargements non-axiaux liés à différents cas de chute. Enfin, nous avons comparé les estimations de la résistance osseuse avec la valeur mesurée expérimentalement, et avec également la possibilité d'évaluer le risque de fracture.

Le but de ce chapitre est donc d'évaluer la capacité de prédiction du segment de radius par simulation numérique en utilisant différentes orientations de chargement dans une configuration statique.

Dans un 1er temps, nous avons pu montrer que l'os avait numériquement un comportement différent en fonction de la direction de chargement. Ce résultat est cohérent, en raison de la structure, et à cause de l'anisotropie intrinsèque de la structure, qui est liée à la disposition

du réseau trabéculaire de l'os. L'angle de -45 ° sélectionnés pour cette étude, était une valeur arbitraire pour vérifier s'il n'y avait pas de différences notoires entre le chargement axial et le non axial. Il a été montré qu'en effet il y avait une différence statistiquement significative entre ces deux types de chargement (différence moyenne de 20%). Comme il a été discuté dans le chapitre 2, la fracture la plus fréquente dans le radius se produit lors d'une chute en avant de 75 ° entre la face antérieure du radius et le sol. Par conséquent, il est important d'estimer cette charge non axiale (75 °). Nous avons également examiné les orientations supplémentaires pour voir s'il y avait une direction spécifique présentant de meilleures capacités de discrimination de groupes.

Ainsi, pour cette étude, nous avons évalué différents angles qui pourraient se produire lors d'une chute. Nous avons étudié: la charge axiale (90 °), angle de 75 ° (chute libre), et trois autres angles (60 °, 45 ° et 30 °). Dans le cas de chute vers l'avant avec un angle de 90 ° toute la charge est transmise le long de l'axe de l'os, tandis que, pour le cas de chute vers l'avant, avec un angle de 30 °, la charge est à peine localisée le long de l'axe de l'os. 11 La figure 3 illustre la position de l'os sous ces différents angles.

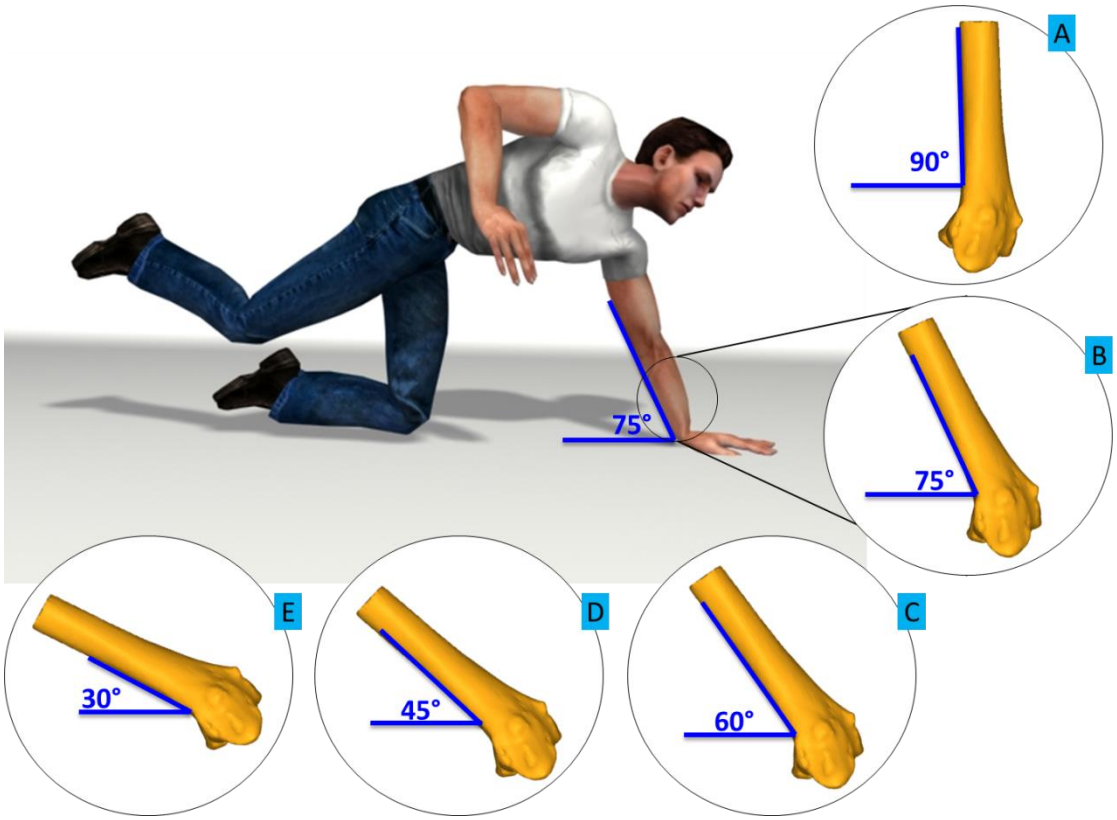

Figure 0-6 : Représentation de diffèrent angles possibles lors d'une chute vers l'avant. A. Axial B. 75° C. 60° D. 45° E. 30°.

Le segment préalablement simulé et créé à partir d'images à 82µm a été utilisé pour cet essai. Pour charger numériquement cet os, le segment a été repositionné, afin de représenter une chute vers l'avant (Figure 0-6, Figure 0-7)

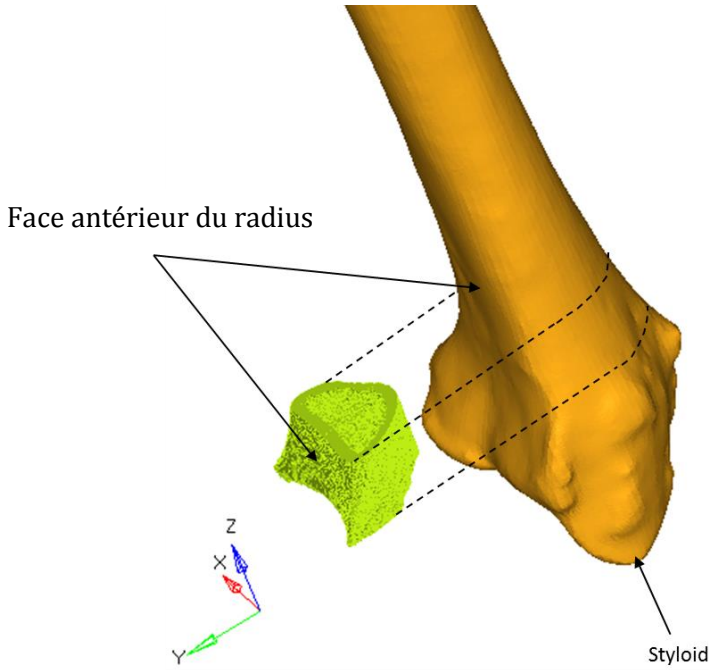

Figure 0-7 : Positionnement du segment distal de radius pour simulation de la chute souhaité

Comparaison avec l'expérimentation : Pour les cas fracturés expérimentalement, la force maximale correspond à la charge à la rupture. On peut alors comparer ce résultat avec la charge à rupture numérique établie à partir du critère de rupture de Pistoia

Nous avons également obtenu des différences statistiquement significatives entre les groupes fracturés et non fracturés en utilisant le BMD et tous les modèles numériques

Les premiers résultats indiquent que les os ayant la plus faible résistance peuvent être plus sensibles à la direction de chargement. Ceci est un argument en faveur de notre hypothèse affirmant que le chargement non-axial pourrait être plus discriminant pour évaluer la fracture osseuse.

L'utilisation des simulations avec chargement hors axe améliore légèrement la prédiction de la charge à rupture expérimentale. L'erreur standard d'estimation (SEE) est en effet améliorée de 5,5% en utilisant un modèle hors-axial par rapport au modèle axial.

Dans toutes nos simulations, en statique, le critère de Pistoia était capable de prédire la résistance de l'os, même dans les directions non-axiales. Néanmoins, la confrontation des modèles avec le facteur de φ, pour estimer leurs capacités de prévision, a montré un quota

inférieur de prédiction. Seuls 3 cas ont été prévus au cours des 14 cas de fractures (21,4%). Le modèle à -45° a présenté une meilleure prédiction des cas fracturés (64,3%), mais une faible prédiction des cas non fracturée (37,5%).

Cela pourrait signifier que le rapport de φ calculé avec une «condition de chute réelle en terme d'angle" n'est pas le plus adéquat pour prédire le risque de fracture pour le modèle de segment de radius par rapport aux données expérimentales. Basé sur notre expérimentation, nous connaissons la valeur de cette charge à rupture, mais dans la vraie vie, elle restera inconnue. Cependant, nous pouvons remarquer que Phi calculé avec un angle de chargement improbable discrimine mieux le groupe fracturé. Ainsi, il est important de considérer l'évaluation du risque de fracture sous un autre angle (autre condition de chargement) lors de l'utilisation la simulation numérique de segment de radius à partir de HR-pQCT.

En conclusion : Les images d'HRpQCT ont permis de générer notre propre modèle numérique afin d'y appliquer les conditions de chargement voulues. Dans la configuration standard, notre modèle était similaire à celui de l'HRpQCT. L'estimation de la charge de rupture expérimentale a été réalisée en utilisant la charge axiale standard. La précision de l'estimation n'a pas été améliorée en changeant la direction de la charge (5,5%). Cependant, tous les modèles ont permis la discrimination des groupes fracturés et non fracturés.

La prédiction du risque de fracture demeure faible lorsqu'on utilise le ratio de φ. Toutefois, en utilisant une valeur de seuil de la charge de rupture, il a été possible d'estimer ~ 79% des cas de fractures et ~ 88% des cas non fracturés.

En résumé, les charges non-axiales testées en statique ne sont pas en mesure d'améliorer la prédiction du risque de fracture actuellement faite par la charge axiale. L'amélioration pourra éventuellement être faite après d'importants changements dans le modèle d'éléments finis comme l'ajout de conditions de charges dynamiques dans le segment, en sélectionnant une autre condition de chargement, et une loi de comportement différente.

Chapitre 4 : Modèle éléments finis reproduisant une chute en avant sur radius distal ex vivo

Comme il a été montré dans le chapitre précédent, nous avons constaté que le modèle de segment est sensible à la direction du chargement. Néanmoins, lorsque l'on compare les modèles de segment avec les expériences ex-vivo, nous avons constaté que la précision, la discrimination et le niveau de détection ne sont pas notoirement améliorées par l'utilisation de modèles non-axiales. Le modèle de segment présente différentes limitations. Tout d'abord, l'échantillon se compose uniquement d'un segment d'une longueur peu inférieure à un centimètre. Même si cette partie pourrait être représentative de la mesure de différents paramètres (par exemple BV / TV, l'épaisseur corticale, aire corticale, etc.) (Macneil & Boyd 2008), ce modèle manque de représentativité de la structure globale.

Comme il a été indiqué dans le chapitre 2, dans le cas d'une chute il existe une faible influence de l'inclinaison radiale. Cet angle, qui mesure l'inclinaison de la surface articulaire, pourrait jouer un rôle important dans la résistance osseuse. Des valeurs plus élevées de l'inclinaison radiale peut provoquer une déviation de la charge d'impact lors d'une chute. Par conséquent, la prédiction de la capacité d'un modèle d'éléments finis prenant seulement une partie du radius pourrait être limitée.

En outre, l'évaluation du risque de fracture de l'os devrait inclure une analyse des conditions de charge réalistes en termes de vitesse. Si nous considérons le cas des chutes, le radius sera dans la plupart des cas affectés par des charges dynamiques non-axiales.

Voilà pourquoi nous avons décidé de développer un modèle en éléments finis du radius distal simulant les conditions de chargement (en orientation et en vitesse), pour le même cas de chute en avant que celui reproduit expérimentalement dans le chapitre 2.

Nous avons fait l'hypothèse que le modèle éléments finis du radius distal, reproduisant les conditions de chargement d'un cas de chute, pourrait être plus prédictif que les modèles qui évaluent la résistance osseuse sous charge statique axiale.

Ce chapitre présente le développement d'un modèle hétérogène et l'estimation de ses capacités de prédiction de la résistance osseuse. La précision de ce modèle de l'extrémité distal du radius par rapport au modèle de segment décrit le chapitre 3 est rapporté ci-après.

La charge maximale au cours de chaque expérience a été comparée au modèle spécifique de l'os correspondant. Nous avons trouvé qu'il n'y a pas de différence notoire pour les modèles utilisant les relations Duchemin et al., 2008 ou Morgan et al., 2003 pour les propriétés des matériaux. Les deux modèles surestiment légèrement la charge maximale mesurée expérimentalement.

En utilisant l'écart-type de l'erreur d'estimation (SEE), il est possible de quantifier la précision des estimations de l'ensemble des modèles du radius distal. Nous pouvons comparer les résultats avec le modèle segment. Pour cette analyse, nous avons pris les 14 cas de fractures, pour lesquels la charge maximale mesurée correspond à la charge de rupture. Table 0-2

	Model segment						**Modèle distale entière de radius**	
Model numérique (n=14)	Axial (=90°)	75°	60°	45°	30°	'YZ'	Avec propriétés Duchemin	Avec propriétés from Morgan
SEE (N)	532	522	512	508	503	559	432	400

Table 0-2 : SEE pour les modèles d'éléments finis (modèle segment et radius distal entier)

Pour les deux modèles du radius distal entier, nous avons trouvé que le modèle avec la plus grande précision est celui utilisant les relations de Morgan et al., 2003.

Ce modèle offre également une meilleure précision que l'ensemble des autres modèles de segments testés au chapitre 3. En effet, par rapport à la méthode standard (axial), la prédiction du modèle du radius distal entier est améliorée de 25%.

Enfin, la densité d'énergie de déformation a été visualisée dans les modèles des os qui ont présenté les types de fractures de Colles et Barton lors de l'expérimentation ex vivo. Les résultats sont montrés Figure 0-8.

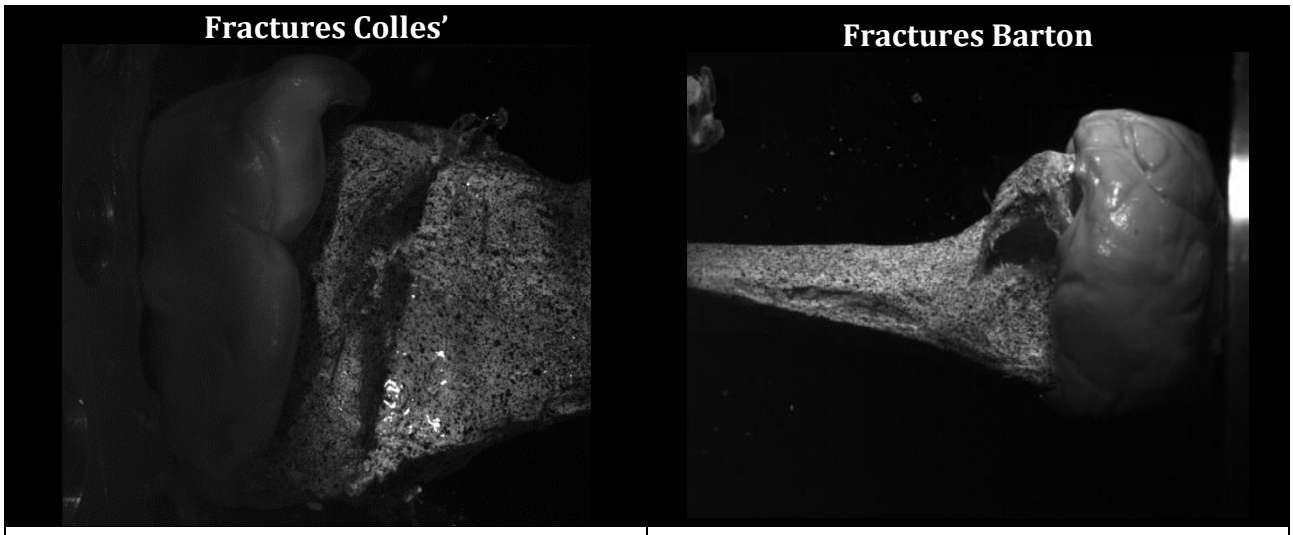

024_2011

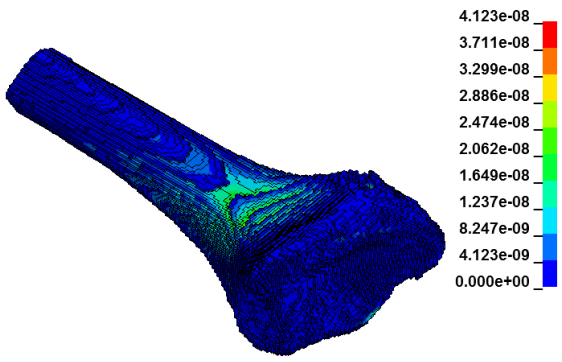

057_2010

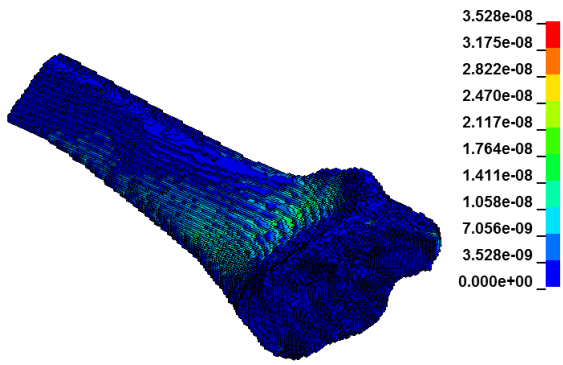

204_2012

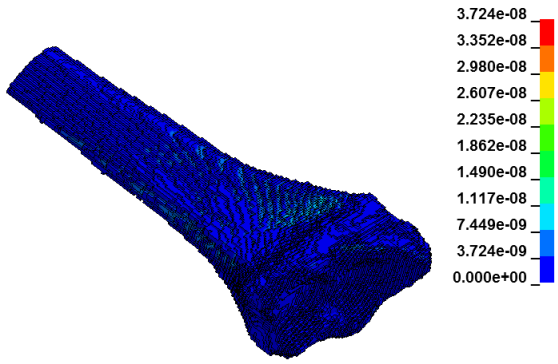

211_2010

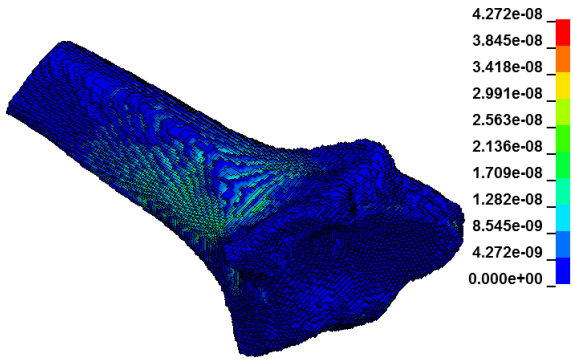

229_2009

232_2009

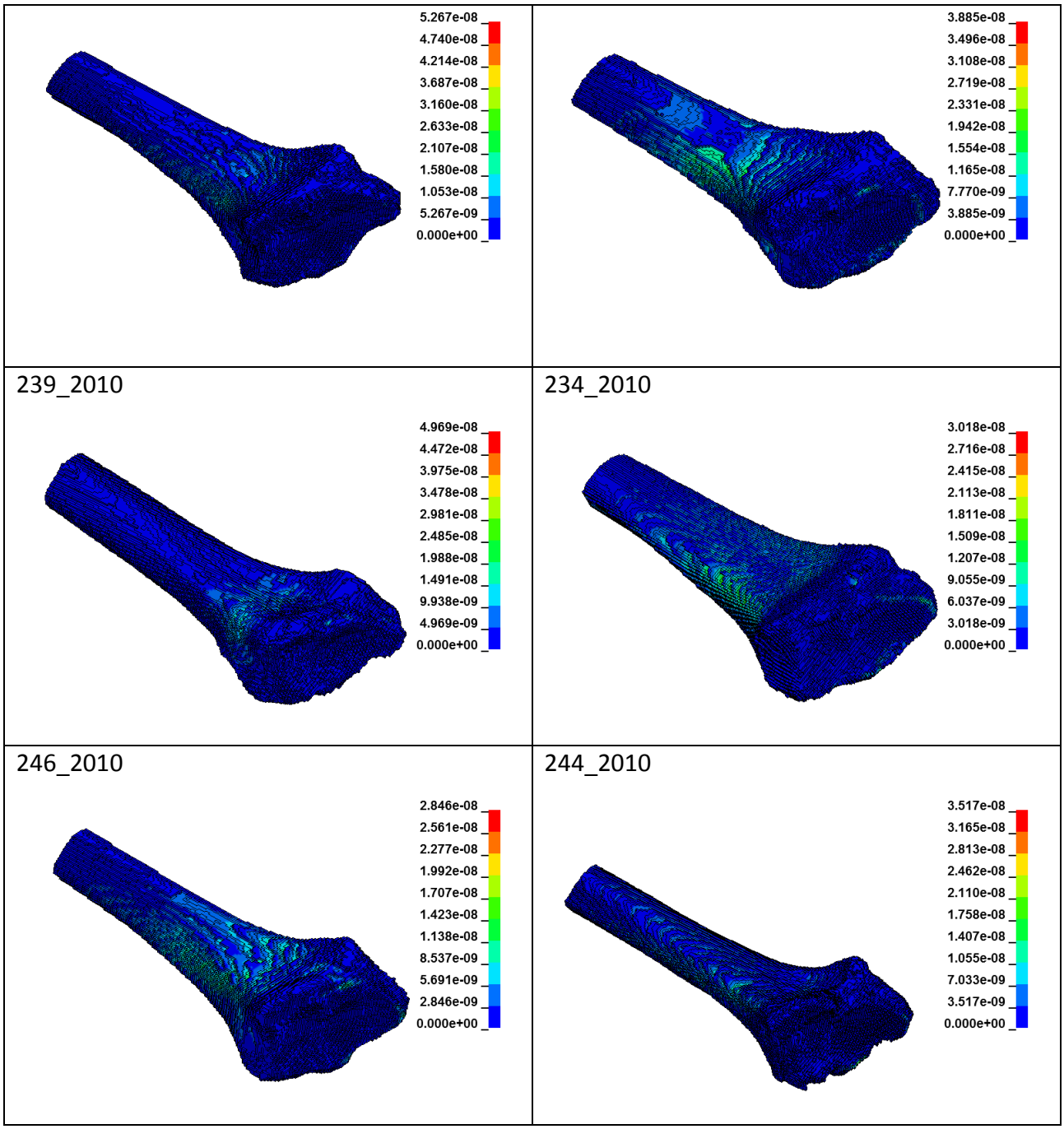

Figure 0-8 : Densité d'énergie de déformation pour les os qu'on présenté des fractures types Colles ou Barton dans le protocole ex-vivo.

Il a été remarqué qu'en général, la densité déformation d'énergie est répartie le long de l'axe pour les os qui présente une fracture de Barton. Dans les modèles des radius qui ont eu des fractures de Colles, les valeurs plus élevées de la densité d'énergie de déformation sont situées généralement dans la région distale palmaire.

Le modèle proposé présente une bonne précision, mais quelques ajustements doivent être apportés pour élaborer un critère de rupture. En particulier, la surestimation demeure un problème. Il y a différentes raisons pour expliquer cela. Premièrement, le modèle a été créé en utilisant une modification de taille de voxel. Trois voxels ont été convertis en un seul. Ainsi, les modèles ont subi des approximations géométriques, qui ont touché probablement l'estimation de l'épaisseur corticale et trabéculaire. Ces approximations géométriques semblent conduire à un modèle rigide, probablement en raison de la surestimation de l'épaisseur dans le réseau de l'os. Néanmoins, ce rapprochement est important du point de vue du temps de calcul. En effet, pour l'un des os (densité moyenne), qui a subi un redimensionnement 3-1, le nombre d'éléments était près de 45000, et plus d'un million et demi pour le même os sans redimensionnement. Le temps de calcul pour le modèle redimensionné était de 4 minutes et 2 heures pour le modèle non redimensionné. En outre, le script Scilab ne permettait pas d'analyser les résultats des modèles non redimensionnés.

Pour la suite, les modèles devront être testés sans redimensionnement et avec un script plus sophistiqué permettant de récupérer les résultats. Toutefois, pour les cliniciens, une méthode basée sur des modèles exigeants plus de 2 heures de calcul présente un intérêt limité dans la pratique clinique.

Une autre limite est liée au système tomographique utilisé pour construire les modèles. Les échantillons ont été analysés en utilisant un scanner CT à faisceau conique. Des fluctuations importantes ont été trouvées lors de l'étalonnage. Par exemple, pour l'os 154-2012 la valeur moyenne de l'insert était équivalente à un os (HU) 668,55, mais la courbe d'étalonnage a été réalisé avec une valeur de 808,75. Cela signifie que pour cet os, la courbe d'étalonnage était différente de 32% par rapport à la mesure de la moyenne. Cela signifie que le seuil de segmentation est affecté, ainsi que les propriétés du matériau. Un calibrage effectué pour chaque os pourrait améliorer le modèle. Pour quantifier la différence entre une calibration moyenne et une calibration spécifique, nous avons décidé de comparer les simulations obtenues dans un os présentant des fluctuations importantes (numéro 154-2012) avec deux équations d'étalonnage. Le modèle en utilisant un étalonnage spécifique a montré une valeur de charge maximale de 11,8% inférieure à celle obtenue avec le modèle utilisant le

calibrage moyen. Une carte de matériau avec un plus grand nombre de groupes pourrait également améliorer les résultats.

Nous avons calculé le SEE afin de déterminer la précision du modèle de radius distal entier et celle du modèle de segment. Nous avons constaté que le modèle du radius distal entier offre une précision Améliorée de 25% par rapport au modèle de segment (avec un chargement axial standard). Ce résultat suggère que tenir compte des conditions de vitesse et de la topologie de l'ensemble du radius distal permet d'améliorer la précision de la prédiction.

La première analyse qualitative de la densité d'énergie de déformation a montré, dans la plupart des cas, un profil différent selon le type de fracture observée expérimentalement (Colles ou Barton). L'analyse quantitative devrait être en mesure de démontrer l'existence de cette différenciation. Néanmoins, la répartition de la densité d'énergie déformation est liée à la structure du réseau de l'os. Il est possible que le modèle lui-même puisse ne pas être tout à fait représentatif de cette structure, par exemple, en raison du processus de redimensionnement ou à cause de la segmentation.

Une analyse plus approfondie permettra de quantifier l'évolution dans le temps de ces mesures. Nous suggérons qu'il est possible de trouver une valeur de seuil de la densité d'énergie de déformation pour prédire la fracture. La distribution de cette mesure semble être différente selon le type de fracture. Ainsi, différents critères de rupture seront peut-être nécessaire pour prédire chaque type de fracture.

Il était possible de créer un modèle pour estimer la charge maximale dans un cas de chute vers l'avant. Toutefois, le modèle éléments finis surestime la charge maximale observée expérimentalement. La précision du modèle pourrait être améliorée en évitant les opérations de redimensionnement et en utilisant les étalonnages particuliers pour chaque échantillon. Néanmoins, il est important de garder à l'esprit qu'une application clinique final exigerait une méthode à faible temps de calcul. Un bon compromis doit être trouvé entre la précision et le temps de calcul.

Au-delà de ces limitations, nous avons pu construire un modèle pour l'estimation de la charge maximale lors d'un cas de chute vers l'avant. Par la mesure de l'ecart-type de l'erreur d'estimation, il a été constaté que le modèle de la partie distale du radius était de 25% plus précis que le modèle de segment pour estimer la charge à la rupture expérimentale.

En utilisant ce modèle du radius distal, nous avons obtenu une première analyse qualitative des résultats de la densité d'énergie de déformation. Ce paramètre pourrait être utile de proposer un critère de rupture.

Afin de trouver ce critère, une analyse logistique pourrait être faite. Ainsi, il serait possible d'évaluer la prédiction de la fracture en modifiant la valeur de seuil de la densité d'énergie de déformation. Ce critère peut aussi comporter une valeur de seuil relative à la quantité de matériau, en exprimant le critère également comme fonction du volume de l'os concerné. Pour mieux représenter les conditions de chargement expérimentales dans le modèle, il serait important de modéliser le moule articulaire libre de glisser sur la surface articulaire du radius.

Conclusion générale

Les fractures de fragilité sont un problème de santé dans le monde entier. La méthode clinique standard pour d'évaluer la fragilité des os utilise des mesures de la densité osseuse par absorptiométrie biphotonique à rayons X (DXA). Cependant, cette technique manque de sensibilité pour prédire le risque de fracture (Siris et al. 2001). L'analyse de la fragilité de l'os par des modèles micro éléments finis (μFEM), créés à partir de tomodensitométrie périphérique haute résolution (HR-pQCT) est une méthode prometteuse. L'efficacité de cette méthode a été démontrée pour mesurer la résistance de l'os in vivo. Cependant, il ne peut pas être confirmé que le risque de fracture peut être mieux évalué en utilisant les μFEM qu'en utilisant les mesures de densité classiques par DXA (Rietbergen & Ito 2015).

La méthode standard d'analyse par μFEM est le chargement statique axial. Dans cette thèse, l'hypothèse est que l'examen des conditions de chargement réalistes (en orientation et en vitesse), dans les modèles en éléments finis, pourrait améliorer l'évaluation de la solidité osseuse et du risque de fracture.

Le chargement lié à la chute en avant a été considéré, car il représente le cas le plus fréquent de fracture du radius distal. Sous cette condition, l'angle moyen entre la face antérieure du radius et le sol est de 75 ° et la vitesse moyenne en cas d'impact au sol est de 2 m/s.

Etude expérimentale: Dans la première phase, nous avons développé une expérience ex-vivo sur 30 radius humains pour reproduire un cas de chute vers l'avant. Le chargement moyen appliqué à l'ensemble des radius a permis de créer deux groupes: fracturés et non fracturés. A partir de cette expérience, nous avons été en mesure de récupérer la charge maximale à la surface articulaire du radius, et également, les valeurs de déformation sur la région palmaire et sur l'encoche ulnaire du radius. Cette expérience a conduit à 14 os fracturés sur 30.

Cet ensemble de données a été utilisé pour l'évaluation des deux types de modèles du radius.

Modèle de segment: Un modèle a été créé en utilisant les données de la HR-pQCT. Ceci est le «modèle de segment de radius 9 mm" classique utilisé dans l'analyse standard par HR-pQCT. Un autre modèle a été créé et validé, basé sur les images HRpQCT, dans Abaqus pour appliquer différentes conditions de chargement (angles). Il a été montré que les deux modèles sont similaires.

Différents angles de chargement non-axial ont été utilisés (chute vers l'avant: 75 °, 60 °, 45 °, 30 °, et chute en arrière: -45 °). Toutes les simulations (statique, axiale et non-axiale) conduisent à des résultats significativement différents entre les deux groupes: fracturé et non fracturé.. La valeur de la charge expérimentale a été correctement estimée quel que soit l'angle de chargement considéré. Il a été trouvé que la différence entre le chargement axial et non axial augmentait lorsque la résistance de l'os diminuait.

La précision du modèle a été mesurée en utilisant le SEE. Il a été constaté que les modèles avec un chargement non-axial ont eu meilleure précision que le modèle avec un chargement axial. Cette précision était améliorée pour l'angle le plus faible (30°). Néanmoins, l'amélioration reste limitée (5,5%).

La prédiction du risque de fracture demeure faible lorsqu'on utilise le ratio φ. Cependant, en utilisant une valeur seuil de la charge de rupture simulée, il a été possible d'estimer ~ 79% des cas de fracture et ~ 88% des cas non fracturé, quel que soit le modèle de segment utilisé.

Des améliorations peuvent être apportées comme l'ajout de conditions de charge dynamique dans le segment, la sélection d'une autre condition de chargement, ou le changement de la loi de comportement.

Modèle du radius distal entier: Le modèle du radius distal entier a été créé en utilisant les données d'une tomodensitométrie à faisceau conique. Ce modèle intègre les conditions de chargement dynamique non-axial (2m/s et 75 °) des expériences ex vivo représentant une chute en avant. On a constaté que le modèle de radius distal entier surestime la charge maximale observée expérimentalement par un facteur 2 ~. Cependant, on a constaté que le modèle de radius distal entier était 25% plus précis que le modèle de segment axial

standard, pour estimer la charge à la rupture expérimentale (SEE = 400 N et 532 N respectivement).

Cette étude présente différentes limites. Pour la partie expérimentale, l'inspection visuelle des radius fracturé et non fracturée ne peut confirmer à 100% la présence ou l'absence de fracture. Ce risque a été réduit en utilisant les vidéos, qui permettent de revisualiser le test au ralenti. Pour le modèle du radius distal entier, un compromis devait être fait entre la résolution, le temps de calcul et l'analyse des résultats. La prochaine étape serait la définition d'un critère de rupture pour le modèle de du radius distal entier, afin de discriminer les cas fracturés et non fracturés.

Perspectives:

Au cours de l'expérimentation ex vivo, nous avons trouvé que le moule articulaire (représentant le semi-lunaire et le scaphoïde) glisse sur la surface articulaire après l'impact. Un modèle encore plus réaliste de radius distal entier doit inclure ce comportement

Une analyse détaillée de la déformation dans le protocole ex vivo, en utilisant le motif peint dans les os et les enregistrements à haute vitesse, devra être menée. Ces données de déformation seront utiles pour la validation d'un critère de rupture.

L'estimation de la prédiction du risque de fracture, par le modèle de segment de radius à partir de HR-pQCT, pourrait être améliorée en utilisant le chargement plus complexe que le chargement standard uniaxial (compression et cisaillement en dynamique).

Cette étude a apporté de nouvelles données (expérimentation ex vivo avec deux groupes : fracturés et non fracturés) et des approches de modélisation pour poursuivre les travaux liés à l'amélioration de la prédiction du risque de fracture.

Appendix 3: FEM Parameters from CT-Scat and HR-PQCT

Finite Element models from CT-Scan

Author	Part	Geometry and Meshing				Mechanical Properties		Validation		
		Mesh	Type	Nodes	Elements	Cortical Bone	Trabecular Bone	Configuration	Samples	Results
(Duchemin et al. 2008)	Femur	3D GEOM Deformation from gFEM	HEXA 8 nodes	22746	15300	Isotropic Linear Heterogeneous E= Fn (ρHA)	Isotropic Linear Heterogeneous E= Fn(ρHA)	Quasi-static compression Stance	39 proximal femurs tested in vitro	Fracture load prediction r2 = 0.87 SEE = 1220N p < 0.05
(Crawford et al. 2003)	Vertebra (L1–L4)	3D VOXEL voxel to element	HEXA 8 nodes			Transverse isotropy Linear Heterogeneous E= Fn (BMD) Kopperdahl DL, Morgan EF, Keaveny TM. Quantitative computed tomography estimates of the mechanical properties of human vertebral trabecular bone. J Orthop Res 2002;20:801–5.	Transverse isotropy Linear Heterogeneous E= Fn (BMD) Kopperdahl DL, Morgan EF, Keaveny TM. Quantitative computed tomography estimates of the mechanical properties of human vertebral trabecular bone. J Orthop Res 2002;20:801–5.	Quasi-static compression Axial	13 vertebral bodies tested in vitro	Strength r2 = 0.86, SEE=716N p < 0.0001 Stiffness r2 = 0.82, SEE= 796N p < 0.0001
(Hazrati Marangalou et al. 2012)	Femur	3D GEOM	TETRA 4 nodes		size: 2mm	Anisotropic Linear Heterogeneous Material properties were based on the element density and fabric values Zysset, P. K. and A. Curnier (1995). "An alternative model for anisotropic elasticity based on fabric tensors." Mechanics of Materials 21(4): 243-250.	Anisotropic Linear Heterogeneous Material properties were based on the element density and fabric values Zysset, P. K. and A. Curnier (1995). "An alternative model for anisotropic elasticity based on fabric tensors." Mechanics of Materials 21(4): 243-250.	7 physiological state: Walking, going upstairs, going downstairs, standing up, sitting down, stance, knee bending Bergmann G., Graichen F., et al. (2010). "Realistic loads for testing hip implants " Bio-Medical Materials and Engineering 20(2): 65-75.	1 proximal femur tested in vitro	Degree of anisotropy mesured with CT-scan resolution r=0.41 Fabric tensor mesured with CT-scan resolution r=0.89
(Sapin-de Brosses et al. 2012)	Vertebra (L1–L4)	3D GEOMDeformation from gFEM	HEXA8 nodes		18000	Isotropic Linear Heterogeneous E= Fn(BMD) D. Kopperdahl, E. Morgan and T. Keaveny, "Quantitative computed tomography estimates of the mechanical properties of human vertebral trabecular bone," J Orthop Res, vol. 20, no. 4, pp. 801-5, 2002.	Isotropic Linear Heterogeneous E= Fn(BMD) D. Kopperdahl, E. Morgan and T. Keaveny, "Quantitative computed tomography estimates of the mechanical properties of human vertebral trabecular bone," J Orthop Res, vol. 20, no. 4, pp. 801-5, 2002.	Compression at the anterior third of the vertebra,	35 vertebrae from 10 donors	Not validaded
(Grassi et al. 2012)	Vertebra (L1–L4)	3D GEOM Deformation from gFEM	HEXA 8 nodes		18000	Isotropic Linear Homogeneuos E= Fn(BMD) inner mean value D. Kopperdahl, E. Morgan and T. Keaveny, "Quantitative computed tomography estimates of the mechanical properties of human vertebral trabecular bone," J Orthop Res, vol. 20, no. 4, pp. 801-5, 2002.	Isotropic Linear Homogeneuos E= Fn(BMD) outer mean value D. Kopperdahl, E. Morgan and T. Keaveny, "Quantitative computed tomography estimates of the mechanical properties of human vertebral trabecular bone," J Orthop Res, vol. 20, no. 4, pp. 801-5, 2002.	Compression at the anterior third of the vertebra,	35 vertebrae from 10 donors	Fracture load prediction r2 = 0.78 SEE=518N (taking heterogeneous version as reference)

Author	Part	Geometry and Meshing				Mechanical Properties		Validation		
		Mesh	Type	Nodes	Elements	Cortical Bone	Trabecular Bone	Configuration	Samples	Results
(Schileo et al. 2007b)	Femur	3D GEOM	TETRA10 nodes	280000	210000size: 2mm	Isotropic Linear Heterogeneous E= Fn (ρ) Morgan, E.F.,Bayraktar,H.H.,Keaveny,T.M.,2003.Trabecularbonemodulus–density relationshipsdependonanatomicsite.JournalofBiomechanics36,897–904.Phantom Calibration: Kalender, W.A.,1992.Aphantomforstandardizationandqualitycontrolinspinalbone mineralmeasurementsbyQCTandDXA:designconsiderationsandspecifications. MedicalPhysics19,583–586.Calibration correction: Schileo, E.,Dall'ara,E.,Taddei,F.,Malandrino,A.,Schotkamp,T.,Baleani,M.,Viceconti, M.,2008.Anaccurateestimationofbonedensityimprovestheaccuracy ofsubject-specificfiniteelementmodels.JournalofBiomechanics41,2483–2491.	Isotropic Linear Heterogeneous E= Fn (ρ) Morgan, E.F.,Bayraktar,H.H.,Keaveny,T.M.,2003.Trabecularbonemodulus–density relationshipsdependonanatomicsite.JournalofBiomechanics36,897–904.Phantom Calibration: Kalender, W.A.,1992.Aphantomforstandardizationandqualitycontrolinspinalbone mineralmeasurementsbyQCTandDXA:designconsiderationsandspecifications. MedicalPhysics19,583–586.Calibration correction: Schileo, E.,Dall'ara,E.,Taddei,F.,Malandrino,A.,Schotkamp,T.,Baleani,M.,Viceconti, M.,2008.Anaccurateestimationofbonedensityimprovestheaccuracy ofsubject-specificfiniteelementmodels.JournalofBiomechanics41,2483–2491.	12 sideways loads: Combination of internal rotation angle(0, 15 and 30) and adduction angle(0, 10, 20 and 30	3 cadaver proximal femurs. Sixteen strain rosettes. In vitro tests	Strain & displacement predictionr2 > 0.9RMSE < 10%
	Femur	3D GEOM	TETRA10 nodes	104020 to 124592	from 69272 to 80508	Isotropic Linear Heterogeneous E= Fn (ρ) Carter, D.R., Hayes, W.C., 1977. The compressive behavior of bone as atwo-phase porous structure. The Journal of Bone and Joint Surgery.American Volume 59, 954–962Keller, T.S., 1994. Predicting the compressive mechanical behavior ofbone. Journal of Biomechanics 27, 1159–1168Morgan, E.F., Bayraktar, H.H., Keaveny, T.M., 2003. Trabecular bonemodulus–density relationships depend on anatomic site. Journal ofBiomechanics 36, 897–904.	Isotropic Linear Heterogeneous E= Fn (ρ) Carter, D.R., Hayes, W.C., 1977. The compressive behavior of bone as atwo-phase porous structure. The Journal of Bone and Joint Surgery.American Volume 59, 954–962Keller, T.S., 1994. Predicting the compressive mechanical behavior ofbone. Journal of Biomechanics 27, 1159–1168Morgan, E.F., Bayraktar, H.H., Keaveny, T.M., 2003. Trabecular bonemodulus–density relationships depend on anatomic site. Journal ofBiomechanics 36, 897–904.	6 loading conditions:one neutral vertical position, two extreme positions in frontal plane, two extreme positions in sagital plane & 8° frontal plane (stance) configuration	8 cadaver femurs, tested in vitro	Strain & displacement predictionr2 = 0.91RMSE lower than 10%
(Taddei et al. 2004)	Ileum, femur and tibia	3D GEOM	HEXA 8 nodes	Coarse Femur 5779 Ileum 8015 Tibia 4616	-	-	-	a vertical force (100 N) on femur head; two vertical forces (100 N) on tibial plateau, a vertical force (100 N) on the acetabulum	not validated	mapping algorithm influences the material distribution Diferences between the maximum von Mises stress < 10% Diferences between the von Mises Stress > 10%
	Ileum, femur and tibia	3D GEOM	HEXA 8 nodes	Coarse Femur 93081 Ileum 124231 Tibia 76406	-	-	-	a vertical force (100 N) on femur head; two vertical forces (100 N) on tibial plateau, a vertical force (100 N) on the acetabulum	not validated	mapping algorithm influences the material distribution Diferences between the maximum von Mises stress < 10% Diferences between the von Mises Stress > 10%

Author	Part	Geometry and Meshing				Mechanical Properties		Validation		
		Mesh	Type	Nodes	Elements	Cortical Bone	Trabecular Bone	Configuration	Samples	Results
(Viceconti et al. 2004)	Femur	3D GEOM	HEXA8 nodes		from 47796 to 27801	Isotropic Linear Heterogeneous E= Fn (ρ) Keller, T.S., 1994. Predicting the compressive mechanical behavior ofbone. Journal of Biomechanics 27 (9), 1159–1168.& homogeneous (1)14200 Mpa	Isotropic Linear Heterogeneous E= Fn (ρ)Keller, T.S., 1994. Predicting the compressive mechanical behavior ofbone. Journal of Biomechanics 27 (9), 1159–1168.& homogeneous (1)14200 Mpa	stress gradients equal or larger than those usually produced in vivo. Femur loaded with thesame forces used in the in vitro study. Viceconti, M., Bellingeri, L., Cristofolini, L., Toni, A., 1998. Acomparative study on different methods of automatic meshgeneration of human femurs. Medical Engineering and Physics 20(1), 1–10.escribir la configuracion segun veconti 1998	5 femurs. Based on previous in vitro results (Viceconti et al., 1998)	Viceconti 1998 is a valid procedure for the generationof subject-specific finite element meshes
(Schileo et al. 2008b)	Femur	3D GEOM	TETRA 10 nodes	from 104020 to124592	from 69272 to 80508	Isotropic Linear Heterogeneous E= Fn (ρ) Morgan, E.F., Bayraktar, H.H., Keaveny, T.M., 2003. Trabecular bone modulus–density relationships depend on anatomic site. Journal of Biomechanics 36, 897–904.	Isotropic Linear Heterogeneous E= Fn (ρ) Morgan, E.F., Bayraktar, H.H., Keaveny, T.M., 2003. Trabecular bone modulus–density relationships depend on anatomic site. Journal of Biomechanics 36, 897–904.	a load simulating the reaction force acting at the hip joint: 8° in the frontal plane(direction of spontaneous fractures Cristofolini, L., Juszczyk, M., Martelli, S., Taddei, F., Viceconti, M., 2007. In vitro replication of spontaneous fractures of the proximal human femur. Journal of Biomechanics 12 (e-pub ahead of print))	Three cadaver femurs. In vitro validation tested in vitro	Fracture prediction can be achieved using εmax (maximal principal strain) criteria
(Gray et al. 2008)	Tibia	3D GEOM	TETRA10 nodes	75583		Transverse isotropyLinearHeterogeneous E = Fn(ρ) Rho, J. Y., Hobatho, M. C., and Ashman, R. B., 1995, “Relations of MechanicalProperties to Density and CT Numbers in Human Bone,” Med. Eng. Phys.,17 5 , pp. 347–355	Transverse isotropy Linear HeterogeneousE = Fn(ρ) z direction: Rho, J. Y., Hobatho, M. C., and Ashman, R. B., 1995, “Relations of MechanicalProperties to Density and CT Numbers in Human Bone,” Med. Eng. Phys.,17 5 , pp. 347–355x & y direction: Rho, J. Y., 1996, “An Ultrasonic Method for Measuring the Elastic Propertiesof Human Tibial Cortical and Cancellous Bone,” Ultrasonics, 34 8 , pp. 777–783.	Two bending load conditions, nine axial loading conditions, and a torsional loading condition	One cadaver tibia teted in vitro	Strain prediction (Axial load)r2 = 0.986% < RMSE < 16%

Author	Part	Geometry and Meshing				Mechanical Properties		Validation		
		Mesh	Type	Nodes	Elements	Cortical Bone	Trabecular Bone	Configuration	Samples	Results
(Taddei, et al. 2006)	Femur	3D GEOM	TETRA 10 nodes	118970	76026	Isotropic Linear Heterogeneous E= Fn (ρ) mapped with Bonemat_V2 Keller TS. Predicting the compressive mechanical behavior of bone. J Biomech 1994;27(9):1159–68.	Isotropic Linear Heterogeneous E= Fn (ρ) mapped with Bonemat_V2 Keller TS. Predicting the compressive mechanical behavior of bone. J Biomech 1994;27(9):1159–68.	(1) Neutral: (2) Maximum adduction (3) Maximum abduction (4) Maximum flexion (5) Maximum extension	One cadaver femur tested in vitro	superficial stresses prediction R2 = 0,91, RMSE = 8.6%, peak error = 27%
						Isotropic Linear Homogeneous E= 19.3 Gpa calculated	Isotropic Linear Homogeneous E= 590MPa	(1) Neutral: (2) Maximum adduction (3) Maximum abduction (4) Maximum flexion (5) Maximum extension	One cadaver femur tested in vitro	superficial stresses prediction R2 = 0,89, RMSE = 9.6%, peak error = 35%

Finite Element models from high resolution Images

Author	Part	Geometry and Meshing				Mechanical Properties		Validation		
		Mesh	Type	Nodes	Elements	Cortical Bone	Trabecular Bone	Configuration	Samples	Results
(Macneil & Boyd 2008)	Femur	3D GEOM Deformation from gFEM	HEXA 8 nodes	22746	15300	Isotropic Linear Heterogeneous E= Fn (ρHA) Duchemin et al. (2007)	Isotropic Linear Heterogeneous E= Fn(ρHA) Duchemin et al. (2007)	Quasi-static compression Stance	39 proximal femurs tested in vitro	<u>Fracture load prediction</u> r2 = 0.87 SEE = 1220N p < 0.05
	Vertebra (L1–L4)	3D VOXEL voxel to element	HEXA 8 nodes			Transverse isotropy Linear Heterogeneous E= Fn (BMD) Kopperdahl DL, Morgan EF, Keaveny TM. Quantitative computed tomography estimates of the mechanical properties of human vertebral trabecular bone. J Orthop Res 2002;20:801–5.	Transverse isotropy Linear Heterogeneous E= Fn (BMD) Kopperdahl DL, Morgan EF, Keaveny TM. Quantitative computed tomography estimates of the mechanical properties of human vertebral trabecular bone. J Orthop Res 2002;20:801–5.	Quasi-static compression Axial	13 vertebral bodies tested in vitro	<u>Strength</u> r2 = 0.86, SEE=716N p < 0.0001 <u>Stiffness</u> r2 = 0.82, SEE= 796N p < 0.0001
(Liu et al. 2010)	Femur	3D GEOM	TETRA 4 nodes		size: 2mm	Anisotropic Linear Heterogeneous Material properties were based on the element density and fabric values Zysset, P. K. and A. Curnier (1995). "An alternative model for anisotropic elasticity based on fabric tensors." Mechanics of Materials 21(4): 243-250.	Anisotropic Linear Heterogeneous Material properties were based on the element density and fabric values Zysset, P. K. and A. Curnier (1995). "An alternative model for anisotropic elasticity based on fabric tensors." Mechanics of Materials 21(4): 243-250.	7 physiological state: Walking, going upstairs, going downstairs, standing up, sitting down, stance, knee bending Bergmann G., Graichen F., et al. (2010). "Realistic loads for testing hip implants " Bio-Medical Materials and Engineering 20(2): 65-75.	1 proximal femur tested in vitro	Degree of anisotropy mesured with CT-scan resolution r=0.41 Fabric tensor mesured with CT-scan resolution r=0.89

Author	Part	Geometry and Meshing				Mechanical Properties		Validation		
		Mesh	Type	Nodes	Elements	Cortical Bone	Trabecular Bone	Configuration	Samples	Results
(Liu, et al. 2010)	Vertebra (L1–L4)	3D GEOM Deformation from gFEM	HEXA 8 nodes		18000	Isotropic Linear Heterogeneous E= Fn(BMD) D. Kopperdahl, E. Morgan and T. Keaveny, "Quantitative computed tomography estimates of the mechanical properties of human vertebral trabecular bone," J Orthop Res, vol. 20, no. 4, pp. 801-5, 2002.	Isotropic Linear Heterogeneous E= Fn(BMD) D. Kopperdahl, E. Morgan and T. Keaveny, "Quantitative computed tomography estimates of the mechanical properties of human vertebral trabecular bone," J Orthop Res, vol. 20, no. 4, pp. 801-5, 2002.	Compression at the anterior third of the vertebra,	35 vertebrae from 10 donors	Not validaded
	Vertebra (L1–L4)	3D GEOMDeformation from gFEM	HEXA8 nodes		18000	Isotropic LinearHomogeneuos E= Fn(BMD) inner mean value D. Kopperdahl, E. Morgan and T. Keaveny, "Quantitative computed tomography estimates of the mechanical properties of human vertebral trabecular bone," J Orthop Res, vol. 20, no. 4, pp. 801-5, 2002.	Isotropic Linear Homogeneuos E= Fn(BMD) outer mean value D. Kopperdahl, E. Morgan and T. Keaveny, "Quantitative computed tomography estimates of the mechanical properties of human vertebral trabecular bone," J Orthop Res, vol. 20, no. 4, pp. 801-5, 2002.	Compression at the anterior third of the vertebra,	35 vertebrae from 10 donors	Fracture load predictionr2 = 0.78SEE=518N (taking heterogeneous version as reference)
(Mueller et al. 2009)	Femur	3D GEOM	TETRA 10 nodes	280000	210000 size: 2mm	Isotropic Linear Heterogeneous E= Fn (ρ) Morgan, E.F.,Bayraktar,H.H.,Keaveny,T.M.,2003.Trabecularbonemodulus–density relationshipsdependonanatomicsite.JournalofBiomechanics36, 897–904. Phantom Calibration: Kalender, W.A.,1992.Aphantomforstandardizationandqualitycontrolinspinal bone mineralmeasurementsbyQCTandDXA:designconsiderationsand specifications. MedicalPhysics19,583–586. Calibration correction: Schileo, E.,Dall'ara,E.,Taddei,F.,Malandrino,A.,Schotkamp,T.,Baleani,M., Viceconti, M.,2008.Anaccurateestimationofbonedensityimprovesthe accuracy ofsubject-specificfiniteelementmodels.JournalofBiomechanics41, 2483–2491.	Isotropic Linear Heterogeneous E= Fn (ρ) Morgan, E.F.,Bayraktar,H.H.,Keaveny,T.M.,2003.Trabecularbonemodulus–density relationshipsdependonanatomicsite.JournalofBiomechanics36, 897–904. Phantom Calibration: Kalender, W.A.,1992.Aphantomforstandardizationandqualitycontrolinspinal bone mineralmeasurementsbyQCTandDXA:designconsiderationsand specifications. MedicalPhysics19,583–586. Calibration correction: Schileo, E.,Dall'ara,E.,Taddei,F.,Malandrino,A.,Schotkamp,T.,Baleani,M., Viceconti, M.,2008.Anaccurateestimationofbonedensityimprovesthe accuracy ofsubject-specificfiniteelementmodels.JournalofBiomechanics41, 2483–2491.	12 sideways loads: Combination of internal rotation angle(0, 15 and 30) and adduction angle(0, 10, 20 and 30	3 cadaver proximal femurs. Sixteen strain rosettes. In vitro tests	Strain & displacement prediction r2 > 0.9 RMSE < 10%
	Femur	3D GEOM	TETRA10 nodes	104020 to 124592	from 69272 to 80508	Isotropic Linear Heterogeneous E= Fn (ρ) Carter, D.R., Hayes, W.C., 1977. The compressive behavior of bone as atwo-phase porous structure. The Journal of Bone and Joint Surgery.American Volume 59, 954–962Keller, T.S., 1994. Predicting the compressive mechanical behavior ofbone. Journal of Biomechanics 27, 1159–1168Morgan, E.F., Bayraktar, H.H., Keaveny, T.M., 2003. Trabecular bonemodulus–density relationships depend on anatomic site. Journal ofBiomechanics 36, 897–904.	Isotropic Linear Heterogeneous E= Fn (ρ) Carter, D.R., Hayes, W.C., 1977. The compressive behavior of bone as atwo-phase porous structure. The Journal of Bone and Joint Surgery.American Volume 59, 954–962Keller, T.S., 1994. Predicting the compressive mechanical behavior ofbone. Journal of Biomechanics 27, 1159–1168Morgan, E.F., Bayraktar, H.H., Keaveny, T.M., 2003. Trabecular bonemodulus–density relationships depend on anatomic site. Journal ofBiomechanics 36, 897–904.	6 loading conditions:one neutral vertical position, two extreme positions in frontal plane, two extreme positions in sagital plane & 8° frontal plane (stance) configuration	8 cadaver femurs, tested in vitro	Strain & displacement predictionr2 = 0.91RMSE lower than 10%
(Vilayphiou et al. 2010) (Mueller et al. 2009)	Ileum, femur and tibia	3D GEOM	HEXA 8 nodes	Coarse Femur 5779 Ileum 8015 Tibia 4616	-	-	-	a vertical force (100 N) on femur head; two vertical forces (100 N) on tibial plateau, a vertical force (100 N) on the acetabulum	not validated	mapping algorithm influences the material distribution Diferences between the maximum von Mises stress < 10% Diferences between the von Mises Stress > 10%

Author	Part	Geometry and Meshing				Mechanical Properties		Validation		
		Mesh	Type	Nodes	Elements	Cortical Bone	Trabecular Bone	Configuration	Samples	Results
	Ileum, femur and tibia	3D GEOM	HEXA 8 nodes	Coarse Femur 93081 Ileum 124231 Tibia 76406	-	-	-	a vertical force (100 N) on femur head; two vertical forces (100 N) on tibial plateau, a vertical force (100 N) on the acetabulum	not validated	mapping algorithm influences the material distribution Diferences between the maximum von Mises stress < 10% Diferences between the von Mises Stress > 10%
(Popp et al. 2012)	Femur	3D GEOM	HEXA8 nodes		from 47796 to 27801	Isotropic Linear Heterogeneous E= Fn (ρ)Keller, T.S., 1994. Predicting the compressive mechanical behavior ofbone. Journal of Biomechanics 27 (9), 1159–1168.& homogeneous (1)14200 Mpa	Isotropic Linear Heterogeneous E= Fn (ρ)Keller, T.S., 1994. Predicting the compressive mechanical behavior ofbone. Journal of Biomechanics 27 (9), 1159–1168.& homogeneous (1)14200 Mpa	stress gradients equal or larger than those usually produced in vivo. Femur loaded with thesame forces used in the in vitro study. Viceconti, M., Bellingeri, L., Cristofolini, L., Toni, A., 1998. Acomparative study on different methods of automatic meshgeneration of human femurs. Medical Engineering and Physics 20(1), 1–10.escribir la configuracion segun veconti 1998	5 femurs. Based on previous in vitro results (Viceconti et al., 1998)	Viceconti 1998 is a valid procedure for the generationof subject-specific finite element meshes

Author	Part	Geometry and Meshing				Mechanical Properties		Validation		
		Mesh	Type	Nodes	Elements	Cortical Bone	Trabecular Bone	Configuration	Samples	Results
(Varga et al. 2010)	Femur	3D GEOM	TETRA 10 nodes	from 104020 to124592	from 69272 to 80508	Isotropic Linear Heterogeneous E= Fn (ρ) Morgan, E.F., Bayraktar, H.H., Keaveny, T.M., 2003. Trabecular bone modulus–density relationships depend on anatomic site. Journal of Biomechanics 36, 897–904.	Isotropic Linear Heterogeneous E= Fn (ρ) Morgan, E.F., Bayraktar, H.H., Keaveny, T.M., 2003. Trabecular bone modulus–density relationships depend on anatomic site. Journal of Biomechanics 36, 897–904.	a load simulating the reaction force acting at the hip joint: 8° in the frontal plane(direction of spontaneous fractures Cristofolini, L., Juszczyk, M., Martelli, S., Taddei, F., Viceconti, M., 2007. In vitro replication of spontaneous fractures of the proximal human femur. Journal of Biomechanics 12 (e-pub ahead of print))	Three cadaver femurs. In vitro validation tested in vitro	Fracture prediction can be achieved using εmax (maximal principal strain) criteria
(Varga et al. 2009)	Tibia	3D GEOM	TETRA10 nodes	75583		Transverse Isotropy Linear Heterogeneous E = Fn(ρ) Rho, J. Y., Hobatho, M. C., and Ashman, R. B., 1995, “Relations of MechanicalProperties to Density and CT Numbers in Human Bone,” Med. Eng. Phys.,17 5 , pp. 347–355	Transverse Isotropy Linear HeterogeneousE = Fn(ρ)z direction: Rho, J. Y., Hobatho, M. C., and Ashman, R. B., 1995, “Relations of MechanicalProperties to Density and CT Numbers in Human Bone,” Med. Eng. Phys.,17 5 , pp. 347–355x & y direction: Rho, J. Y., 1996, “An Ultrasonic Method for Measuring the Elastic Propertiesof Human Tibial Cortical and Cancellous Bone,” Ultrasonics, 34 8 , pp. 777–783.	Two bending load conditions, nine axial loading conditions, and a torsional loading condition	One cadaver tibia teted in vitro	Strain prediction (Axial load)r2 = 0.986% < RMSE < 16%
(Ackerman et al. 2012) (Kazakia et al. 2013)	Femur	3D GEOM	TETRA 10 nodes	118970	76026	Isotropic Linear Heterogeneous E= Fn (ρ) mapped with Bonemat_V2 Keller TS. Predicting the compressive mechanical behavior of bone. J Biomech 1994;27(9):1159–68.	Isotropic Linear Heterogeneous E= Fn (ρ) mapped with Bonemat_V2 Keller TS. Predicting the compressive mechanical behavior of bone. J Biomech 1994;27(9):1159–68.	(1) Neutral: (2) Maximum adduction (3) Maximum abduction (4) Maximum flexion (5) Maximum extension	One cadaver femur tested in vitro	superficial stresses prediction R2 = 0,91, RMSE = 8.6%, peak error = 27%
						Isotropic Linear Homogeneous E= 19.3 Gpa calculated	Isotropic Linear Homogeneous E= 590MPa	(1) Neutral: (2) Maximum adduction (3) Maximum abduction (4) Maximum flexion (5) Maximum extension	One cadaver femur tested in vitro	superficial stresses prediction R2 = 0,89, RMSE = 9.6%, peak error = 35%